Fermilab

FERMILAB-THESIS-2001-22

Observation of Diffractive J/ψ Production at the Fermilab Tevatron

A thesis presented to the faculty of

The Rockefeller University

in partial fulfillment of the requirements for

the degree of Doctor of Philosophy

by

Andrei Solodsky

2001

Acknowledgments

I would like to express my gratitude to the entire Rockefeller University Experimental High Energy Physics Group. Especially, I would like to thank Professor Konstantin Goulianos, who gave me an opportunity to join the group and CDF experiment and was constantly supporting my work during these years. I benefited very much from the opportunity to share my time between hardware projects, analysis of experimental data and discussions of the obtained results. I would like to thank my research advisor, Professor Luc Demortier. I gratefully acknowledge his guidance and assistance in all aspects of the research. I consider myself fortunate for having an opportunity to meet such colleagues as Giorgio Apollinari, Anwar Bhatti, Kerstin Borras, Mary Convery, Stefano Lami and Michele Gallinaro. From working with them I have learned a great deal of experimental physics and professionalism. My special thanks are due to Luc Demortier, Konstantin Goulianos and Anwar Bhatti for their extremely careful reading of the manuscript and numerous important corrections, which made this thesis less painful to a reader. I also thank Professor William Carithers for his comments and suggestions. I thank the diffractive physics group for numerous hours spent on discussions of different aspects of the analysis. I would like to thank the entire QCD group of the CDF experiment for helpful suggestions and discussions. Especially, I would like to thank Mike Albrow, Joey Huston and Bob Blair for their constant interest to this research. I thank my fellow graduate students Alexander Akopian, Suren Bagdasarov, Andrea Bocci, Ken-ichi Hatakeyama, Christina Mesropian and Alexey Titov for sharing with me the unforgettable experience of being a graduate student at The Rockefeller University. This thesis would not have been possible also without the dedicated effort of the entire CDF collaboration. All of the people involved have my sincerest thanks. My very deep acknowledgments go to

the Rockefeller University for providing me with the exceptional research opportunity in New York City.

Finally, my most important acknowledgment is for the love, support and encouragement of my family – my parents and my wife.

Contents

List of Figures

List of Tables

Observation of Diffractive J/ψ Production at the Fermilab Tevatron

by
Andrei Solodsky

Abstract

The first observation of diffractive $J/\psi(\rightarrow \mu^+\mu^-)$ production in $\bar{p}p$ collisions at $\sqrt{s}$=1.8 TeV is presented using data collected from the Collider Detector at Fermilab (CDF). In a sample of events with two muons of transverse momentum $P_T^{\mu} > 2$ GeV/c within the pseudorapidity region $|\eta|$ <1.0, the ratio of diffractive to total J/ψ production rates is found to be $R_{J/\psi} = (1.45 \pm 0.25)\%$. Diffractive events are identified by their rapidity gap signature. The ratio $R_{J/\psi}$ is studied as a function of the momentum fraction $x_{\rm bj}$ of the struck parton in the (anti)proton. By combining this measurement with a similar one of diffractive dijet production with a leading antiproton, the gluon fraction of the (anti)proton diffractive structure is found to be 0.59 ± 0.15. These results are compared with reported results for diffractive W, dijet and b-quark production.

Chapter 1

Introduction

The current theory of strong interactions, Quantum Chromodynamics (QCD), has been very successful in describing perturbative hadronic interactions at large momentum transfers (Q^2), e.g. jet or prompt photon production. However, most of the hadronic cross section is associated with non-perturbative processes, e.g. elastic and diffractive scattering, which cannot be calculated from QCD since the perturbation theory fails in this regime. In terms of final state properties, diffractive events are characterized by the presence of rapidity gaps, regions in rapidity space devoid of particles, which are not exponentially suppressed with increasing gap width, as would be expected for gaps produced by fluctuations in the hadronization of a non-diffractive event. The specific property of the final state of single-diffractive events, $p+p \to p+X$, is the appearance of a leading hadron, i.e. a hadron with a momentum close to the beam momentum, which scatters quasi-elastically and is separated from the diffractive final state X by a rapidity gap.

Diffractive processes play a very important role in fundamental particle dynamics and have a close connection to the problem of quark and gluon confinement.

In theory, diffractive scattering is described by non-perturbative QCD (non-pQCD), for which only phenomenological models are available.

The term *diffraction* is related to the behavior of the cross-section for diffractive event production as a function of the momentum transfer. An exponential fall-off with increasing momentum transfer is observed, reminiscent of the properties of the diffraction of light on a circular aperture. Another characteristic of diffractive processes is weak dependence on the center-of-mass energy.

In terms of quantum field theory, any process between two hadrons is described by the exchange of field carriers. In order to preserve a hadron as a color singlet in the single diffraction process the exchanged object should carry the quantum numbers of the vacuum. This colorless exchange object with vacuum quantum numbers is commonly referred to as the *pomeron*. The partonic structure of pomeron exchange is one important question which can be addressed by studying *hard* (large momentum transfer) diffraction processes.

At the Fermilab Tevatron $p\bar{p}$ collider, the gluonic content of pomeron exchange can be probed by measuring diffractive J/ψ meson production, since in leading order J/ψ production occurs mostly through the subprocess $g + g \rightarrow J/\psi + g$. A similar study was done by analyzing diffractive $b\bar{b}$ production [1], another process sensitive to the gluon part of pomeron exchange. In that analysis the ratio of diffractive to non-diffractive $b\bar{b}$ cross-sections, averaged over phase space, was measured. In the measurement discussed here, we extract the diffractive to non-diffractive ratio as a function of the momentum fraction of the struck parton in the (anti)proton x_{bj} and thereby determining the diffractive structure function of the (anti)proton. Since J/ψ's probe a different kinematical region than $b\bar{b}$ events, a comparison with the previous work may lead to interesting results.

In this dissertation, we present the first observation of diffractive J/ψ meson production in $\bar{p}p$ collisions at $\sqrt{s} = 1.8$ TeV using the Collider Detector at Fermilab (CDF). Chapter 2 provides a brief overview of theoretical aspects of diffractive scattering, including models of hard diffraction dissociation. Chapter 3 discusses the current theoretical understanding of charmonium hadroproduction. This chapter also addresses the physical motivation for the study of diffractive J/ψ production at the Tevatron. In Chapter 4, the Fermilab accelerator complex and components of the Collider Detector at Fermilab are described, paying more attention to the detector parts that are relevant to this analysis. The data collection, trigger requirements, J/ψ candidate selection criteria and background contributions are presented in Chapter 5. Chapter 6 describes the details of the method used to extract the diffractive J/ψ signal, the correction factors required to calculate the ratio of diffractive to non-diffractive J/ψ production, and includes a study of the B-hadron decay contribution in the selected J/ψ sample. Extensive Monte Carlo studies of J/ψ production, which are critical for evaluating the fraction of diffractive events satisfying our rapidity gap requirement, are presented in Chapter 7. The final ratio of diffractive to non-diffractive prompt J/ψ production, $R_{J/\psi}$, corrected for the rapidity gap acceptance, is also given in this chapter. The analysis of diffractive J/ψ events with an additional jet required in the event is presented in Chapter 8. The distribution of $x_{\rm bj}$, calculated from the reconstructed jet, is presented in this chapter. By comparing the ratio $R_{J/\psi}$ for the $J/\psi + jet$ sample as a function of $x_{\rm bj}$ with that for dijet production [22], the gluon fraction of the (anti)proton diffractive structure function is derived. The last chapter summarizes the results and compares them with other measurements.

Chapter 2

Theoretical Models of Hard Diffraction

2.1 Introduction

The dynamics of diffractive processes are one important aspect of the more general unsolved problem of non-pQCD, the others being hadronization in high energy collisions and the confinement of quarks and gluons. The understanding of diffractive phenomena from the Lagrangian of QCD is a 'first class challenge' to theorists, which in recent years has received revived attention due to the discovery of diffractive hard scattering. In this chapter we discuss the phenomenology of hard diffraction, paying more attention to the experimental findings which shaped the theoretical understanding of the problem, and presenting them in historical order.

2.2 Rapidity Gaps and the Pomeron Concept

In collision experiments, the distribution of final state particles is usually expressed in terms of the rapidity, y, defined as

$$y = \frac{1}{2}\ln\left(\frac{E + p_z}{E - p_z}\right), \tag{2.1}$$

where E and p_z are the total energy and longitudinal momentum of the particle, respectively. For relativistic particles

$$y \approx -\ln\left(\tan\frac{\theta}{2}\right), \tag{2.2}$$

where the polar angle θ is with respect to the z-axis of the beam and the approximation is exact for massless particles. The quantity on the right side of expression 2.2, named *pseudorapidity*, is usually denoted by η. We will use rapidity and pseudorapidity interchangeably throughout this dissertation.

In a totally inelastic interaction the final state hadrons are distributed with a flat rapidity plateau. This corresponds to longitudinal phase space where the transverse momenta of produced particles are limited to a few hundred MeV, but longitudinal momenta cover the available phase space. The probability for producing events with a *rapidity gap*, i.e. a rapidity region without any particles, due to fluctuations in the hadronization in such a rapidity distribution decreases exponentially with the width of the gap. Experimentally, gaps are observed at a much higher rate. *Diffraction* is often defined as events with *large rapidity gaps in the produced-particle phase space which are not exponentially suppressed* [2]. This is a more general definition than that in terms of an escaping proton taking a large fraction ($x_F \gtrsim 0.9$) of the incident proton momentum, which imposes a rapidity gap simply by kinematical constraints. Nevertheless, a gap can be anywhere in the event and therefore the gap

definition of diffraction allows a forward system of higher mass than a single proton. In this dissertation we will assume that for diffractive events the probability of a forward system of mass higher than the proton mass is negligibly small.

The simplest gap events are produced in elastic and single diffractive scattering. Due to the scattered proton an exchange of energy-momentum occurs, but not of quantum numbers. In Regge phenomenology [3], these processes are described by the exchange of a pomeron ($\mathbb{P}$), named after Russian theoretician Isaak Yakovlevich Pomeranchuk (1913-1966). In QCD the Pomeron is a color-singlet with vacuum quantum numbers.

The kinematics of single diffraction (SD) scattering can be described in terms of two variables: the momentum fraction $x_p = p_f/p_i$ of the quasi-elastically scattered proton relative to the initial proton momentum and the square of the momentum transfer $t = (p_i - p_f)^2$. The pomeron then carries the momentum fraction $\xi = 1 - x_p$ and has a negative mass-squared $m^2_{\mathbb{P}} = t < 0$ indicating that it is a virtual exchanged object. Meanwhile, the other proton dissociates producing a hadronic system X of mass $M_X^2 = s \cdot \xi$, i.e. the invariant mass-squared of the *pomeron-proton collision.* Experimentally it is found that the cross section for single diffraction is well described by

$$\frac{d\sigma_{SD}}{dtd\xi} \simeq \frac{1}{\xi}(a_1 e^{b_1 t} + a_2 e^{b_2 t} + a_3 e^{b_3 t} + ...) \simeq \frac{a}{M_X^2}|F(t)|^2, \tag{2.3}$$

where the exponential damping in t can be interpreted in terms of a proton form factor $F(t)$ giving the probability that the proton stays intact after the momentum *kick* t.

The Regge factorization formalism relates the differential cross sections for elastic and diffractive processes. This is accomplished through the factorization of

different vertices such that the same type of vertex in different processes is given by the same expression. Exchange of other than vacuum quantum numbers are interpreted as meson exchanges (ρ, π). The exchanged object is not a real state, but virtual with a negative mass-squared. In fact, it is a representation of a whole set of states with essentially the same quantum numbers. The dependence of spin α on mass-squared t of such a set provides a linear relation which can be extrapolated to $m^2 = t < 0$ and gives the trajectory $\alpha(t)$ for the exchange. This yields the fundamental energy dependence $\sigma \sim s^{2\alpha(t)-2}$ of the cross section. The pomeron trajectory $\alpha_{I\!P}(t) = 1 + \epsilon + \alpha' t \simeq 1 + 0.115 + 0.26t$ [4] has the largest value of all trajectories at $t = 0$ (intercept), resulting in the main contribution to the hadron-hadron cross section. In contrast to the ρ and π trajectories, which have well known integer spin states at the pole positions $t = m^2_{meson}$, there are no real observed states on the pomeron trajectory. A recently found spin-2 glueball candidate with mass 1926 ± 12 MeV [5] fits well on the pomeron trajectory. This would be in agreement with the proposal that the pomeron is some gluonic system [6, 7]which may be interpreted as a virtual glueball [8].

2.3 Diffractive Hard Scattering

In QCD the pomeron can be considered as a hadron-like object with a quark and gluon content. In this concept, pomeron-hadron interactions would then resemble hadron-hadron collisions and produce final state hadrons in longitudinal phase space, just as observed.

According to the pomeron factorization hypothesis, the diffractive hard scattering process is described [9] in terms of an emitted pomeron and a pomeron-particle interaction, which is a hard scattering process on the parton level. As a result, the

diffractive hard scattering cross section can be factorized as the product of the inclusive single diffraction cross section and the ratio of the pomeron-proton cross section for producing jets and the cross section for producing anything,

$$\frac{d\sigma_{jj}}{dtdM_X^2} = \frac{d\sigma_{SD}}{dtdM_X^2}\frac{\sigma(\mathbb{P}p \to jj)}{\sigma(\mathbb{P}p \to X)} \tag{2.4}$$

Here, $d\sigma_{SD}$ can be taken as the parameterization of data in Eq. 2.3 and the total pomeron-proton cross section $\sigma(\mathbb{P}p \to X)$ can be determined from elastic and soft-diffraction data using the Regge formalism, resulting in a value of order 1 mb. Together these two parts of Eq. 2.4 can be interpreted as an expression for a *pomeron flux* $f_{\mathbb{P}/p}(\xi, t)$ in the proton. The cross section for pomeron-proton to jets, $\sigma(\mathbb{P}p \to jj)$, is assumed to be given by pQCD as

$$\sigma(\mathbb{P}p \to jj) = \int dx_1 dx_2 d\hat{t} \sum_{ij} f_{i/\mathbb{P}}(x_1, Q^2) f_{j/p}(x_2, Q^2) \frac{d\hat{\sigma}}{d\hat{t}} \tag{2.5}$$

where $\hat{\sigma}$ and $\hat{t}$ are the cross-section and the four-momentum transfer respectively for the elementary reaction among partons; a parton density function $f_{i/\mathbb{P}}$ for the pomeron is introduced in a similar way to those for ordinary (real) hadrons. Assuming the pomeron to be gluon-dominated it is reasonable to try $xg(x) = ax(1-x)$ or $xg(x) = b(1-x)^5$ for the case of only two gluons or of many, in analogy with the proton [9]. In the same way, if the pomeron were essentially a $q\bar{q}$ system one would guess $xq(x) = cx(1-x)$. The normalization constants a, b, c can be chosen to satisfy the momentum sum rule $\int_0^1 dx \sum_i x f_{i/\mathbb{P}}(x) = 1$, which seems like a rational assumption.

A Monte Carlo simulation based on the formalism described above reveals a clearly observable event signature: a leading proton ($x_F \gtrsim 0.9$) separated by a large rapidity gap from a central hadronic system with high-P_T jets. In 1987 this striking event signature was observed by the UA8 experiment [10] signaling the discovery of

diffractive hard scattering phenomena, which were studied further with more data [11, 12].

The jets detected by UA8 exhibited the distinctive properties of QCD jets, e.g. jet E_T and angular distributions and energy profiles. The longitudinal momentum of the jets provides information on the momentum fraction, β, of the parton in the pomeron. A change in the shape of the β-distribution shifts the parton-parton center-of-mass system (c.m.s.) with respect to the c.m.s. of the diffractive system X and thereby the momentum distribution of the jets [9]. Comparison of data and Monte Carlo indicates a preference for a hard parton distribution in the pomeron [11].

Gluon and quark contributions inside the pomeron cannot be separately measured using the UA8 data only. The UA1 experiment reported some evidence for diffractive heavy flavor, charm and bottom, production [13, 14]. This may be explained by a gluon-dominated pomeron such that the $gg \to b\bar{b}$ subprocess can be at work, but no ultimate conclusion could be made given the normalization uncertainty in the model and the experimental errors [15].

2.4 Rapidity Gap Events at HERA and the Tevatron

The pomeron model of diffractive hard scattering described above can be naturally extended to other types of particle collisions, $p + a \to p + X$ where a is a lepton or a photon. Based on the factorization hypothesis [9, 16] the cross section is given by

$$d\sigma(p + a \to p + X) = f_{\mathbb{P}/p}(\xi, t)\sigma(\mathbb{P} + a \to X) \tag{2.6}$$

The pomeron flux can be taken as a simple parameterization of data in terms of exponentials as above (see Eq. 2.3), or derived from Regge phenomenology in the

form [17]

$$f_{\mathbb{P}/p}(\xi,t) = \frac{9\beta_0^2}{4\pi^2}[F_1(t)]^2 \left(\frac{1}{\xi}\right)^{2\alpha_{\mathbb{P}}(t)-1} \tag{2.7}$$

with parameters determined from hadronic inclusive diffractive scattering experiments. Here, β_0 is the effective pomeron-quark coupling and $F_1(t)$ is a proton form factor given by

$$F_1(t) = \frac{4m_p^2 - 2.8t}{4m_p^2 - t}\left(\frac{1}{1 - t/0.7}\right)^2, \tag{2.8}$$

where m_p is the proton mass. For the hard scattering cross section $\sigma(\mathbb{P} + a \to X)$ one should use the relevant convolution of parton densities and parton cross sections, e.g. Eq. 2.5 for hadron-pomeron collisions.

In Ref. [9], it was proposed to study the pomeron structure with deep inelastic scattering (DIS) at HERA, an electron-proton collider. DIS is a clean process with a well understood point-like probe with high resolving power. In diffractive DIS the experimental signature should be very clear: a quasi-elastically scattered proton (going down the beam pipe) well separated by a rapidity gap from the remaining hadronic system. The kinematics is described by the diffractive variables ξ and t, and the standard DIS variables $Q^2 = -q^2 = -(p_e - p_{e'})^2$ and Bjorken $x = Q^2/(2P \cdot q)$, where $P, p_e, p_{e'}, q$ are the four-momenta of the initial proton, initial electron, scattered electron and exchanged photon, respectively.

In terms of the above kinematical variables, the cross section for diffractive DIS can be written as a generalization of non-diffractive formula

$$\frac{d\sigma(ep \to epX)}{dx dQ^2 d\xi dt} = \frac{4\pi\alpha^2}{xQ^4}\left(1 - y + \frac{y^2}{2}\right) F_2^{D(4)}(\beta, Q^2, \xi, t) \tag{2.9}$$

where $F_2^{D(4)}$ is the diffractive proton structure function. Assuming sea factorization, $F_2^{D(4)}$ can be expressed as the product of a function which depends on ξ and t and a

function which depends on β and Q^2

$$F_2^{D(4)}(x, Q^2, \xi, t) = g(\xi, t) F_2^{2D}(\beta, Q^2) \tag{2.10}$$

where the pomeron structure function F_2^{2D} is given by the densities of (anti)quarks of flavor f

$$F_2^{2D}(\beta, Q^2) = \sum_f e_f^2 \left[\beta q_f(\beta, Q^2) + \beta \bar{q}_f(\beta, Q^2)\right] \tag{2.11}$$

In DIS gluons only enter indirectly through the process $g \to q\bar{q}$, because the photon does not couple directly to gluons. The above formulae do not depend on Regge theory but are generalizations of non-diffractive formulae. In terms of the Ingelman-Schlein pomeron model [9], the functions $g(\xi, t)$ and $F_2^{2D}(\beta, Q^2)$ can be interpreted as the pomeron flux factor and the pomeron structure function respectively.

Although diffractive DIS had been predicted, it was a big surprise for many when it was observed first by ZEUS [18] and then by the H1 collaboration [19]. The observed gap events have the same Q^2 dependence as normal DIS and are therefore not some higher twist correction. The overall measured rate of gap events is about 10% of all events, so that it is not a rare phenomenon.

Based on Eq. 2.9, the diffractive structure function $F_2^{D(4)}$ is extracted from the cross section of rapidity gap events. Since t is not measured it is effectively integrated out, giving the observable $F_2^{D(3)}(\xi, \beta, Q^2)$. Study of $F_2^{D(3)}$ shows that to a first approximation the ξ dependence factorizes [19] and is of the form $1/\xi^n$ with $n = 1.19 \pm 0.06(stat) \pm 0.07(syst)$. This is in general agreement with the expectation $f_{\mathbb{P}/p} \sim 1/\xi^{2\alpha_{\mathbb{P}}(t)-1} \simeq 1/\xi^{1.23+0.52t}$ from the pomeron Regge trajectory above.

However, after collecting more data in an extended kinematic range, deviations from sea factorization were observed [20]. The power of ξ in $F_2^{D(3)}$ was found to depend on β. One way to accommodate this is to introduce a sub-leading reggeon

($\mathbb{R}$) exchange with expected trajectory $\alpha_{\mathbb{R}}(t) \simeq 0.55 + 0.9t$ and quantum numbers of the ρ, ω, a or f meson [20]. A fit to diffractive DIS data yields the intercept $\alpha_{\mathbb{R}}(0) = 0.50 \pm 0.19$, in agreement with expectation, but $\alpha_{\mathbb{P}}(0) = 1.20 \pm 0.04$ which is significantly larger than the 1.12 obtained from soft hadronic cross section. In this two reggeon scenario there is no evidence for a β or Q^2 dependence in these intercepts and one can therefore integrate over ξ, resulting in the measurement of $F_2^D(\beta, Q^2)$. This quantity can be interpreted as the structure function of the exchanged color singlet object, which is mainly the pomeron. The F_2^D is essentially scale independent, i.e. almost constant with Q^2. The small Q^2 dependence is actually compatible with being logarithmic as in normal QCD evolution, although the rise with $\ln(Q^2)$ persists up to large values of β, in contrast to the proton structure function. There is only a weak dependence on β, so that the partons are quite hard compared to the case of ordinary hadrons. These features are in accordance with a large, $80 - 90\%$, gluon component of the diffractive exchange, as confirmed by a quantitative QCD analysis [20].

At the Tevatron, diffractive events in $\bar{p}p$ scattering were also observed by selecting events with a rapidity gap and/or a leading antiproton. Several processes were studied, including single diffraction dissociation with dijet production [21, 22], diffractive production of W bosons [23], bottom quarks [1] and events with a rapidity gap between two jets [24, 25]. The fraction of diffractive events for a given process (relative to the inclusive cross-section for the same process) is about 1%. Comparisons of the observed rates with the predictions obtained using the factorization formalism described above and the parton distributions as determined from the HERA data indicate a substantial difference. The cross-sections measured at the Tevatron are about a factor of $5 - 6$ smaller. A similar study of events with a central dijet system and rapidity gaps on both sides [26], which can be interpreted as interactions of two

pomerons, leads to a factor of $10 - 100$ with respect to the expectation based on factorization. By comparing the results of diffractive W, dijet and b-quark production [1] the gluon fraction of the pomeron was evaluated to be $0.54^{+0.16}_{-0.14}$.

2.5 Problems of the Pomeron Model

The failure to describe the data on hard diffraction from both HERA and the Tevatron with the same pomeron model raises questions on the universality of the model, e.g. concerning the pomeron flux and structure function. A possible solution to this problem has been proposed in terms of a pomeron flux *renormalization* [4]. In this model the prediction for HERA is not affected, but at the higher energy of the Tevatron the pomeron flux is reduced and the data are essentially reproduced. In another proposal [27] based on an analysis of single diffraction cross sections, the pomeron flux is reduced at small ξ through a ξ- and t-depending damping factor.

A third proposal attempts to explain the discrepancy between diffraction in ep and $\bar{p}p$ by the possibility for coherent pomeron interactions in the latter [28]. In the case of an incoherent interaction, only one parton from the pomeron participates and all others are spectators. But, in the pomeron-proton interaction with $\mathbb{P} = gg$ both gluons may take part in the hard interaction, giving a coherent interaction. In DIS, the coherent interaction cannot occur in the same way because the pomeron interacts with a particle without colored constituents. This difference between ep and $\bar{p}p$ indicates that there should be no complete universality of parton densities in the pomeron.

Although modified pomeron models may explain the rapidity gap event rates reasonably well, there is still no adequate understanding of the pomeron and its

interaction mechanisms. There are problems with the very concept of pomeron. The concept of structure function is not well defined for a virtual particle and, in particular, it is unclear whether a momentum sum rule should apply. In fact, since only the product is an observable quantity, the factorization into a pomeron flux and a pomeron structure function cannot be uniquely defined.

Chapter 3

Charmonium Production

There are two dominant processes that contribute to the production of charmonium states in high energy $\bar{p}p$ collisions. The first is known as *direct production*, when a $c\bar{c}$ pair is produced from the initial particle collision, and the two quarks combine producing a colorless bound state. Another process is the production of a bottom quark fragmenting into a B hadron, which can subsequently decay into ψ and other hadrons. This production process is further referred as B *production*. In high energy colliders the charmonium production is called *prompt* if the point at which the state is produced can not be resolved using a vertex detector from the interaction point of the colliding beams. The prompt charmonium states include states produced directly and from the decay of a higher mass charmonium state, i.e. J/ψ's from electromagnetic decay of χ_c mesons. The ψ's produced from the B-hadron decay is an example of non-prompt source of charmonium.

3.1 Direct Production

The leading order diagrams for direct ψ and χ_c production in $\bar{p}p$ collisions are presented in Fig. 3.1. The $c\bar{c}$ quarks are produced in a color-singlet state, and the entire diagram can be calculated, except for the "blob" denoting the hadronization process of the quarks into a ψ or χ_c meson. The ψ diagram can be calculated up to a factor related to the amplitude of the non-relativistic ψ wave function at the origin, $|\psi(0)|^2$. The value of the wave function at the origin can be determined from the ψ leptonic decay width. The partial width for the decay $\psi \to l^+l^-$ derived from the diagram in Fig. 3.2 is given by [29]

$$, _{l^+l^-} = \frac{16\pi\alpha^2Q^2}{M_\psi}|\psi(0)|^2 \tag{3.1}$$

where $l = e, \mu, \tau$ and $Q = \frac{2}{3}$ is the charm quark charge. The photon propagator gives a factor of $1/q^2 = 1/M_\psi^2$, where q is the momentum carried by the photon. The $l^+l^-\gamma$ vertex enters as $\sqrt{4\pi\alpha}$ and the $c\bar{c}\gamma$ vertex contributes a factor of $Q\sqrt{4\pi\alpha}$, yielding

$$|\mathcal{M}|^2 \propto \frac{\alpha^2Q^2}{M_\psi^4} \tag{3.2}$$

The integral over the lepton phase space is proportional to $q^2|\psi(0)|^2$, leaving the $1/M_\psi^2$ dependence. All of the quantities on the right hand side of the Eq. 3.1 are known except for the wave function. Therefore, a measurement of $, _{l^+l^-}$ provides a measurement of the ψ wave function at the origin.

There is a similar production mechanism which only contributes to J/ψ production. The $c\bar{c}$ pair can form a χ_c state, which then decays to a J/ψ through an electromagnetic transition, $\chi_c \to J/\psi\gamma$.

As seen in Fig. 3.1, the ψ production diagrams contain charm quark loops which are connected to three gluons, while the quark loops in the χ_c production

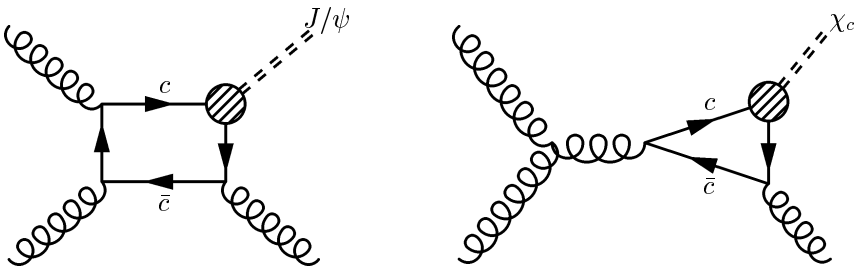

Figure 3.1: *Leading order diagram for (left) J/ψ and (right) χ_c production.*

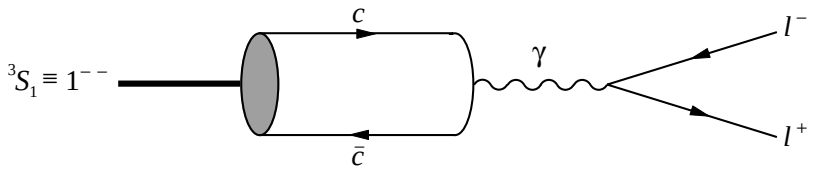

Figure 3.2: *Leading order diagram for ψ decay into l^+l^- via virtual photon.*

diagrams are connected to only two. This is a result of G-parity conservation[1] low. Since the gluon has negative G-parity, a state consisting of N gluons has $G = (-1)^N$. As a result, the ψ, with odd G-parity, only couples to states with an odd number of gluons, while the χ_c, with even G-parity, can only couple to states with an even number of gluons.

3.2 Fragmentation Production

The described model of charmonium production in which a bound $c\bar{c}$ state is produced in the color singlet configuration is usually referred to as Color Singlet Model (CSM). This model alone is not able to describe charmonium hadroproduction. In particular, the predicted by CSM cross sections fall off much more rapidly with transverse momentum than the cross sections measured at the Tevatron [30].

[1] G-parity is a quantity conserved by strong interactions. It is simply a combined operation of charge conjugation and a rotation in isospin space.

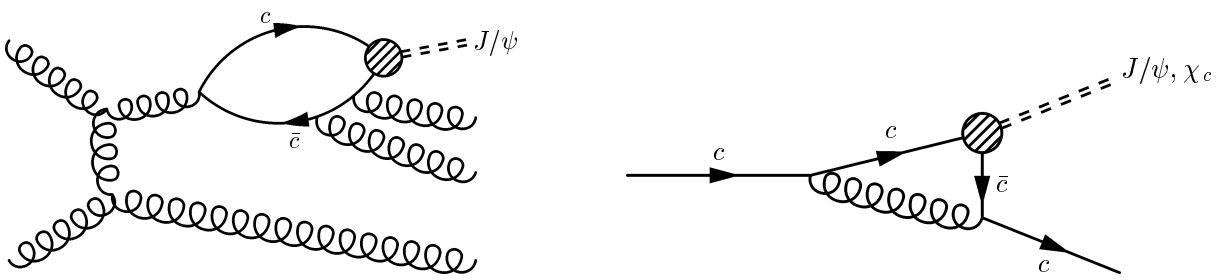

Figure 3.3: *Gluon(left) and charm (right) fragmentation production of ψ in the color singlet model.*

However, two effects can significantly enhance the predicted cross section for direct charmonium production at high P_T. One is the parton *fragmentation* contribution which represents a dominant source of prompt quarkonia at high energies [31]. Figure 3.3 shows a Feynman diagram involved in ψ production via gluon fragmentation which is $\mathcal{O}(\alpha_S^5)$. Given that the leading order diagram (see Fig. 3.1) is $\mathcal{O}(\alpha_S^3)$, the contribution from this diagram to the total ψ cross section should be significantly suppressed. Nevertheless, if the ψ has a sufficiently large transverse momentum $P_T \gg M_\psi$, then the diagram will be dominated by configurations where the gluon has $Q^2 \sim M_\psi^2 \ll E_{\text{gluon}}^2$. In this case the gluon is nearly real, and diagram is enhanced by a factor of $(P_T/M_\psi)^2$. When P_T becomes large enough this diagram starts dominating over the leading order diagrams. Because this process produces a (nearly) on-shell gluon which fragments into a ψ, it is referred to as gluon fragmentation production. The same mechanism also contributes to production of χ_c mesons. Actually, for the χ_c, one less gluon needs to be emitted, so the process is $\mathcal{O}(\alpha_S^4)$. A ψ can also be produced by a fragmentation process where a charm quark fragments, as shown in Fig. 3.3, although this is not as essential, because the production of a charm quark is substantially suppressed in comparison with the gluon production.

3.3 Color Octet Model

Up to this point, all considered perturbative processes have produced a color-singlet $c\bar{c}$ pair which hadronizes into a ψ or χ_c. In the Color Singlet Model the radiated gluons cannot be too soft, or perturbation theory will fail. A few years ago, Bodwin, Braaten and Lepage developed a general factorization formalism for heavy quarkonium production, which is based on the non-relativistic QCD model (NRQCD) [32], an effective potential model, inspired by Heavy Quark Effective Theory (HQET) [33, 34, 35]. In this framework, charmonium production is described as two-step process: $c\bar{c}$ pair production at perturbative level and the subsequent evolution to colorless vector meson through soft gluon emission at the non-perturbative domain. This argument is advocated by the fact that the $c\bar{c}$ pair is produced at distance $1/m_c$, m_c standing for heavy quark mass, which is much smaller than $1/\Lambda_{QCD}$, the typical QCD scale for bound-state system. According to the color octet model formulation [36], the wave function of an S-wave quarkonium state in terms of Fock state decompositions is given by

$$\begin{aligned} |\psi_Q\rangle =& \mathcal{O}(1)|Q\bar{Q}[^3S_1^{(1)}]\rangle + \mathcal{O}(v)|Q\bar{Q}[^3P_J^{(8)}]g\rangle + \mathcal{O}(v^2)|Q\bar{Q}[^1S_0^{(8)}]g\rangle + \\ & \mathcal{O}(v^2)|Q\bar{Q}[^3S_1^{(8)}]gg\rangle + ... \end{aligned} \tag{3.3}$$

where v is a typical relative velocity of constituent quarks in quarkonium state. Here, the usual spectroscopic notation, $^{2S+1}L_J$, is used, and the color state is indicated by (1) for singlet and (8) for the octet. Inside a charmonium state, the two quarks are moving fairly slowly, with $v_c^2 \approx 0.25$. Thus, a double expansion, in powers of α_S and v_c, similar to Eq. 3.3 is possible. The terms that are of lowest order in v_c, so that which terms dominate the cross section depends upon the power of both α_S and v_c. Since the $c\bar{c}$ pair is often produced as a color octet state in this model, the model is

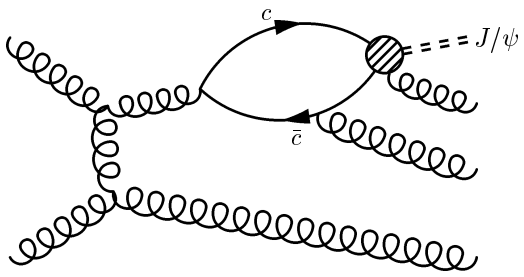

Figure 3.4: *Gluon fragmentation production of ψ in the color octet model. In this case, one gluon is radiated during the non-perturbative process.*

named the Color Octet Model (COM).

As in case of CSM, the entire process cannot be calculated using perturbation theory. However, a non-perturbative part can be factored out. This part is a well-defined matrix element, which could be calculated using lattice QCD, or extracted from experimental measurements. It can be argued that the matrix element is independent of the kinematics in the perturbative part, which results in an unknown normalization, but does not affect the spectrum. Moreover, the matrix elements are *universal*, so a matrix element measured at one experiment can be used to make predictions for another experiment, or compared with the matrix element measured at that experiment. Finally, naive power counting provides an order of magnitude estimate for the matrix element. In terms of Feynman graphs, what happens is that one or more of gluons radiated from the $c\bar{c}$ pair is removed from the perturbative portion, and added to the non-perturbative portion, as shown in Fig. 3.4. The gluon can become extremely soft, greatly enhancing the contribution of the diagram. In fact, a typical approximation is to assume that the gluon carries no energy, only the excess color.

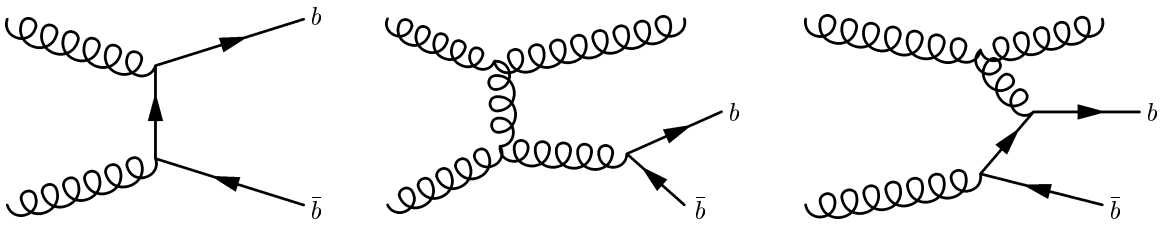

Figure 3.5: *Feynman diagrams for b production from gluon fusion (left), gluon splitting (center) and flavor excitation (right).*

3.4 B Production

The other mechanism for ψ production is the decay of B hadron. The initial interaction produces a b quark, which fragments into a B hadron that subsequently decays into a ψ and other particles. At next-to-leading order, the diagrams for b quark production can be grouped into three classes, shown in Fig. 3.5. Each of these processes has distinct characteristics. The first diagram represents the process of gluon fusion. The $b\bar{b}$ pair produced by this reaction is separated by 180° in azimuthal angle, and results in two well separated jets. Gluon splitting (second diagram) tends to produce b quarks which are close together, as the mass of the virtual gluon tends to be small. As a result, the decay products of the two quarks may appear to come from a single parent, especially after fragmentation effects and experimental resolution are included. The third class, flavor excitation, is often the result of the gluon scattering off one of the virtual b quarks that form the cloud around the valence quarks. In this case, the other b proceeds close to the initial proton or anti-proton direction.

After the b quark fragments into a B hadron, it can decay to a ψ or χ_c through diagrams such as Fig. 3.6. This decay is suppressed relative to the decay $B \to DX$ for several reasons. First, the W must decay into $\bar{c}s$, while for the $B \to DX$ decay, all possible W decay modes are allowed. This reduces the rate by about a

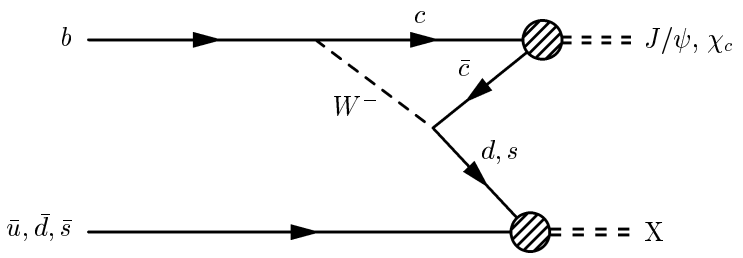

Figure 3.6: *Typical B meson decay diagram for charmonium production.*

factor of three. Additionally, the $\bar{c}$ must have the same color as the c quark, as the fragmentation of the color octet $c\bar{c}$ state into charmonium is suppressed. This leads to another factor of three. Finally, the c and $\bar{c}$ quarks must have similar momenta, so that they can form a bound state. This results in the relatively small branching ratios of $\mathcal{B}(B \to J/\psi X) = 1.13 \pm 0.07\%$ and $\mathcal{B}(B \to \psi(2S)X) = 0.34 \pm 0.05\%$ [37]. While these branching ratios are small, it is an experimental fact that the two muons from ψ decay provide an excellent experimental trigger, so the process $B \to \psi X$ is tremendously useful from a practical standpoint.

At the Tevatron, the fraction of ψ mesons originating from B-hadron decays ranges from 15% to 40% of all ψ's with $P_T^{\psi} > 5$ GeV produced in the central pseudo-rapidity region, $|\eta| < 0.6$, as reported by CDF Collaboration [30]. The study of B-hadron decay contribution presented in Section 6.9 is of special importance for the analysis of this dissertation, since it provides an algorithm to disentangle prompt J/ψ's from B production.

3.5 Charmonium Spectroscopy

Naively, one would expect that charmonium decays quickly, as the $c\bar{c}$ pair would annihilate into gluons, producing a broad resonance. While this does happen,

it occurs at a lower rate than in other strong decays, due to several factors. After the $c\bar{c}$ pair annihilates into gluons, one or more of the resulting gluons must carry away most of the energy, about 3 GeV. This is a high enough energy that α_s is fairly small, which reduces the rate for the process. Besides, color conservation requires that at least two gluons be emitted. In the above discussion of a ψ production, we saw that G-parity prohibits the production of a ψ from two gluons, thereby requiring three gluons. The same is true for the ψ decay - again, three gluons are required. As a result, the decay is a higher order process than are most other strong decays, since most strong decays exchange only one soft gluon. Finally, three body phase-space is highly suppressed relative to two body phase-space, i.e., the kinematics involved discourage three body decays.

The combination of all of these factors suppress the rate at which this strong force decay takes place. Electromagnetic decays, in which either the pair annihilates into a virtual photon, or a real photon is emitted, form a significant fraction of the decays of many charmonium states [2].

The internal dynamics of the charmonium system are similar to those of the positronium system. One difference is that, while positronium is bound together by exchange of soft photons, charmonium is bound by exchange of soft gluons. Therefore, while accurate calculations are possible for the energy levels of positronium, similar calculations for the masses of charmonium states are much more difficult. However, the quantum numbers that are used to describe positronium can also be applied to charmonium. The rotational quantum number in positronium results from the rotational invariance of the potential, while the radial quantum number is the number

[2] One exception is states with masses larger than twice the D-meson mass. These states decay almost exclusively into $D\bar{D}$. Since such decays proceed by the exchange of one soft gluon, the rate for these decays is much higher than the rate of radiative decays to other charmonium states.

of nodes of the radial wave function plus 1. The QCD quark-quark potential has similar properties, so similar quantum numbers exist, although the dependence of the energy levels is different [3].

The lightest charmonium state is the η_c. In an η_c, the $c\bar{c}$ pair is in an S-wave state, with the quark spins anti-parallel. The next higher state is the J/ψ, which is the S-wave state with parallel spins. The excited S-wave states are sometimes denoted by ψ(nS) or by ψ', ψ'', etc. The P-wave states with parallel spins are denoted as χ_{cJ}, where $J = 0, 1, 2$ is the total angular momentum of the state. χ_c is a generic term that refers to any of the χ_{cJ}. By radiating a photon, a χ_c meson may decay into a lower energy J/ψ state, thus resulting in contribution to prompt J/ψ production. The fraction of J/ψ mesons from χ_c decays measured at the Tevatron amounts to about 30% [38] of all prompt J/ψ's and slightly varies with $P_T^{J/\psi}$. Other excited states, such as the P-wave spin singlet, and D-wave states, are expected to exist, but are not expected to contribute significantly to ψ production [4]. Figure 3.7 shows the mass spectra of charmonium family and transitions between $c\bar{c}$ states.

3.6 Summary

In conclusion, J/ψ mesons can be produced in high energy $\bar{p}p$ collisions through three mechanisms:

- The hard scattering can create a $c\bar{c}$ pair, which forms a bound state, directly producing a J/ψ particle.

[3] Just as in positronium, the spin-orbit coupling breaks the rotational symmetry. While the effect is larger than it is in positronium, it can still be treated as a small perturbation.

[4] Feed down from P-wave singlet is suppressed, because of the need to flip the spin of one of the quarks, and the decay of a D-wave state to a ψ requires $\Delta L = 2$, which is suppressed by an additional power of α.

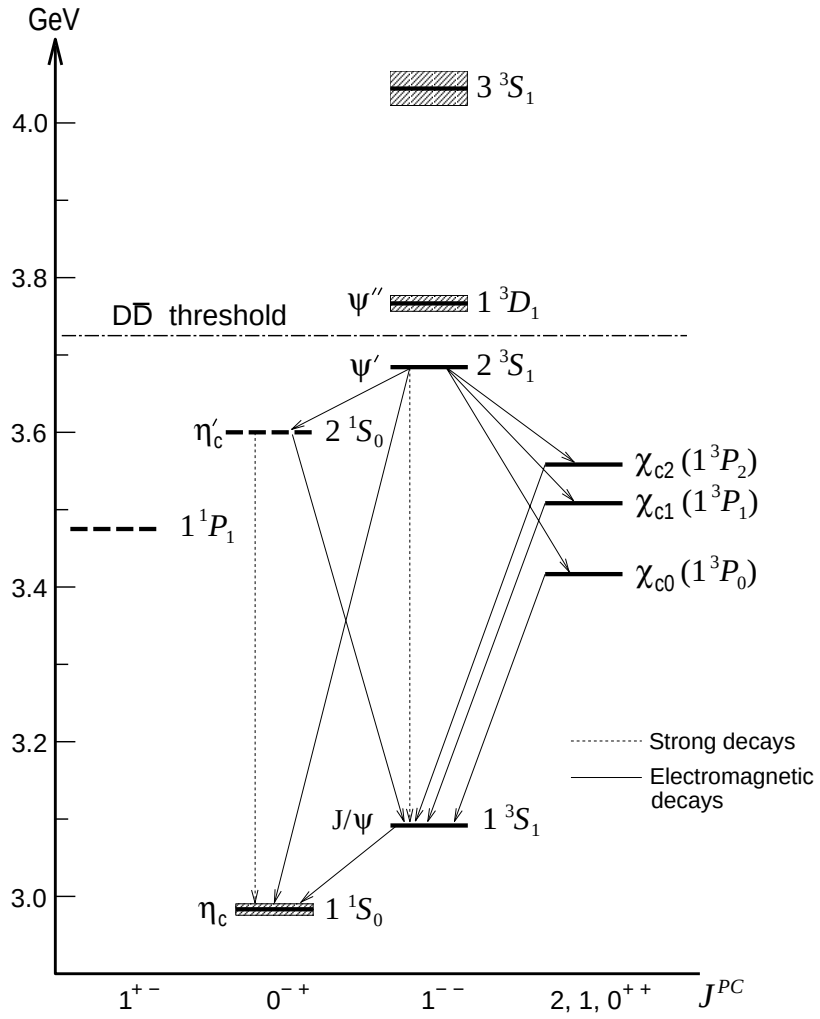

Figure 3.7: *Observed and expected transitions of charmonium states.*

- When the $c\bar{c}$ pair binds together, the resulting bound state can be a χ_c meson, which can decay to J/ψ by emitting a photon.

- A $b\bar{b}$ pair may be produced in the interaction. After fragmentation forms a B hadron, the hadron can decay to J/ψ or χ_c plus anything, with χ_c decaying to J/ψ plus photon.

At charmonium high transverse momentum, gluon fragmentation is the dominant process of producing the $c\bar{c}$ pair for the first two mechanisms, even though it is a higher-order process. In general, gluons play a major role in J/ψ hadroproduction, making this process a unique tool for studying the gluonic content of the pomeron.

Chapter 4

The Tevatron and Collider Detector

The data used in this analysis were collected by CDF during Tevatron runs that took place from January 1994 until the end of July 1995, collectively called Run 1B. The integrated luminosity accumulated by CDF during this run was $(89 \pm 4)\text{pb}^{-1}$.

4.1 Accelerator Complex

Figure 4.1 shows the steps required to generate the 900 GeV beams of protons and antiprotons. The process for producing the protons starts with hydrogen gas, which is ionized by adding electrons. The negative hydrogen ions are accelerated to 750 KeV using a Cockroft-Walton electrostatic accelerator, and then to 400 MeV in a linear accelerator called Linac, which is approximately 500 feet long. Before entering the Booster accelerator, the ions are passed through a copper foil which removes the electrons, leaving only the protons. Located nearly 20 feet below ground, the Booster is a rapid cycling synchrotron 500 feet in diameter. It uses magnets to deflect electrically charged particles in a circular path so that they experience the repeated action of accelerating electric fields during each revolution. The protons

travel around the Booster about 20,000 times and their energy is raised to 8 GeV. The Booster normally cycles twelve times in rapid succession, injecting twelve pulses, or bunches, of roughly 10^{11}protons, into the Main Ring, the next stage of the accelerating process. The Main Ring is a synchrotron two kilometers in diameter that uses conventional magnets and accelerates protons to 150 GeV.

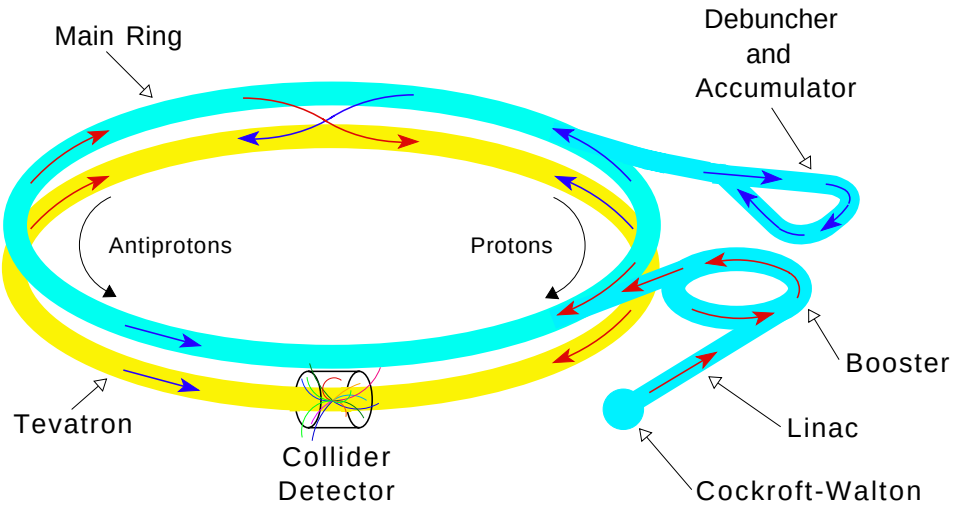

Figure 4.1: *Schematic view of the Fermilab accelerator complex for $\bar{p}p$ collisions.*

The process of producing antiprotons is more complex. A beam of protons accelerated to 120 GeV is taken from the Main Ring and focused onto a tungsten target. The antiprotons are selected from the spray of the produced secondary particles and transfered to the Debuncher, where the dimensions and energy spread of the antiproton beam are reduced using the debunching technique and a process known as stochastic cooling [39]. From the Debuncher, the antiprotons are transfered to the Accumulator ring, where they are stored. When enough antiprotons are stored they are injected into the Main Ring and accelerated to 150 GeV. Now the process of colliding beams of protons and antiprotons can begin.

Once the protons and antiprotons reach energies of 150 GeV, six bunches

of protons and six bunches of antiprotons are injected into the Tevatron in opposite directions, where they are accelerated simultaneously to an energy of 900 GeV. Each bunch of protons and antiprotons has approximately 2×10^{11} and 3×10^{10} particles, respectively. The Tevatron consists of superconducting magnets located directly below the Main Ring in the same tunnel. The proton and antiproton bunches share the same magnetic and RF fields and travel within the same beam pipe. Quadrupole magnets bring the two beams to collision at the center of the CDF detector, located in the B0 collision hall. At the B0 collision point the beam bunches are approximately circular in cross section with a radius of 30 μm at 1σ. Longitudinally, the bunches have a roughly Gaussian shape of 30 cm width.

The number of collisions per second, N, at the CDF interaction region is given by

$$N = \sigma \times \mathcal{L} \tag{4.1}$$

where σ is the cross section of the proton-antiproton collisions and $\mathcal{L}$ the instantaneous luminosity of the colliding beams. The instantaneous luminosity is given by

$$\mathcal{L} = \frac{N_p N_{\bar{p}} f}{4\pi\sigma^2} \tag{4.2}$$

where N_p and $N_{\bar{p}}$ are the numbers of protons and antiprotons per bunch, respectively, f is the frequency of bunch crossing, and σ the r.m.s. width of the beam transverse profile at the interaction point.

For Run 1B, the maximum instantaneous luminosity achieved was 2.8×10^{31} cm^{-2}s^{-1}, with typical values of 1.6×10^{31} cm^{-2}s^{-1}. The total integrated luminosity, $\int \mathcal{L}dt$, of beam delivered to the CDF interaction region during Run 1B was about 126 pb^{-1}, where 1 pb^{-1} = 10^{36} cm^{-2}.

4.2 The CDF Detector

The Collider Detector at Fermilab (CDF) is a multipurpose detector designed to measure the properties of particles emerging from high-energy $\bar{p}p$ collisions at the Tevatron Collider. The detector has azimuthal and forward/backward polar symmetry and covers 98% of the 4π solid angle. A quarter view schematic drawing of the CDF detector is shown in Figure 4.2.

The CDF employs a conventional right-handed coordinate system with its origin at the center of the detector, which is also the nominal interaction point for $\bar{p}p$ collisions. The positive z-axis lies along the beam line in the proton direction, West to East, the positive y-axis points vertically upward, and the positive x-axis points radially outward in the horizontal plane of the Tevatron ring. The polar angle θ is determined from the positive z-axis. The azimuthal angle ϕ is an angle in the $x-y$ plane measured from the positive x-axis toward the positive y-axis. The radius r indicates the distance from the z-axis. The pseudorapidity is defined in terms of the polar angle θ by the relation $\eta = -\ln(\tan(\theta/2))$.

The CDF detector is composed of several specialized devices each designed for a specific task in determining the properties of particles produced in $\bar{p}p$ collisions, such as type, charge, momentum, energy, charged particle trajectory, etc. The detector is made up of three main functional sections: tracking detectors, calorimeters and muon detectors. Starting from the interaction point and moving radially outward, the tracking systems reside inside a solenoidal magnetic field of about 1.4 T, generated by a superconducting solenoidal magnet 3 m in diameter and 4.8 m long. The magnetic field causes the trajectory of a charged particle to bend. The curvature of the trajectory is used to measure the momentum and charge of the particle. In addition, the

tracking systems provide a measurement of the vertices from which charged particles originate in a given event.

The tracking chambers are surrounded by calorimeters used to measure the electromagnetic and hadronic energy of the emerging particles, both charged and neutral. The outermost detectors are the muon detectors. The calorimeters and layers of steel in front of the muon chambers absorb hadrons, so the muons can be clearly identified by the muon systems.

The following sections present a brief overview of the CDF detector components which are important to this analysis. A more complete description of the detector can be found in [40].

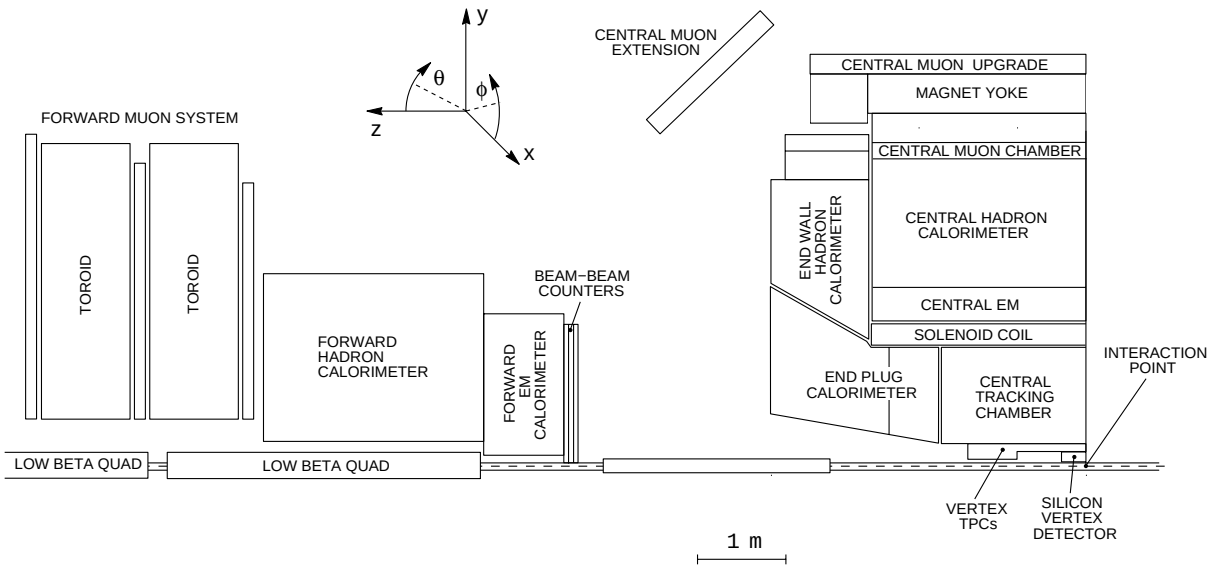

Figure 4.2: *Side-view cross section of one quadrant of the CDF detector, displaying its main components.*

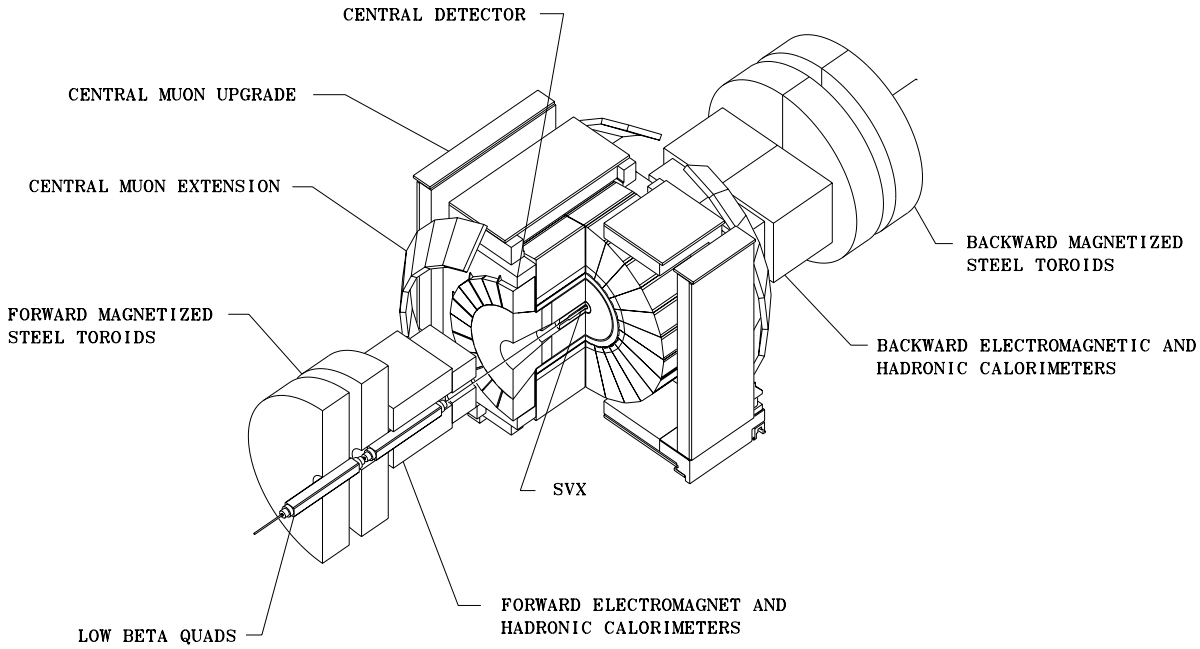

Figure 4.3: *Perspective view of the CDF detector.*

4.2.1 Tracking Detectors

The CDF tracking system comprises four detectors: the Silicon Vertex Detector (SVX), the Vertex Time Projection Chamber (VTX), the Central Tracking Chamber (CTC), and the Central Drift Tube (CDT) array. All of these detectors are placed inside a solenoidal magnetic field of 1.4 T. Each tracking detector is designed to perform a particular task. The SVX, which is closest to the beam pipe, has the best position resolution and is used to identify displaced decay vertices indicating the decay of a B hadron. The VTX surrounds the SVX and is primarily used to measure the z position of an event's interaction point, its *primary vertex*. The CTC was designed for precise measurement of a charged particle's momentum and to give good two-track separation.

Silicon Vertex Detector

The Silicon Vertex Detector (SVX) [41] is located right outside the 1.9 cm radius beryllium beam pipe. It consists of two identical cylindrical modules, referred to as barrels, that are aligned end-to-end along the beam direction. There is a 2.15 cm gap between the two barrels at $z = 0$. An isometric view of one of the SVX barrels is shown in Figure 4.4. The total active length of the detector is 51.5 cm providing a pseudorapidity coverage of $|\eta| < 1.9$. Since the $\bar{p}p$ collisions occur with a spread of $\sigma \simeq 30$ cm about $z = 0$, due to the longitudinal size of the proton and antiproton bunches, the track acceptance of the SVX is only about 60%.

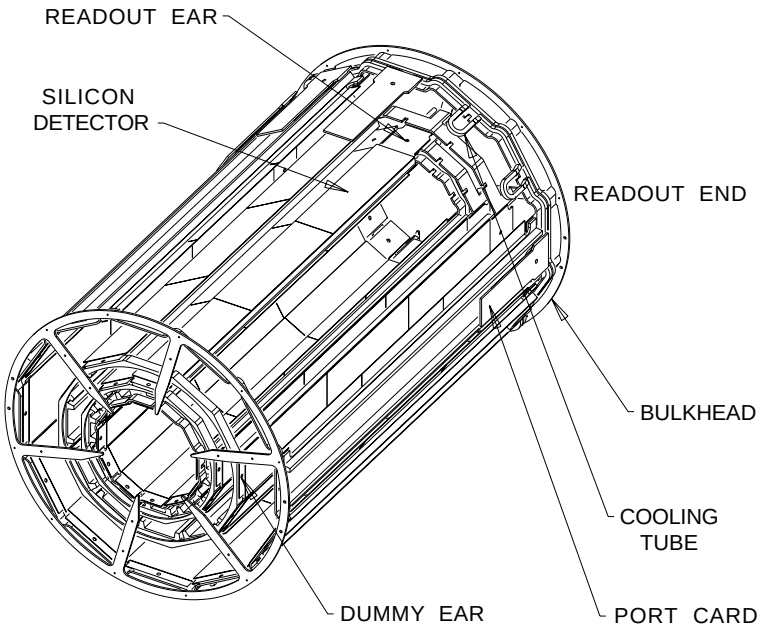

Figure 4.4: *An isometric view of one of the SVX barrels.*

Each barrel consists of four concentric layers of silicon strip detectors segmented into twelve flat *ladders* that cover 30° in azimuth. The innermost layer is at a distance of 2.86 cm and the outermost layer is at a distance of 7.87 cm from the beam pipe. Each ladder has three 8.5 cm long single-sided silicon strip detectors

with the readout strips running parallel to the beam line. The strip pitch is 60 μm for the inner three layers and 55 μm for the outer layer. Axial microstrips provide precision track reconstruction with a single hit position resolution of 12 μm and an asymptotic impact parameter resolution of 13 μm. The SVX has a total of 96 ladders. The ladders are read out by chips, each of which is responsible for 128 channels (strips). The entire SVX detector has a total of 46080 channels, nearly one third of all the channels for the whole CDF detector. The channels for each wedge are read out in parallel and in a *sparse mode*, meaning that only channels which have a signal above some threshold are read out. With typical occupancies $\approx 5\%$, readout times are about 2 ms, the longest among the CDF detector subsystems.

Vertex Time Projection Chamber

The Vertex Time Projection Chamber (VTX) is a gas drift chamber that surrounds and provides mechanical support for the SVX detector. The VTX is 2.8 m long in z and extends to a radius of 22 cm from the beam pipe, providing a pseudo-rapidity coverage of $|\eta| < 3.5$. It consists of 28 drift modules filled with a 50%/50% mixture of argon/ethane gas. Each drift module has a central high voltage grid that divides it into two 5 cm long drift regions. These modules are mounted end-to-end along the beam direction. Each module is further subdivided into 8 wedges, or octants, each covering 45° in azimuth. There are 24 sense wires in each drift region of the 10 end modules. The 18 inner modules have only 16 sense wires in each drift region, due to the space allocated for the SVX detector. In each octant, the sense wires are strung tangent to the azimuthal direction in the plane perpendicular to the beam line. A sense wire plane is placed in each drift region of a module on either side of the high voltage grid. Charged particles passing through the VTX ionize the gas

and free electrons which drift along z toward the central cathode of each module and collected by sense wires. The drift times in conjunction with the radial positions of the sense wires are used to reconstruct an $r-z$ profile of the track. Thus, the VTX provides two dimensional track reconstruction, but it is primarily used to determine the z displacement of the primary vertex of the event by locating the convergence of all the reconstructed tracks in the event. The uncertainty in the measurement of the z coordinate of the vertex is in the range 1-2 mm, depending on the multiplicity of charged tracks associated with the reconstructed vertex. Each module is canted 15° in ϕ relative to its neighbors, therefore rudimentary ϕ information can be obtained for a track crossing through more than one module.

Central Tracking Chamber

The Central Tracking Chamber (CTC) [42] is the main tracking device of the CDF detector and performs full three dimensional reconstruction of the tracks of charged particles.

The CTC is a cylindrical drift chamber with an inner radius of 28 cm, outer radius of 138 cm, and length of 320 cm. It consists of 84 layers of 40 μm diameter gold plated tungsten sense wires arranged into nine superlayers. In five superlayers the wires are parallel to the beam line and are grouped in 12 sense wire layers. These five *axial* superlayers are interleaved with four superlayers of *stereo* wires, in which the sense wires tilted at $+3°$ or $-3°$ with respect to the beam direction. The stereo angle direction alternates at each stereo superlayer. Each stereo superlayer contains six sense wire layers. The axial layers provide tracking information in the $r-\phi$ plane while the stereo layers give information in the $r-z$ plane. Together, the axial and stereo layers measure the full helical path of charged particles traversing the chamber

and bending in the magnetic field, yielding momentum and charge measurement.

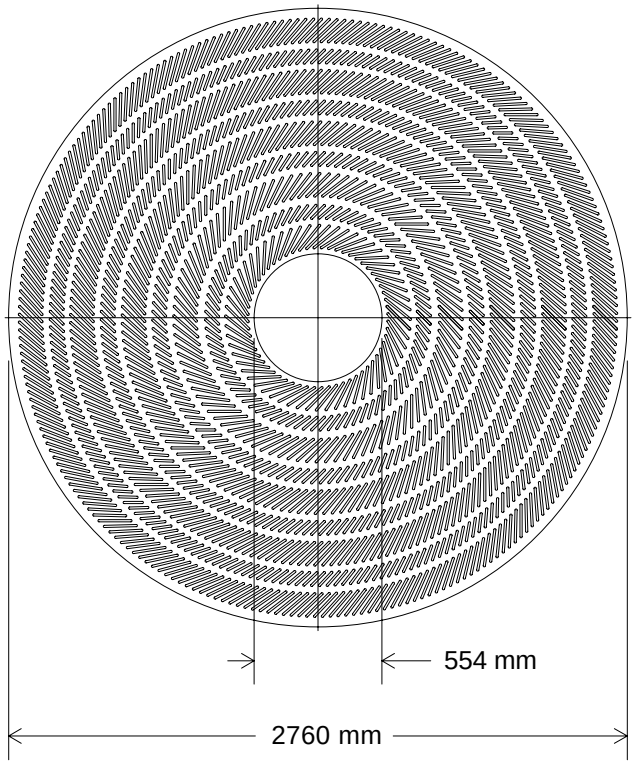

Figure 4.5: *End view of the Central Tracking Chamber.*

The superlayers are divided into cells so that the maximum drift distance is less than 40 mm, corresponding to a drift time of about 0.8 μs, much less than the 3.5 μs interval between bunch crossings. The boundaries of each cell are defined by two planes of stainless steel field wires, creating an electric field of 1350 V/cm. The sense wires lie midway between these planes with a potential wire separating each from its neighbor, which is used to control the gas gain on the sense wires. Figure 4.5 shows a transverse end view of the CTC. There are in total 6156 sense wires and $\approx$30000 field shaping wires. To compensate for the Lorenz angle produced by the crossed electric and magnetic fields the cells are tilted by 45° with respect to the radial direction. This gives drift electrons trajectories which are approximately

perpendicular to the radial direction and simplifies track reconstruction. There is a significant, about 20%, overlap in azimuth between the cells, which guarantees that every radial high P_T track must pass close to at least one sense wire in each superlayer.

Tracks are reconstructed by fitting hits in the CTC to a helix. The curvature of the track is related to the transverse momentum of the particle. The spatial resolution in the $r-\phi$ plane is between 125 and 250 μm, depending on the location in the chamber, and is 4 mm in the z direction. The two-track resolution of the CTC is 3.5 mm. The momentum resolution of the CTC is

$$\frac{\delta P_T}{P_T} = 0.002 \times P_T, \tag{4.3}$$

where P_T is measured in GeV/c. By combining tracking information from the CTC and the SVX, the momentum resolution improves to

$$\frac{\delta P_T}{P_T} = \big(0.0009 \times P_T\big) \oplus 0.0066. \tag{4.4}$$

The CTC is also able to determine the identity of particles by measuring the ionization rate along tracks.

Central Drift Tube Array

The Central Drift Tube (CDT) array [43] is the fourth tracking system and surrounds the CTC at a radius of 1.4 m. The CDT is composed of three layers of 672 3 m long, 1.27 cm diameter drift tubes oriented parallel to the beam pipe. A 50 μm diameter stainless steel anode wire is placed at the center of each drift tube. The CDT operates in the limited streamer mode, and provides accurate $r-\phi-z$ information. Tracking of charged particles in the $r-z$ view of the CDT array is accomplished via charge division along the anode wires. Drift-time measurements in three layers of the

CDT provide tracking information in the $r - \phi$ view. Typical resolutions are 2.5 mm in the axial (beam) direction and 200 μm in the azimuthal direction.

4.2.2 Calorimetry

The CDF calorimetry consists of three sections, the central, plug, and forward calorimeters, covering the pseudorapidity range $|\eta| < 4.2$ and providing full azimuthal coverage. The calorimeters are segmented in pseudorapidity and azimuth in a *projective tower geometry* which points toward the nominal interaction point. Each tower is composed of an electromagnetic section followed by a hadronic section to allow comparison of deposited electromagnetic and hadronic energy on a tower-by-tower basis. The coverage of the calorimeter towers in $\eta - \phi$ space is shown in Figure 4.6 for one CDF quadrant.

All CDF calorimeters are sampling calorimeters, which in contrast to homogeneous calorimeters sample only a fraction of the energy deposited by an incident particle. Layers of sampling material are interleaved with layers of absorber. A primary particle interacts with the absorber material producing a shower of secondary particles, which deposit a fraction of their energy in the active medium of the sampling layers. The true energy of the initial particle is determined by calibrating the calorimeter response to particles of known energy.

Two types of sampling calorimeters are used at CDF, employing scintillator or gas as active medium. Scintillator sampling was chosen for the central and endwall calorimeters because of its good energy resolution. In the forward region of the detector the energy resolution becomes less critical, although a finer transverse segmentation is needed to obtain the same spatial resolution as in the central region. To achieve this goal gas sampling was employed in the plug and forward calorimeters.

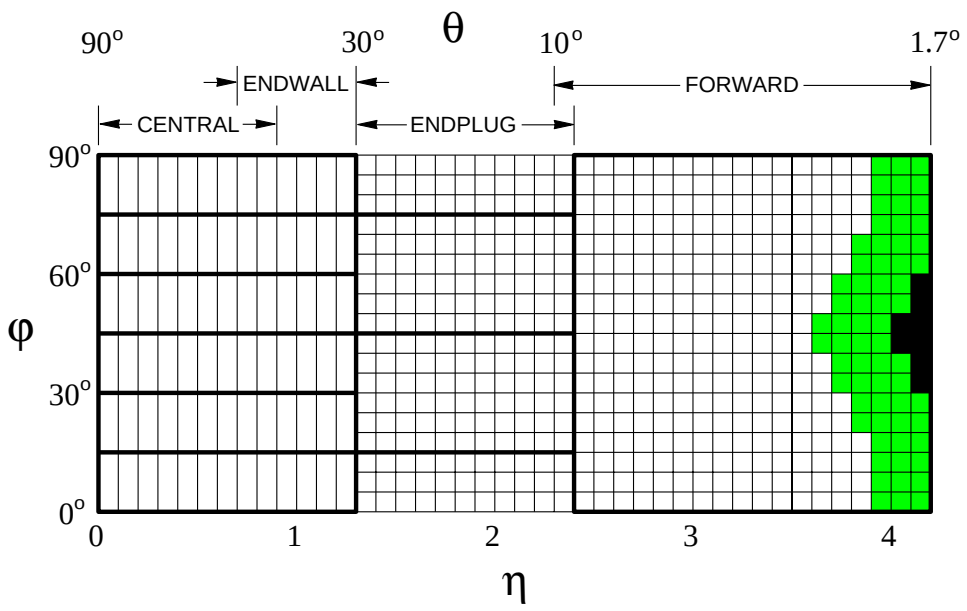

Figure 4.6: *Schematic $\eta - \phi$ segmentation of CDF hadronic calorimeters. The shaded region represents partial depth coverage to accommodate the low-β quadrupole magnets; the black region has no coverage. The heavy lines indicate module or chamber boundaries. The EM calorimeters have complete ϕ coverage out to $\eta = 4.2$.*

Central Calorimeters

The central calorimeter consists of 48 wedge-shaped modules, assembled into four free-standing "C"-shaped arches. Each module covers 15° in ϕ and consists of ten projective towers, with each covering approximately 0.1 units in η. The central electromagnetic calorimeter (CEM) [44] uses a hybrid design with scintillator/absorber sandwiches for energy measurement and an embedded strip chamber for position determination. This design combines the good energy resolution of scintillator with the high spatial resolution of gas strip chambers. A CEM tower is composed of thirty 3.2 mm thick lead layers, clad on each side with 0.38 mm of aluminum, interleaved with thirty-one 5 mm thick layers of polystyrene. The thickness of the CEM tower

is about 18 radiation lengths for electromagnetic showers, which corresponds to one interaction length for hadronic showers. In order to maintain a constant radiation length thickness as the polar angle varies, acrylic layers are substituted for lead layers, increasing the number of acrylic layers with increasing $|\eta|$. The light from the scintillator is collected by wavelength shifters, which are inserted in the gap between the steel cover and scintillator/absorber sandwiches, and transmitted by rectangular lightguides to photomultiplier tubes located at the back of each wedge. A cutaway cross-section view of a central calorimeter wedge is shown in Figure 4.7.

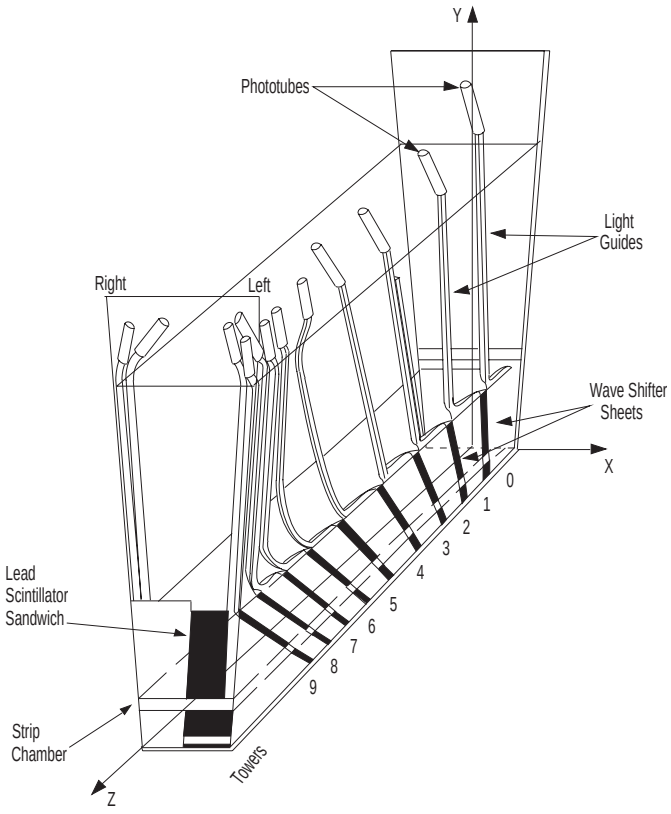

Figure 4.7: *Layout of the CEM light-collection system in a single wedge of the CEM and CHA calorimeters.*

The energy resolution for electrons between 10 and 100 GeV was measured

to be $\sigma/E = (13.5\%/\sqrt{E_T})\oplus 2\%$, where E_T is the transverse energy of the electrons in GeV and the symbol $\oplus$ indicates that the independent contributions are added in quadrature.

To enable a more precise measurement of the transverse profile of an electromagnetic shower, a proportional strip and wire chamber (CES) was embedded in the CEM wedges between the eighth lead layer and the ninth scintillator layer, at a depth corresponding to the maximum average transverse development of an electromagnetic shower. The CES is a proportional gas chamber with anode wires running along the beam direction and cathode strips along the ϕ direction, i.e. perpendicular to the wires. It is used to determine the shower position and the shower transverse development by measuring the charge deposition on the strips and wires. The position resolution of the CES is approximately 2 mm in azimuthal and z direction for 50 GeV electrons.

The CEM calorimeter is followed by the central (CHA) and endwall (WHA) hadronic calorimeters [45], which cover polar angles between 30° and 150° ($|\eta| < 1.3$). Each tower in the central electromagnetic calorimeter is matched by a hadronic tower. The CHA is constructed from 32 layers of 2.5 cm thick steel absorber interleaved with 1 cm thick layers of acrylic scintillator forming 4.7 interaction lengths. The WHA contains 15 layers of 5 cm thick steel plates perpendicular to the beam direction separated with 1 cm thick plates of acrylic scintillator (4.5 interaction length). The energy resolution of the CHA and the WHA for pions between 10 and 150 GeV was found to be $(50\%/\sqrt{E_T})\oplus 3\%$ and $(75\%/\sqrt{E_T})\oplus 4\%$ respectively.

The initial calibration of the central calorimeters was performed with 50 GeV electrons and pions in a test beam [46]. All modules were also tested with cosmic rays [47]. Maintaining of the initial calibration was provided by a calibration sys-

tem [48] employing radioactive and light sources. Gamma rays from individual ^{137}Cs sources on each module were used to maintain the scintillator gain calibration over long time periods. A ^{60}Co source automatically driven on a track was used to set the photomultiplier gain. For the CEM, short term variations were monitored by a xenon-flasher system that tested the response of the wavelength shifters. A light-emitting diode injected green light into the CEM phototubes via quartz fibers to check on short term variations and a nitrogen laser was used in a similar way for the hadronic phototubes. During Run 1B, source calibration runs were carried out about once a month and the flasher systems were used for daily calibrations.

Plug Calorimeters

The plug and forward calorimeters are gas calorimeters with a 50%/50% mixture of argon/ethane gas as active medium. The two plug calorimeters extend calorimetric coverage out to $|\eta| = 2.4$, and the forward calorimeters to $|\eta| = 4.2$. Each calorimeter consists of an electromagnetic and a hadronic section.

The Plug Electromagnetic Calorimeter (PEM) [49] is composed of four 90° azimuthal quadrants. Its projective towers cover 5° in ϕ, and there are sixteen towers segmented in η. The first tower, at $|\eta| = 2.4$, is of size $\Delta\eta = 0.09$, the next four towers are one half of this size, and the remaining eleven towers are of width 0.009 units of η. In the offline analysis, the four small towers are usually combined to form two standard towers. Each PEM quadrant consists of 34 layers of proportional drift tube arrays interleaved with 2.7 mm thick layers of lead. The proportional tubes are constructed of conductive plastic and have of a square inner cross section of 7 mm×7 mm with 0.8 mm thick walls. Each tube contains a centered 50 μm gold-plated tungsten anode wire. The tubes are arranged side by side in layers perpendicular to the beam

axis. The layers of tubes are sandwiched by a pair of 1.6 mm thick copper clad G-10 cathode panels. On one side of the panel, the copper is segmented into pads to provide projective tower geometry segmentation. On the other side of the G-10 panel the cathode signals from the pads are brought radially to the outer edge of the quadrant by etched strip lines. Summing up the pad signals longitudinally yields a single tower signal. Longitudinal segmentation is achieved by ganging the necessary number of connectors at the same ϕ into three depth segments. The first segment contains the first five layers, the second the next twenty four, and the third the last five. The front of the PEM is covered with a 1.3 cm thick steel plate, which acts as the first absorber layer. Similarly, the rear is covered with a 4.5 cm thick steel plate, acting as the first absorber layer of the hadronic calorimeter.

All towers of the PEM were calibrated with a 100 GeV electron beam. The energy resolution for electrons in the range 20 to 200 GeV was measured to be $\sigma/E = (28\%/\sqrt{E_T})\oplus 2\%$ and the response was found to be linear within 3%.

The Plug Hadronic Calorimeter (PHA) is arranged in twelve 30° sectors, and covers the region $1.2 < |\eta| < 2.4$. The PHA is a sandwich of 20 proportional tube layers alternating with 21 5.1 cm thick[1] steel plates. The PHA proportional tubes are similar to the PEM tubes. Gold-plated tungsten wires, centered in resistive plastic tubes with a cross section of 8 mm×14 mm, act as anodes. The cathode plane consists of 72 electrically distinct pads on the inner side, which are connected to the outer side via a plated through hole. Copper traces on the outer side carry the signals to the edge of the chamber. The signals from each chamber in the sector are ganged together longitudinally to form twelve towers, seventy-two towers per sector. The cathode tower signals are then amplified and digitized. The anode signal for each

[1]The plate after the fourth proportional layer has a thickness of 6.4 cm.

chamber is separately amplified and digitized, providing information on longitudinal shower development.

The PHA sectors were calibrated with charged 200 GeV pions. The observed response to pions between 20 and 200 GeV was linear and the energy resolution was measured to be $\sigma/E = (90\%/\sqrt{E_T})\oplus 4\%$.

Forward Calorimeters

The forward calorimeters complete the coverage of the CDF calorimeters, extending the range to $|\eta| = 4.2$. The two identical calorimeters are located 6.5 m from the interaction point in either z direction. The Forward Electromagnetic Calorimeter (FEM) is azimuthally arranged in four 90° quadrants. The FEM is a sandwich of 30 layers of gas-filled proportional chambers interleaved with lead plates, segmented into projective towers in ϕ and η. A FEM tower spans 5° in ϕ, and there are nineteen towers of 0.1 units of η. Pad signals are read out in two equal longitudinal depth segments. The anode wires are ganged together in five sectors per chamber.

Four quadrants of FEM were calibrated with electrons. The energy response was found to be linear for electrons in the energy range from 20 to 160 GeV and the energy resolution was measured to be $\sigma/E = (25\%/\sqrt{E_T})\oplus 2\%$.

The FEM towers are followed by the towers of the Forward Hadronic Calorimeter (FHA) [52]. Each FHA segment is composed of alternated 27 steel plates and 27 layers of proportional chambers. The construction of the proportional chambers is similar to that of the FEM, but the tubes are about 1.5 times larger and there is no longitudinal segmentation. The signals from the anode wires, segmented into six sections per chamber, are used for monitoring the longitudinal shower development.

The FHA was calibrated with charged pion beams. The calorimeter response

was found to be linear for pions from 40 to 200 GeV and the energy resolution was measured to be $\sigma/E = (130\%/\sqrt{E_T})\oplus 4\%$.

The gas gain of the proportional chambers in the plug and forward calorimeters was monitored, to better than 1%, via a number of special gas monitor drift tubes. The monitoring tubes were irradiated by 5.9 KeV gamma rays from ^{55}Fe sources affixed to the tubes.

4.2.3 Muon Detectors

The central muon system consists of three detectors, the Central Muon detector (CMU) [53], the central Muon Upgrade (CMP) and the Central Muon Extension (CMX). The CMU and CMP cover the pseudorapidity range $|\eta| < 0.6$ and the CMX, $0.6 < |\eta| < 1.0$. All these detectors consist of proportional drift chambers. A 50%/50% mixture of argon/ethane gas is used in all the chambers, bubbled through either ethanol or isopropanol at -7°C acting as the quenching agent.

Central Muon Chamber

The CMU is located directly behind the CHA at a distance of 3.47 m from the beam axis. There are about five interaction lengths of material between the CMU and the beam axis. Muons of $P_T > 1.5$ GeV/c have sufficient momentum to pass through the calorimeters and enter the CMU.

The CMU is segmented in ϕ into 12.6° wedges, each of which is further segmented into three modules of 4.2° each. Each module in a wedge is made up of four layers of four rectangular cells. A stainless steel resistive sense wire 50 μm in diameter is located at the center of the cell. Four drift cells, one from each layer, form a *muon tower*. Two of the four sense wires, from alternating layers, lie on a radial

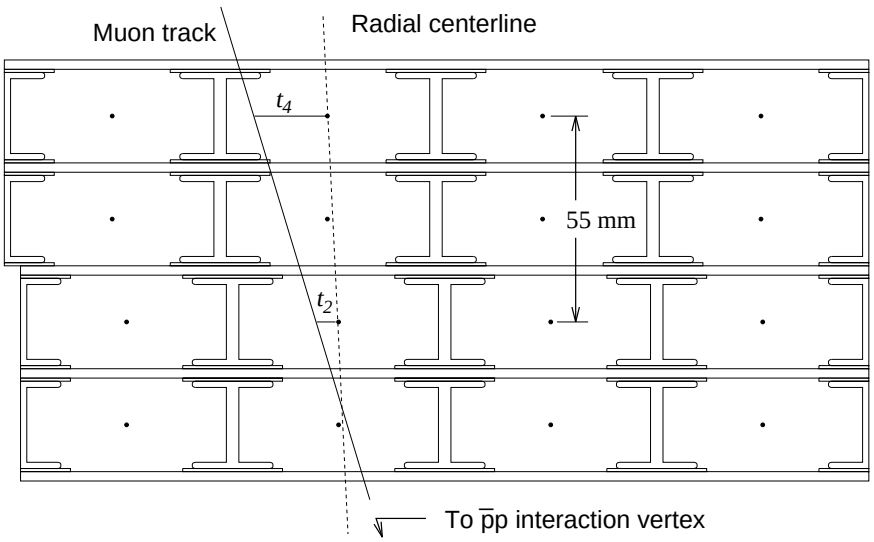

Figure 4.8: *One module of the CMU showing the arrangement of the four planes of drift tubes in a view along the beam direction. Alternating layers' sense wires have a 2 mm offset in their azimuthal position. A particle traversing through one muon tower and the associated drift times are also shown.*

line passing through the interaction point. The remaining two wires are offset from these by 2 mm in the midpoint of the chamber to resolve the ambiguity as to which side of the sense wires in ϕ a track passes by measuring the difference in arrival times of the drift electrons. The CMU has 84% coverage in ϕ due to 2.4° gaps between adjacent wedges and the gap between the two calorimeter arches at $\eta = 0$. Tracks in the CMU are reconstructed with a resolution of 250 μm in the $r - \phi$ plane and z resolution 1.2 mm [53]. The CMU also provides a rough measurement of transverse momentum for muon tracks from the track azimuthal angle with respect to the sense wires, obtained from timing differences between alternating layers. A reconstructed muon track in the drift chambers is often referred to as a *muon stub*. If this stub matches a CTC track, the track is considered to be a muon candidate.

Central Muon Upgrade

The Central Muon Upgrade system [54] is located outside the CMU behind an additional three interaction lengths of steel for extra hadron absorption. Behind shielding there are four layers of drift tubes of similar construction to those in the CMU. The CMP system provides 63% azimuthal coverage. The extra shielding drastically reduces the hadronic background in this chamber relative to that in the CMU but also raises the transverse momentum threshold for detectable muons to 2.2 GeV/c. The CMP measures the muon position in the $r-\phi$ plane with a resolution of 300 μm.

Central Muon Extension

Muon detection was extended to the $0.6 < |\eta| < 1.0$ region with the addition of four free standing conical arches of four layers of drift tubes called the Central Muon Extension (CMX). Figure 4.3 shows the placement of these arches around the central detector. The CMX coverage is $\sim$ 66% in azimuth. In order to reach the CMX chambers a particle has to go through six interaction lengths of material and have transverse momentum higher than 1.7 GeV/c. The CMX is sandwiched between two layers of scintillator counters (CSX) [55] which are used for triggering. The CMX drift tubes are of a similar construction to the CMU and CMP drift tubes. The position resolution in azimuth obtained with the CMX is about 270 μm.

Forward Muon Detector

The Forward Muon system (FMU) [56] consists of a pair of magnetized iron toroids with three sets of gas drift chambers and two planes of scintillation trigger counters. The FMU covers the pseudorapidity range $2.0 < |\eta| < 3.6$. The drift chambers provide a measurement of muon momentum with resolution 13% and

position with resolution 130 μm.

4.2.4 Beam-Beam Counters

The beam-beam counters (BBC) are two planes of scintillation counters mounted in the front of the forward calorimeter on the east and west sides of the detector. These scintillator hodoscopes are primarily used to provide a *minimum bias trigger* [57] for the detector, and are also used to estimate the luminosity. Each BBC consists of sixteen scintillator counters arranged in a criss-cross grid around the beam pipe, forming four concentric squares, as shown in Figure 4.9. The dimensions of the four counters in each square are such that each counter covers an approximately equal range in pseudorapidity of $\Delta\eta = 0.7$. The counters are located at a distance of 5.8 m from the nominal interaction point and cover the angular region from 0.32° to 4.47°, corresponding to a pseudo-rapidity of range of 3.24 to 5.89. The counters provide an accurate measurement of the time of the interaction with a timing resolution better than 200 ps. Coincident signals detected in the counters on each side of the interaction point, within a fifteen nanosecond gate centered twenty nanoseconds after the beam crossing, serve as a minimum bias trigger. The minimum bias trigger rejects events due to collisions between the beam and residual gas in the beam pipe, beam halo, and cosmic rays.

The integrated (instantaneous) luminosity is measured as the rate of east-west coincidences divided by σ_{BBC}, the $\bar{p}p$ cross section visible in the beam-beam counters. The measured value of σ_{BBC} is 51.15 ± 1.60 mb [58].

The beam-beam counters play an important role in the analysis of this dissertation, measuring the charged particle multiplicity in the forward region. Together with the adjacent forward calorimeter they are used to tag events with a forward ra-

pidity gap.

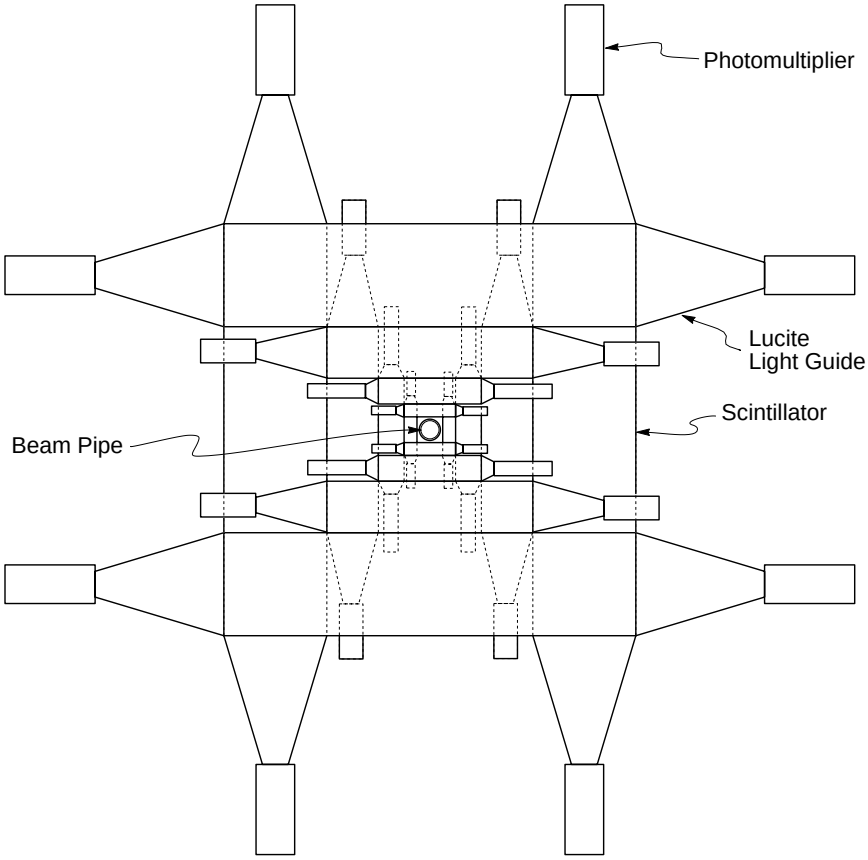

Figure 4.9: *Front view of one of the Beam-Beam Counter planes.*

4.3 Trigger System

At the Tevatron, operating with six proton bunches colliding with six anti-proton bunches, a beam crossing at the CDF detector occurs every 3.5 μs. Therefore, with a typical instantaneous luminosity of $\mathcal{L} \approx 10^{31}$ cm^{-2}s^{-1} at least one $\bar{p}p$ interaction is expected at every beam crossing, yielding an event rate of $\sim$ 300 KHz. The amount of information the CDF detector collects after a single beam crossing, termed an *event* as far as the data and triggering system are concerned, is typically around 200 KB.

CDF can reliably write data to permanent storage media at a maximum rate of a few events per second, thus keeping the amount of data for offline processing to a manageable level. This requires the use of a sophisticated trigger system with a rejection factor of about 10^4-10^5, while maintaining high trigger efficiencies for desired types of events.

In order to select and filter the small fraction of interesting physics events from the large number of $p\bar{p}$ interactions produced by the Tevatron, CDF implements a three-level trigger system [57]. Each successive level uses more detailed requirements. The decision at each level is based on a logical "OR" of these requirements, which are designed to select different physics processes. The first two levels of the trigger system are implemented in hardware, while the third level is implemented in software.

The first level trigger, Level 1, trigger makes a decision whether or not to accept the event in the relatively short time between beam crossing (3.5 μs), introducing no *dead-time*(time interval when the trigger system cannot react to a beam crossing). Level 1 is implemented in custom-built hardware and uses the fast analog outputs from the calorimeters and muon detectors. The calorimeter towers are summed, separately for the electromagnetic and hadronic parts, into *trigger towers* of 0.2 units in η and 15° in ϕ, corresponding to an array of 42 (in η) by 24 (in ϕ). The signals from the towers are summed and weighted by $\sin\theta$ to represent the transverse energy, E_T.

Typical Level 1 trigger requirements are that the transverse energy of a single trigger tower be above some preprogrammed threshold, or the presence of track segments in the muon chambers, or a beam-beam counter coincidence, etc. Various combinations of the above criteria form different Level 1 triggers. The average rate of accepted events out of Level 1 is approximately 1 KHz.

Once Level 1 trigger accepts an event, the second level trigger, Level 2, deals with the event. If the event is rejected, the information stored in the CDF components is cleared and the detector is ready to consider the next $p\bar{p}$ interaction. The Level 2 trigger takes about 20 μs to decide if the event should be considered further or not, introducing $\sim 10\%$ of dead-time.

Level 2 uses the same 42×24 array of trigger towers in $\eta - \phi$ to search for clusters of electromagnetic or total energy. This is done by a hardware *cluster finder*. The clusters are formed by searching for a seed tower above some predefined threshold and adding in neighboring towers which are over a lower threshold. Electromagnetic and hadronic energies of all found clusters are summed separately, digitized and presented to a fast hardware Level 2 processor. Electromagnetic clusters are distinguished from hadronic jet clusters on the basis of the fraction of the electromagnetic energy in the cluster. For each calorimeter cluster and track segment in the muon chambers, the fast hardware tracking processor matches tracks found in the CTC. The result of the Level 2 trigger processing is identification of possible muon, electron, photon, and jet candidates. The acceptance rate after the Level 2 trigger is ~ 20 Hz.

At Level 2 some triggers are prescaled to reduce the total acceptance rate. This means that a predefined fraction of events that passed the trigger are considered to fail it. Prescaling is sometimes more preferable to making the trigger cuts more stringent and allows to accept as many rate events as possible while still accepting other data at reasonable rates. Some triggers are *dynamically* prescaled. A dynamical prescale changes during the course of the run depending on the instantaneous luminosity: it is large when the luminosity is high and small when the luminosity is low.

The Level 3 trigger, which is the last stage of the on-line trigger system, is entirely based on software. It runs a simplified version of the CDF offline event reconstruction code on a farm of 64 commercial Silicon Graphics processors. Several events are analyzed in parallel. After the event reconstruction, various analysis and filtering software modules are run in separate trigger paths. The Level 3 trigger reduces the event rate to a few Hz with a rejection factor of 3-4. All events passing Level 3 were logged to staging disks and then copied to 8 mm tapes.

4.4 Data Acquisition System

The CDF detector has about 150,000 electronic channels of photomultiplier tubes, strip/wire/pad chambers, drift chambers, drift chambers with current division readout, and silicon strip detectors. These channels are read out by *front end* electronics, which consists of 60 commercial FASTBUS crates and 129 custom built RABBIT crates mounted on the detector.

A special Redundant Analog Bus-Based Information Transfer (RABBIT) [59] system was developed at Fermilab to deal with the very large dynamic range, $\sim (0.001 - 100)$ GeV, required by the calorimetry electronic readout. Most tracking detectors are read out by a FASTBUS [59] system. The RABBIT system services calorimetry and muon detectors. The analog signals from the front end electronics are digitized by analog-to-digital (ADC) or time-to-digital (TDC) converters, depending on the origin of the signal. The digitized RABBIT channels are read out by fast intelligent scanners called MXs [59]. FASTBUS Readout controllers (FRC) are installed in each FASTBUS crate to read out the front end electronics. A series of six single-board VME based Scanner CPUs (SCPU) read out a subset of the FRCs over

a custom built Scanner Bus. The Scanner CPUs are controlled by processes running on a dedicated VME based CPU called the Scanner Manager (SM). FRCs also provide the interface for the MX readout. The data flow through the hardware trigger system, consisting of the Level 1 and 2 triggers and Front-end Readout and Decision boards (FRED), is managed by the Trigger Supervisor (TS) FASTBUS module.

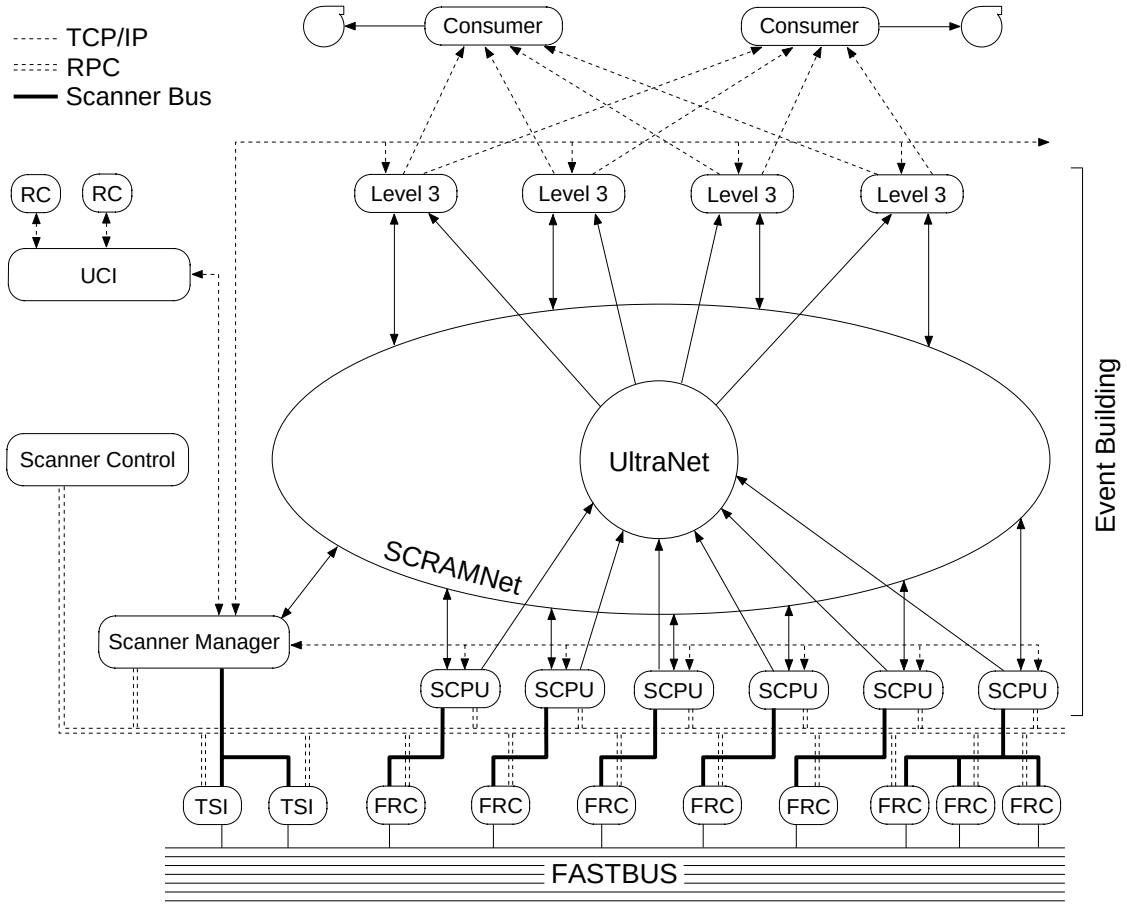

Figure 4.10: *Schematic of data flow through the CDF Data Acquisition system.*

During data taking, once the Level 2 trigger accepts an event, it communicates its decision via FRED to the Trigger Supervisor, which instructs the FRCs to load the event. When all FRCs finish loading an event, the Trigger Supervisor notifies the Scanner Manager about the event, via the Trigger Supervisor Interface

(TSI), which is an FRC in the Trigger Supervisor crate. After that the SM broadcasts the "Load Event" control signal to the SCPU. Communication with the Scanner CPUs, Scanner Manager and the Level 3 systems is via a dedicated reflective-memory network called SCRAMNet (Shared Common RAM Network). After a SCPU has received data from all FRCs connected to it, it sends the "Load Event" acknowledgment to the SM. After all the SCPUs are finished loading the event, the SM informs the Trigger Supervisor via TSI, which frees the front end buffers so that another event can be loaded. Additionally, the SM finds an available memory buffer in Level 3, and issues a "Send Event" command to the SCPU. Each SCPU transmits its event fragment over the Ultranet network to the correct Level 3 memory buffer. After the transmission is finished, the SCPU returns a "Send Event" acknowledgment to the SM. The SM notifies the Level 3 when the event is complete. The Level 3 builds and formats the complete event from the received fragments and passes it to Level 3 trigger software. Events passing the Level 3 trigger are passed to the Consumer Server (CS) via Ultranet. The CS then passes events to the Consumers using either Ultranet or Ethernet. One of the consumers is the Data Logger, which writes accepted events to staging disks and subsequently to tape. The SM crate contains the User Control Interface (UCI) and the Error Monitor processes, running on local CPU VME boards. Thus a command passing from the DAQ user via Run Control (RC) to and from the SM, which controls the entire system, is implemented via yet another independent path, the VME bus of the SM crate.

Chapter 5

Data

The events used in the analysis of this dissertation were selected by a three level trigger system, described in Section 4.3. The criteria used to identify muon triggers are described in more detail in the following section.

5.1 Muon Triggers

Muon candidates from the decay $J/\psi \to \mu^+\mu^-$ are identified in the central pseudorapidity region ($|\eta| < 1.0$) by the muon drift chambers described in Section 4.2.3. The central muon chambers, CMU and CMP, cover the region $|\eta| < 0.6$, and the central muon extension system, CMX, extends this coverage to $|\eta| < 1.0$. These muon detectors are used in a three-level trigger system to require one or two muons in the event.

5.1.1 Level 1

For the Level 1 trigger the central muon detectors are logically segmented in azimuth into 5° wide trigger towers. The east and west halves of the detectors are

independent. Also, the CMU and CMX trigger towers are counted separately. A muon track or stub at the trigger level consists of at least two hits on radially aligned wires in the CMU or CMX chambers. To reduce backgrounds each muon stub is required to have a matching hit from the hadron-calorimeter TDC fastout. In addition, for CMX stubs the trigger uses the timing information provided by scintillator counters (CSX), in order to reduce the rate from particles not associated with the primary interaction. The transverse momentum, P_T, of the muon track segment is roughly evaluated by using the arrival times of the drift electrons at the sense wires to determine the deflection angle due to the magnetic field. The Level 1 dimuon trigger requires two muon stubs with $P_T > 3.3$ GeV/c. Despite the P_T cut, a muon with a P_T as low as 1.5 GeV/c can pass the dimuon triggers. The trigger hardware combines azimuthally adjacent towers with muon stubs into a single muon. Thus, to pass the dimuon trigger, there must be a tower between two muons which does not contain a muon stub, or the muons must be in opposite halves of the detector or in different muon systems (CMU and CMX). The Level 1 single muon trigger requires a track segment in the CMU system with $P_T > 6$ GeV/c in coincidence with hits in the CMP, or a track segment in the CMX with $P_T > 10$ GeV/c in coincidence with hits in the CSX.

5.1.2 Level 2

To identify muons the Level 2 muon trigger matches CTC tracks reconstructed in the $r - \phi$ plane using the Central Fast Track processor (CFT) [60], above a specific P_T threshold to muon trigger towers which are set at Level 1. The momentum resolution of the CFT is $\sigma(P_T)/P_T = 3.5\%$ with high efficiency. If the CFT track extrapolates to a muon trigger tower, the wedge containing this tower and the trigger tower itself are marked as having a golden muon. Golden muons are associated with

calorimeter trigger towers defined in Section 4.3. Contiguous calorimeter towers are grouped by the hardware cluster finder to form Level 2 *muon clusters*. Clusters are tagged as to whether they are for CMU and/or CMX muons. A typical muon cluster includes 3 calorimeter towers; however, golden muon hits in adjacent wedges form a 6-tower cluster, and a single CFT track associated with CMU and CMX Level 1 trigger towers on the same side in the same wedge yields a 5-tower cluster. Each such cluster is treated as one gold muon by Level 2. The Level 2 dimuon trigger demands a Level 1 dimuon trigger and one or two Level 2 muon clusters as described above. The trigger with two golden muons requires associated CFT tracks of $P_T > 2.2$ GeV/c. For two CMU/CMX muon candidates on the same side of the detector the trigger also requires at least one empty wedge between the two golden wedges. For a CMU muon candidate pair with one muon in the east and the other in the west half of the detector, the golden wedges must be at different azimuth for the trigger to fire. The Level 2 dimuon trigger requiring one Level 2 CMU cluster and in addition demands a second Level 1 muon stub in either the CMU or the CMX, or the highest P_T muon cluster to have 6 or more towers. In the first case the threshold of matching a CFT track is set at 3.4 GeV/c and in the second case at 2.2 GeV/c. The Level 2 single muon trigger requires a Level 1 single muon trigger and one Level 2 muon cluster with a CFT track of $P_T > 7.5$ GeV/c or $P_T > 12$ GeV/c. The extrapolated position of the CFT track to the muon tower is required to be within 5° in azimuth. In addition, depending on further use, several single muon triggers apply jet requirements or a minimum ionizing cut.

5.1.3 Level 3

At the third level of the trigger, a computer farm is used to fully reconstruct the data, including three-dimensional track reconstruction in the CTC in addition to the standard muon reconstruction. There are two Level 3 triggers used to select J/ψ candidates. The first trigger requires a Level 2 trigger with two golden muons and applies a set of quality cuts detailed below, while the second requires an event to only pass any other Level 2 muon trigger. In addition to the requirement of two Level 2 muons, the first Level 3 trigger applies the following selection criteria:

- a pair of oppositely charged muons;
- muon track transverse momentum of $P_T > 1.4$ GeV/c;
- dimuon invariant mass between 2.8 and 3.4 GeV/c^2;
- matching between the extrapolated CTC track and the muon stub within 4σ in the $r-\phi$ and $r-z$ view for CMU muons, and in the $r-\phi$ view only for CMX and CMP muons, where σ is the track extrapolation uncertainty due to multiple scattering and resolution.

The triggers are necessary to ensure that the events are in a region where the efficiency of the detector is well understood. Additional requirements are applied for the purpose of increasing the signal to background ratio. The backgrounds that need to be suppressed are discussed below.

5.2 Non-J/ψ Background Contributions

The main source of muon background is *punch-through*, which is usually divided into two types. Non-interactive (or *sail-through*) punch-through takes place

when a charged hadron, typically a pion or a kaon, travels through the entire calorimeter without initiating a hadronic shower. Averaged over the different particles, there is a 0.5% probability of a hadron penetrating the calorimeters without initiating a shower [61, 62]. Since this is the specific property of muons which the muon detectors exploit to identify muons, these particles are misidentified as muons. There is little that can be done to reject this type of background, beyond increasing the shielding in front of the muon chambers. Interactive punch-through occurs when a particle initiates a shower in the calorimeter, but the shower is not fully contained by the hadronic calorimeter and one or more charged particles escape. If one of these particles leaves a stub in the muon chamber consistent with a track reconstructed in the CTC, a muon candidate is formed. Since these particles are generally traveling at an angle relative to the particle that initiated the shower, the match of the muon stub with the extrapolated CTC track is often much worse than for a real muon.

Another source of background is *decay-in-flight* muons. These are muons produced by the decays $(\pi^{\pm}, K^{\pm}) \rightarrow \mu^{\pm}\nu_{\mu}$. Depending on where in the detector the decay occurs, it will either result in a poorer match between the muon stub and the extrapolated CTC track or there may be difficulties in attempting to extrapolate the track to the production vertex. The magnitude of any extrapolation discrepancies will depend upon the parent transverse momentum; higher P_T decays will produce smaller kinks and smaller discrepancies.

Background is also contributed by heavy flavor decays, consisting of opposite sign muon pairs produced by $b\bar{b}$ or $c\bar{c}$ production when both heavy quarks decay semileptonically by $b\bar{b} \rightarrow c\bar{c}\mu^{+}\mu^{-}X$ or $c\bar{c} \rightarrow s\bar{s}\mu^{+}\mu^{-}X$ or by the sequential decay $b \rightarrow c\mu^{-}\bar{\nu_{\mu}}$ followed by $c \rightarrow s\mu^{+}\nu_{\mu}$. Whereas most of the other backgrounds do not contain muons, the muon candidates produced by these decays are real muons. The

only differences with J/ψ events are that the mass does not peak sharply and the muons do not originate from a common vertex.

Still another background is dimuons from Drell-Yan production. Unlike the heavy flavor decay background, these dimuons are produced from the same vertex. The Drell-Yan dimuons form an invariant mass which contributes to the background under the J/ψ mass peak.

5.3 Offline Dimuon Selection

The sample of J/ψ candidates selected by the Level 3 trigger is further processed in the offline analysis by applying the following set of selection criteria.

- All runs declared "bad" for analysis based on the muon detectors or containing duplicate events are removed from the sample.

- As explained in Section 6.2 we use BBC information to tag rapidity gaps. Therefore, we only use data for which there is no BBC-coincidence requirement in the trigger.

- In diffractive J/ψ events, a second minimum bias interaction most likely contributes to non-zero multiplicity on the rapidity gap side of the event. In order to eliminate events with more than one interaction during the same beam-beam crossing, only events with one reconstructed vertex are retained.

- The vertex distribution has a roughly Gaussian shape of 30 cm width and is centered within a few cm around $z = 0$. To ensure good coverage by the central detector, each event is required to have a vertex within ± 60 cm of the center of the detector along the beam line.

- A minimum transverse momentum of 2 GeV/c is required for each muon to ensure that the muon trigger was efficient for dimuon events.

- Several of the backgrounds mentioned above create muon candidates for which the matching between the muon stub and the CTC track is not as good as in the case of muons from J/ψ decays. To reduce these backgrounds, the matching requirement is tightened to be less than 3σ in the $r-\phi$ view and less than $\sqrt{12}\sigma$ in the $r-z$ view: $\chi^2_{r-\phi}$(CMU)$<$ 9, χ^2_{r-z}(CMU)$<$ 12, $\chi^2_{r-\phi}$(CMP)$<$ 9, $\chi^2_{r-\phi}$(CMX)$<$ 9.

- For optimal vertex resolution both muon candidate tracks are required to be reconstructed in the SVX detector.

- The muon tracks are constrained to come from a common vertex. The χ^2 from the vertex constrained fit (CTVMFT) is required to be less than 6.6, which corresponds to a confidence level for the fit larger than 1%. There are several advantages in imposing this constraint. The calculated dimuon mass using the vertex constrained momenta is more accurate than the unconstrained mass, resulting in less background under the mass peak. Also, some of the background sources yield tracks which do not extrapolate to a common vertex. Requiring the two tracks to be consistent with a common vertex reduces these backgrounds.

- The calculated uncertainty of the two dimensional decay distance L_{xy} [1] is re-

[1] L_{xy} is the projection of the vector $\vec{X}$, pointing from the primary to the secondary vertex, onto the transverse momentum of the J/ψ:

$$L_{xy} \equiv \frac{\vec{X} \cdot \vec{P_T}^{\psi}}{|\vec{P_T}^{\psi}|}$$

quired to be $\leq 150\ \mu m$ to ensure a precise vertex measurement.

- The dimuon invariant mass of J/ψ candidates is required to be in the window $3.05 \leq M_{\mu^+\mu^-} < 3.15\ \mathrm{GeV}/c^2$.

The mass window requirement is presented for reference only. It is relaxed in order to estimate the non-J/ψ background under the J/ψ peak (see Section 6.4) and to study the contribution from B-hadron decays presented in Section 6.9.

Criterion	Accepted Events
Initial sample	990,422
Bad runs and duplicate events	835,236
No BBC coincidence in the trigger	734,375
Only 1 vertex	74,058
$\lvert z_{\mathrm{vertex}}\rvert \leq 60$ cm	70,149
$P_T^{\mu} \geq 2\ \mathrm{GeV}/c$	52,343
$\chi^2_{r-\phi}$(CMU/CMP/CMX)< 9, χ^2_{r-z}(CMX)< 12	48,396
Both muon tracks in the SVX	31,551
Vertex constrained fit $\chi^2 \leq 6.6$	28,669
$\sigma(L_{xy}) \leq 150\ \mu m$	26,115
$3.05 \leq M_{\mu^+\mu^-} < 3.15\ \mathrm{GeV}/c^2$	18,910

Table 5.1: *Criteria used to select the $J/\psi \to \mu^+\mu^-$ sample for the diffractive analysis.*

Table 5.1 lists the offline selection criteria together with the number of events remaining in the sample after each cut. Figure 5.1 shows the distribution of the primary vertex z-position (a), the χ^2 of the vertex constrained fit (b), the muon transverse momentum (c) and the calculated decay length uncertainty (d) for the events remaining in the sample and those removed (shaded area) by the corresponding selection criterion. The final J/ψ sample contains 18,910 events.

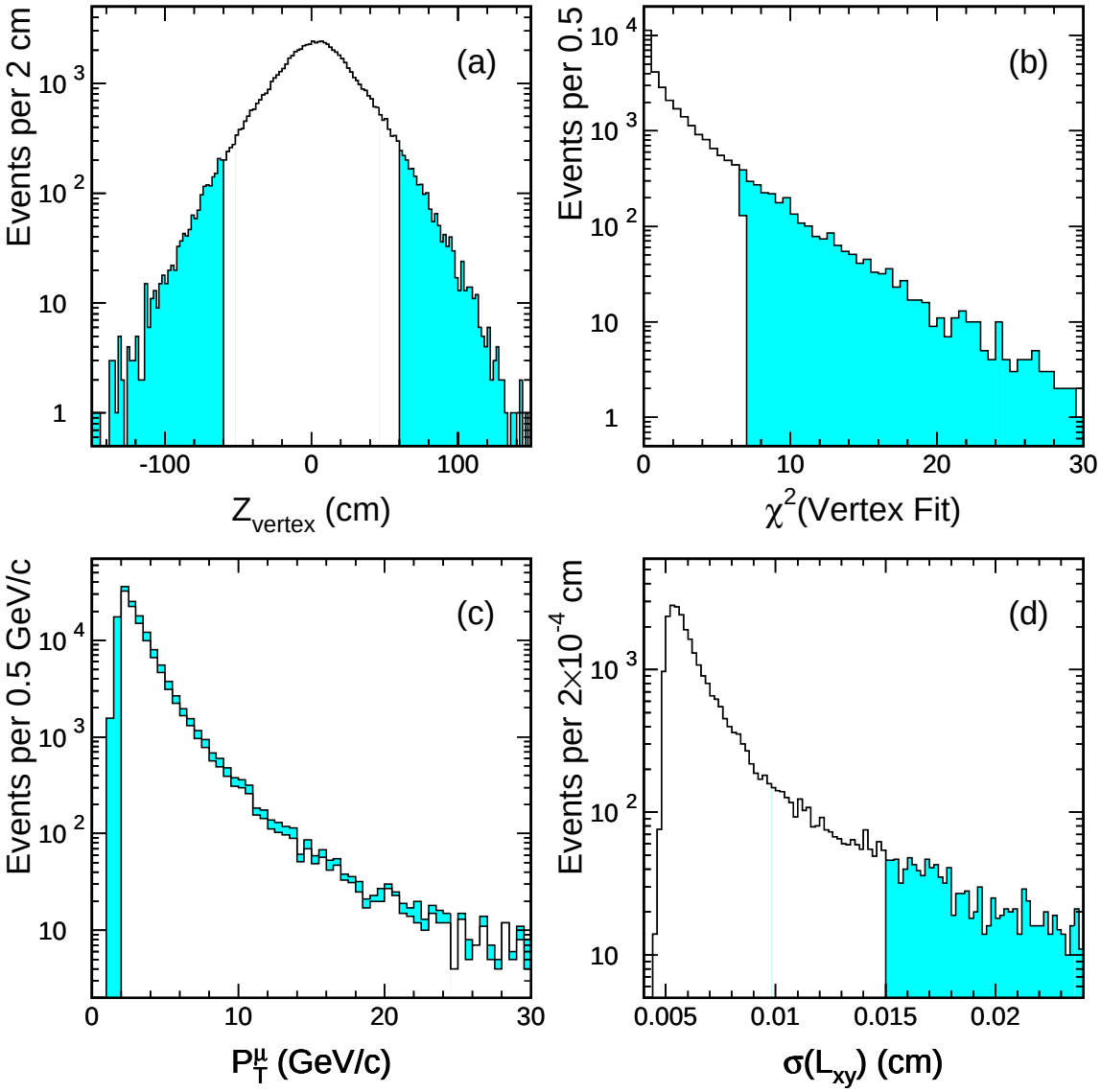

Figure 5.1: *(a) Primary vertex z-position, (b) χ^2 of the vertex constrained fit, (c) muon transverse momentum and (d) calculated decay length uncertainty for the events remaining in the sample (histogram) and those removed (shaded area) by the selection criterion.*

Chapter 6

Diffractive J/ψ Production

6.1 Introduction

CDF has published several papers on hard diffraction, diffractive W [23], dijet [21] and bottom-quark production [1]. The interest in these processes lies in the information they provide about the quark and gluon content of the colorless exchange, the so-called pomeron, which mediates diffractive reactions. In hadron-hadron collisions J/ψ mesons are mainly produced through gg fusion reactions (See Fig. 6.1) and therefore diffractive J/ψ production enables us to probe directly the gluon content in the pomeron [63].

Sections 6.2 - 6.6 describe the method of extracting the diffractive J/ψ signal. The corrections used to calculate the fraction of diffractive J/ψ production are discussed in Section 6.7. The diffractive to non-diffractive J/ψ production ratio is given in Section 6.8, and an extensive study on separation of prompt and non-prompt J/ψ components is provided in Section 6.9.

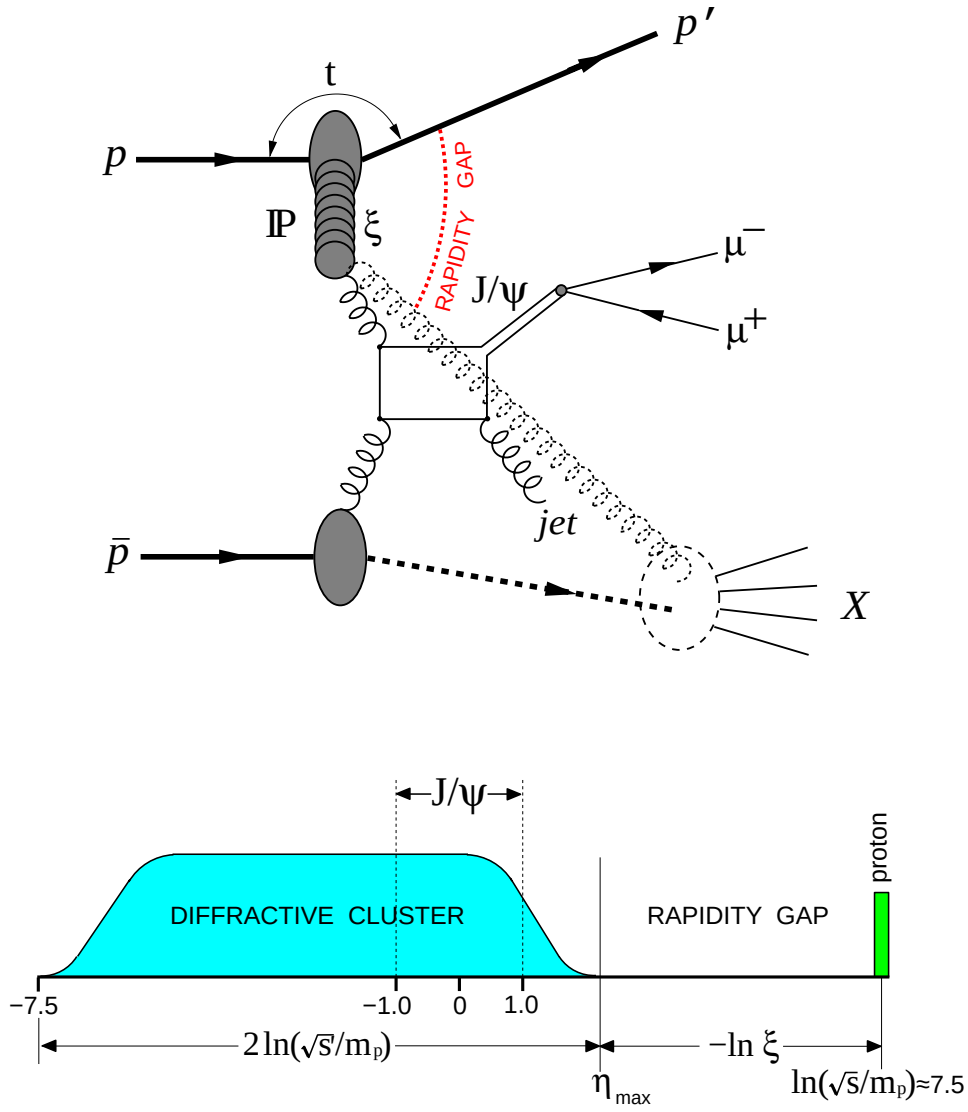

Figure 6.1: *Schematic diagram for diffractive J/ψ production by color-singlet exchange in $\bar{p}p$ interactions.*

6.2 Rapidity Gaps

Single-diffractive (SD) events are characterized by a rapidity gap (absence of particles) in one of the forward regions of the detector. The interpretation of such events in terms of pomeron exchange is illustrated in Figure 6.1. Suppose an incoming proton emits a pomeron that interacts with an incoming antiproton. Since the pomeron is a colorless object with vacuum quantum numbers, no particles are produced in the rapidity region between the proton and the pomeron, and a rapidity gap appears on the east side of the detector (at CDF protons travel from west to east). The width of this gap is $\Delta\eta \approx -\ln\xi$, where ξ is the fraction of the proton momentum carried by the pomeron. The far edge of the gap is given by the outgoing proton rapidity, which is $\eta_{\rm proton} = \ln(\sqrt{s}/m_{\rm proton}) \approx 7.5$ [1].

When searching for rapidity gaps, two effects must be taken into account: detector noise, which fills true rapidity gaps with fake particle signals, and multiplicity fluctuations, which create rapidity gaps of non-diffractive origin. To deal with the detector noise problem, the standard technique at CDF is to set calorimeter thresholds just above noise level and to correlate calorimeter gaps with gaps in the beam-beam counters. Optimal calorimeter thresholds were determined by studying a sample of events triggered on beam-beam crossings only and with no reconstructed vertex [64]. These thresholds are listed in Table 6.1.

For this analysis rapidity gaps are identified by the following two requirements:

1. No calorimeter tower energy above threshold in the region $-4.2 \leq \eta \leq -2.4$ for west gaps, or $2.4 \leq \eta \leq 4.2$ for east gaps.

[1] We use rapidity y and pseudo-rapidity η interchangeably, since in practice they are approximately equal.

η region	Tower E_T threshold (GeV)
$\lvert\eta\rvert < 1.1$	0.2
$1.1 < \lvert\eta\rvert < 1.5$	$0.45 \times \sin[2\arctan(\exp(-\eta))]$
$1.5 < \lvert\eta\rvert < 2.3$	0.2
$2.3 < \lvert\eta\rvert < 3.0$	$-0.143 \times \lvert\eta\rvert + 0.579$
$3.0 < \lvert\eta\rvert < 4.2$	$-0.0625 \times \lvert\eta\rvert + 0.3375$

Table 6.1: *Tower E_T thresholds used to tag rapidity gaps in the calorimeters. In the central and plug calorimeters the thresholds are constant at 200 MeV except around edge cells. In the forward calorimeters the E_T thresholds are approximately equivalent to a constant energy threshold of 1.5 GeV.*

2. No hit in the beam-beam counters (BBC) on the same side as the calorimeter gap. Here, a beam-beam counter hit is defined as the logical AND of the hit signals of the two attached PMT's. A PMT is hit if the corresponding TDC count is less than 100 nsec. The logical AND is satisfied if the difference between the two PMT TDC's is less than 15 nsec. The rapidity coverage of the beam-beam counters extends from 3.2 to 5.9 on each side of the detector.

A typical diffractive J/ψ candidate is shown in Figure 6.2. As shown in the top lego plot, there is no calorimeter activity in the region $2.4 \leq \eta \leq 4.2$. In addition to the two muons from the J/ψ decay there is a jet produced back-to-back in ϕ with respect to the J/ψ.

6.3 Diffractive Event Signal

To select rapidity gap events we plot the BBC hit multiplicity versus the multiplicity of the forward calorimeter towers above the energy thresholds described in Section 6.2 for events with a dimuon mass in the range $3.05 \leq M_{\mu^+\mu^-} < 3.15$

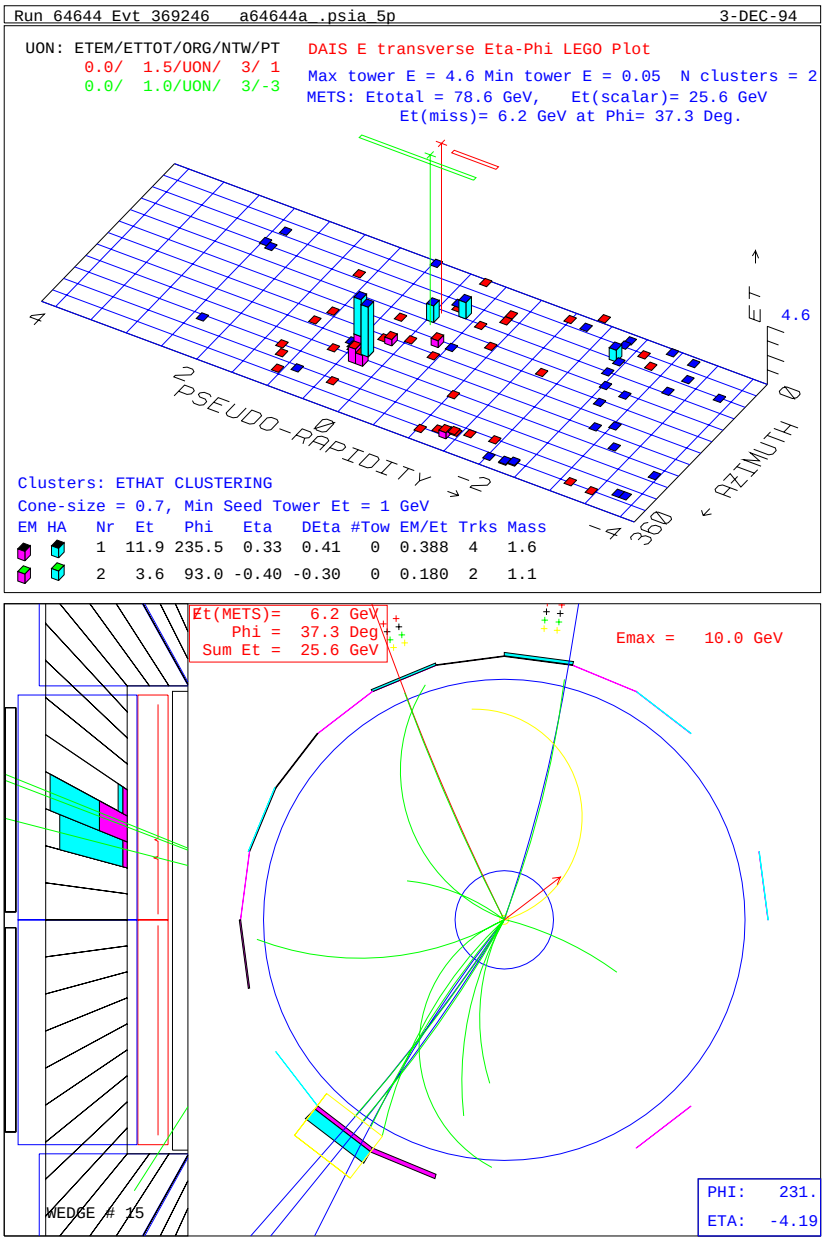

Figure 6.2: *Typical diffractive J/ψ candidate as observed in the detector. Top: η-ϕ lego plot of transverse energy deposited in the calorimeter. The plot shows two muons observed in muon chambers and one energetic jet with $E_T = 12$ GeV. Bottom: transverse view of the event and side view of the part of the central calorimeter with the detected jet.*

GeV/c^2 (see Fig. 6.4). Figure 6.3a shows this multiplicity plot for east and west sides superimposed, i.e. using two entries per event. There is a clear excess in the $N_{\rm BBC} = N_{\rm CAL} = 0$ bin, which is associated with a diffractive signal. Figure 6.3b shows the same distribution with only one entry per event, which is chosen to be the side with the minimum BBC multiplicity.

The diagonal bins ($N = N_{\rm BBC} = N_{\rm CAL}$) of the multiplicity distribution (Fig. 6.3b) are used to estimate the non-diffractive background in the (0,0) bin, since Monte Carlo studies of other diffractive processes (see for example [64]), as well as of this process (see Section 7.1), have shown that there is very little diffractive signal leaking into the non-zero diagonal multiplicity bins.

Both the non-J/ψ and non-diffractive backgrounds must be carefully subtracted in order to correctly evaluate the ratio of diffractive to non-diffractive J/ψ production.

6.4 Non-J/ψ Background

In order to measure the ratio of diffractive to non-diffractive J/ψ production, we first need to estimate the number of non-J/ψ events in the (0,0) bin. This is done by performing a binned log-likelihood fit of the dimuon mass spectrum in the (0,0) bin to the function

$$f(M) = \frac{p_1\,\Delta M}{\sqrt{2\pi}\,p_3}\,e^{-\frac{1}{2}\left(\frac{M-p_2}{p_3}\right)^2} + \frac{p_4}{N_{\rm bins}} \tag{6.1}$$

where $\Delta M = 0.01$ GeV/c^2 is the bin width and $N_{\rm bins} = 40$ is the number of bins in the fit. The fit parameters are $p_1, \ldots, p_4$, where p_1 represents the number of J/ψ events and p_4 the number of non-J/ψ events. To estimate the non-diffractive background in the (0,0) bin from the diagonal bins of the lower plot in Fig. 6.3, we also need to

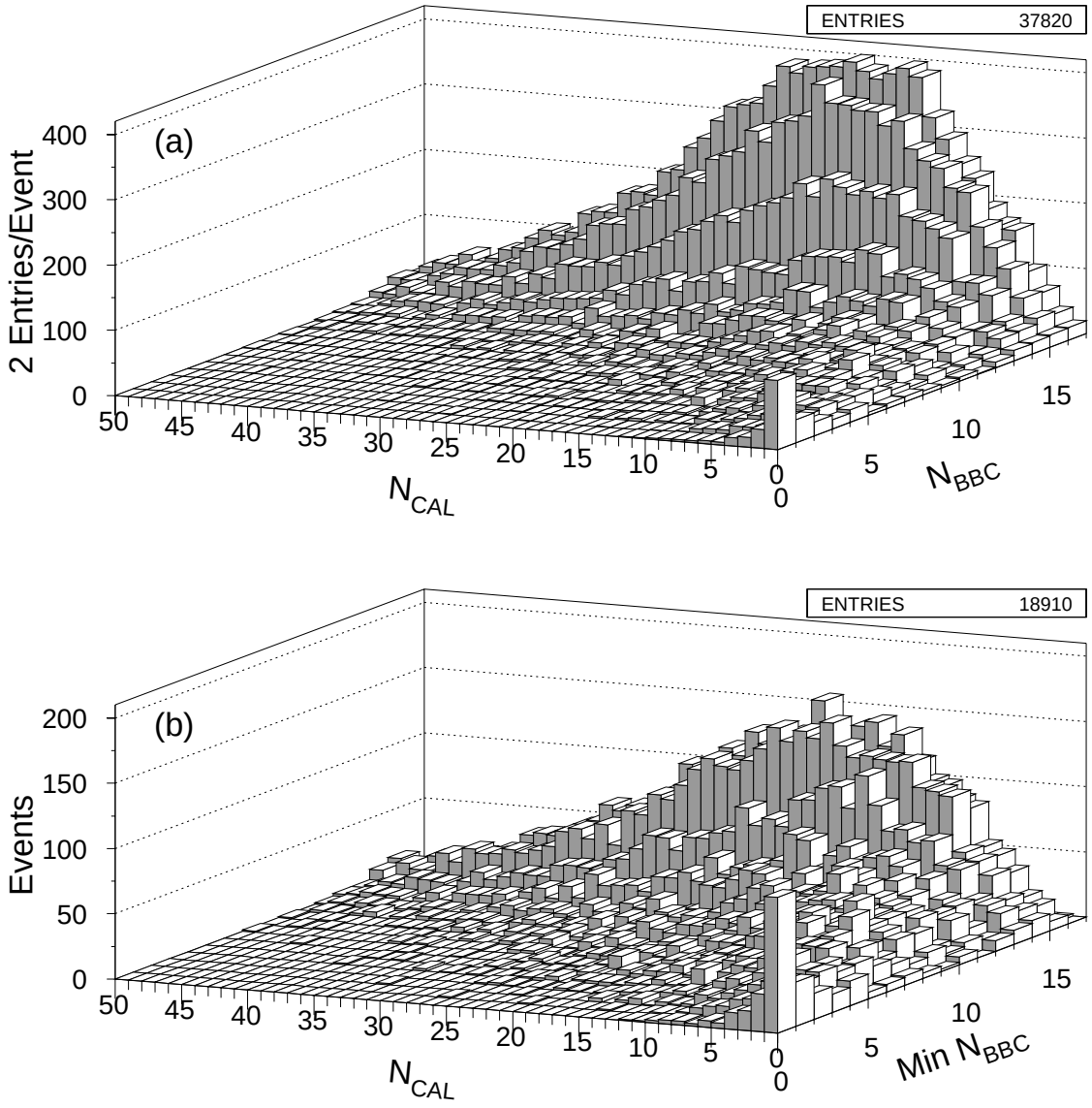

Figure 6.3: *(a) Multiplicity in calorimeter towers with* $2.4 < |\eta| < 4.2$ *versus BBC hit multiplicity on both east and west sides, i.e. two entries per event; (b) BBC hits versus calorimeter tower multiplicity only for the side of the detector with minimum BBC hit multiplicity.*

fit for the non-J/ψ background in the diagonal bins, as well as in the inclusive J/ψ candidate sample. In order to account for the muon final state radiation, the dimuon mass distribution of the inclusive J/ψ candidate sample is fitted to the sum of two Gaussians and a linear function. The fit results are displayed in Figs. 6.4 to 6.7 and summarized in Table 6.2. The fit yields the following result for the number of J/ψ events in the (0,0) bin:

$$N_{J/\psi}^{(0,0)} \;=\; 98.0 \;\pm\; 10.3 \tag{6.2}$$

6.5 Non-diffractive Background

To remove the non-diffractive component from the (0,0) bin, we plot the number of events as a function of diagonal multiplicity, *after* subtracting the non-J/ψ background, and perform an extrapolation to the zero-multiplicity bin of a linear fit to bins 2-12. The relevant plot is shown in Fig. 6.8. The fit to bins 2-12 yields

$N_{events} = a \times \text{Multiplicity} + b$
(*after* subtraction of non-J/ψ background)
$a = 2.52 \pm 0.60$
$b = 21.5 \pm 4.2$
$\chi^2/\text{Ndof} = 11.7/9$

Extrapolating to the (0,0) multiplicity bin yields a non-diffractive background of 21.5 ± 4.2 events. The diffractive J/ψ content of the (0,0) bin is therefore:

$$N_{\text{SD}\,J/\psi}^{(0,0)} \;=\; (98.0 \pm 10.3) \;-\; (21.5 \pm 4.2) \;=\; 76.5 \pm 11.1 \tag{6.3}$$

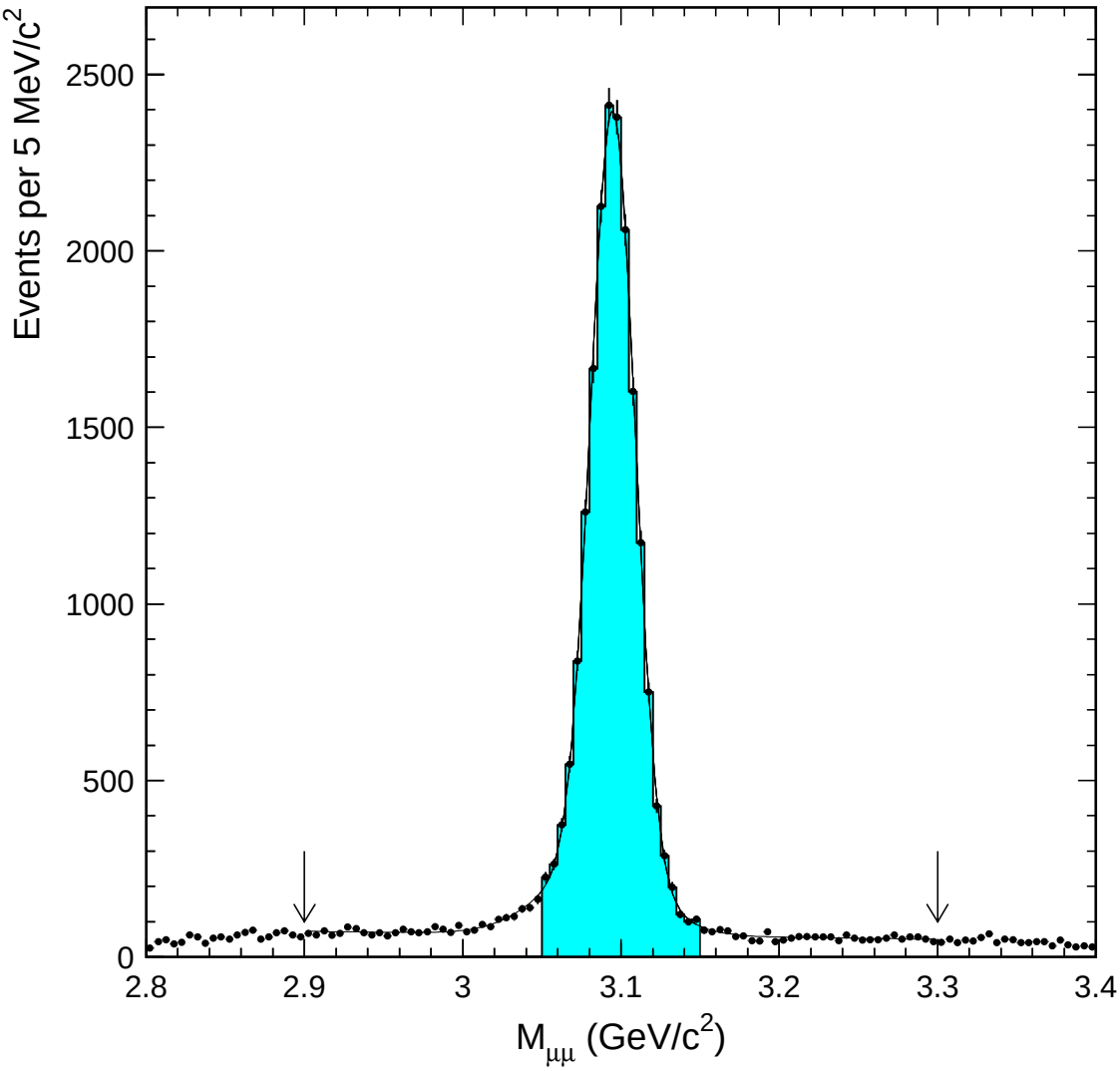

Figure 6.4: *Mass distribution of the J/ψ candidates. A fit to the function described in the text is superimposed. Shaded histogram shows the mass region for events used in the search for diffractive J/ψ production. The arrows indicate the mass region used in the fit.*

Multiplicity	N_{events}	$N(\text{non}-J/\psi)$	$N(J/\psi)$
0	104	6.0 ± 1.4	98.0 ± 10.3
1	34	0.3 ± 0.3	33.7 ± 5.8
2	25	0.6 ± 0.5	24.4 ± 5.0
3	41	1.4 ± 0.7	39.6 ± 6.4
4	23	1.0 ± 0.6	22.0 ± 4.8
5	38	2.5 ± 0.9	35.5 ± 6.2
6	48	2.2 ± 1.0	45.8 ± 7.0
7	50	2.6 ± 1.0	47.4 ± 7.1
8	42	1.6 ± 0.4	40.4 ± 6.5
9	47	1.1 ± 0.6	45.9 ± 6.9
10	48	4.3 ± 1.2	43.7 ± 7.0
11	46	4.0 ± 1.1	42.0 ± 6.9
12	63	6.6 ± 1.5	56.4 ± 8.1
Full sample	18910	1230 ± 27.5	17680 ± 140

Table 6.2: *Results of fits to the dimuon invariant mass distribution as a function of calorimeter tower and BBC multiplicity for events where the two multiplicities are equal. The first column indicates this common multiplicity. The second column gives the total number of events in the corresponding multiplicity bin. The third column provides the fit results for the number of non-J/ψ background events and fourth column gives the number of J/ψ events left after subtracting the background. The last line provides the result of a fit to the entire inclusive J/ψ candidate sample.*

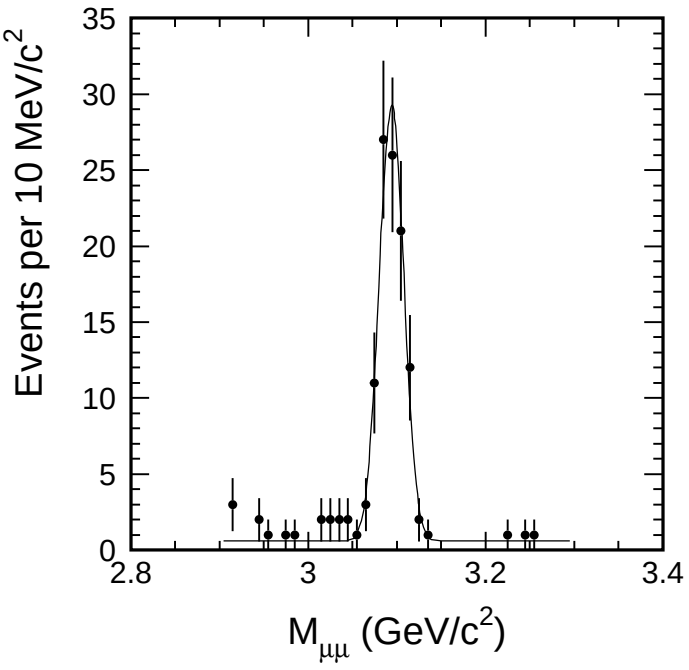

Figure 6.5: *Mass distribution of the diffractive J/ψ candidates ($N_{\rm BBC} = N_{\rm CAL} = 0$). A fit to the sum of a gaussian and a constant function is superimposed.*

6.6 Comparison of Diffractive and Non-diffractive J/ψ Event Kinematics

As shown in Section 6.5, the zero-multiplicity bin contains approximately 80% diffractive J/ψ's. Figures 6.9 and 6.10 show distributions of the J/ψ transverse momentum, the η, and the vertex z position for the events in the zero-multiplicity bin and for the total inclusive sample. The distributions for "diffractive" (zero multiplicity) and "non-diffractive" (inclusive) events are very similar.

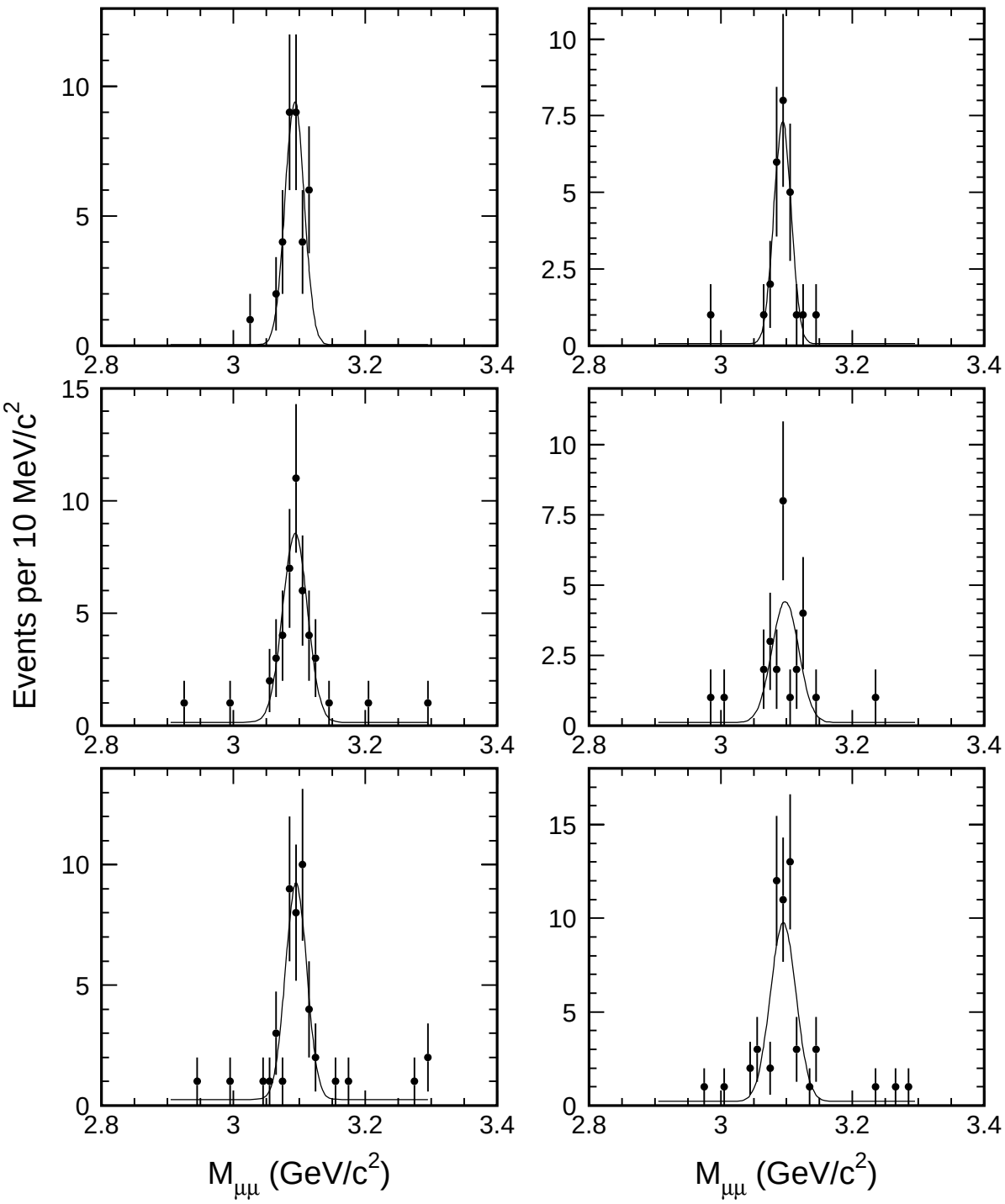

Figure 6.6: *Mass distribution for events with equal calorimeter tower and BBC multiplicities of 1,2,3,4,5 and 6. A fit to the sum of a gaussian and a constant function is superimposed on each distribution.*

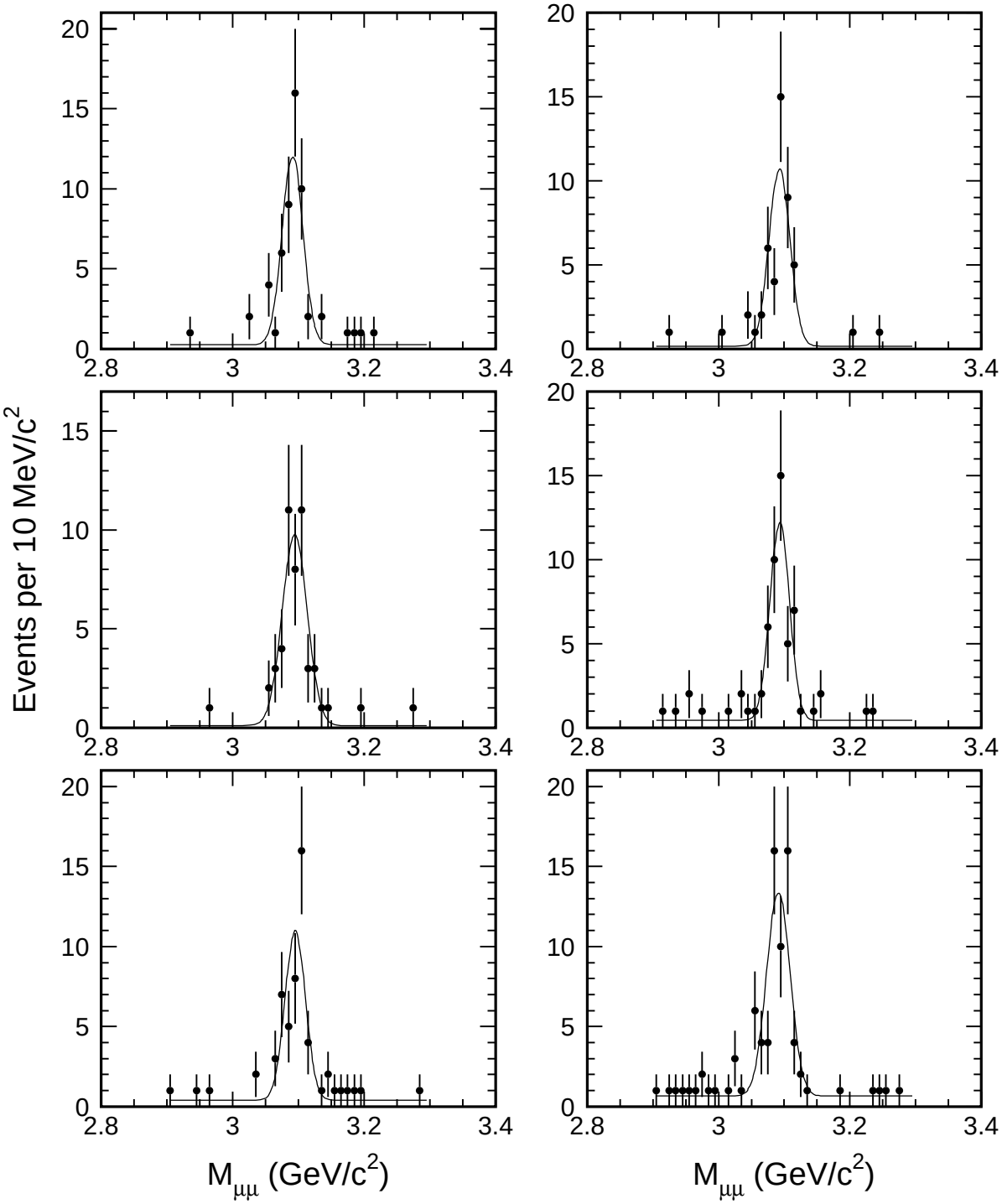

Figure 6.7: *Mass distribution for events with equal calorimeter tower and BBC multiplicities of 7,8,9,10,11 and 12. A fit to the sum of a gaussian and a constant function is superimposed on each distribution.*

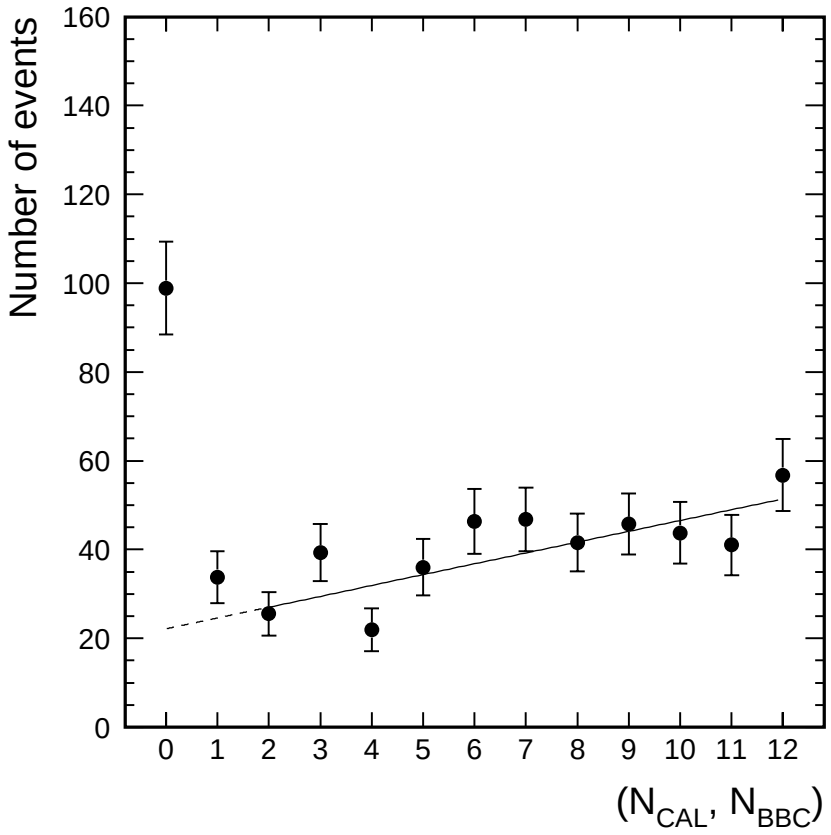

Figure 6.8: *J/ψ event counts in bins of equal BBC and calorimeter multiplicity (for $2.4 < |\eta| < 4.2$) as a function of multiplicity $N = N_{\rm CAL} = N_{\rm BBC}$. The linear fit in the region $2 \leq N \leq 12$ is extrapolated to $N = 0$ to estimate the non-diffractive background under the diffractive signal.*

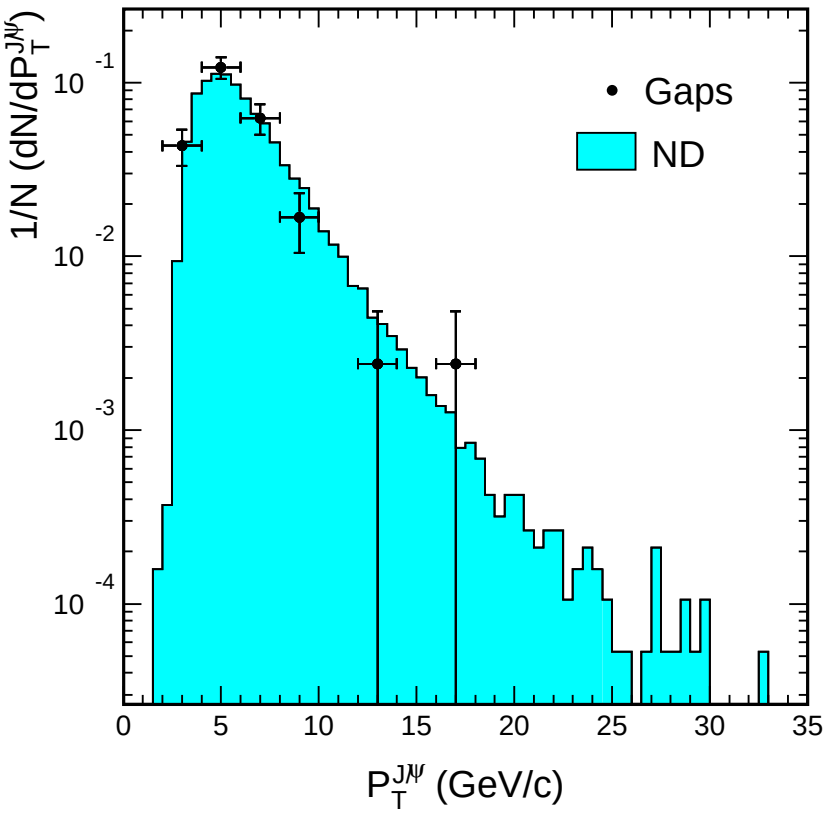

Figure 6.9: *J/ψ transverse momentum.*

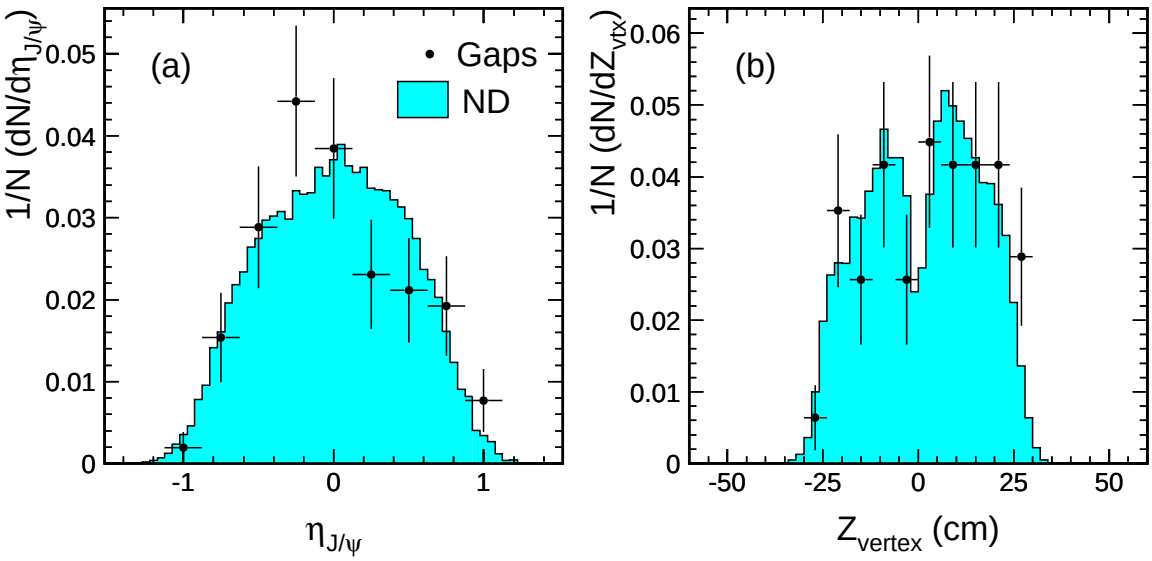

Figure 6.10: *(a) Pseudo-rapidity and (b) vertex z-position of diffractive candidate (points) and inclusive (shaded histograms) J/ψ events.*

6.7 Corrections

In order to evaluate the ratio of diffractive to non-diffractive J/ψ production, three effects need to be taken into account:

1. The occupancy of the BBC and of the forward calorimeters due to detector noise or beam halo, which hides a rapidity gap signal ("kills" the gap).

2. The one-vertex cut efficiency. The one-vertex requirement, aimed to exclude events with multiple interactions in a beam crossing, also rejects some single-interaction J/ψ events due to confusion in vertex reconstruction resulting in extra reconstructed vertices, particularly in events with high track multiplicity.

3. The gap acceptance, $\mathcal{A}_{\rm gap}$, defined as the fraction of single-diffractive interactions having a rapidity gap in the selected region $2.4 < |\eta| < 5.9$.

6.7.1 Forward Detector Live Time Efficiency

The forward detector live time efficiency, defined as the complement of the occupancy, was measured by studying the rate of hits in these detectors in a sample of trigger-unbiased events with no reconstructed primary vertex [65]. We will refer to such hits as "noise". Since the Run 1B minimum bias data were collected with the BBC trigger requirement activated, it was not possible to create an appropriate trigger-unbiased no-vertex sample from the data of this run. Therefore, Run 1A minimum bias data were used for this study. Figure 6.11 shows the probability of no-noise in the forward detectors as a function of instantaneous luminosity. Parameterizing the luminosity dependence of the no-noise probability using a linear function allows us to estimate the live time efficiency at the average luminosity of our run 1B J/ψ

sample.

The average luminosity of the sample is $7.3 \times 10^{30}\mathrm{cm}^{-2}\mathrm{s}^{-1}$. At this luminosity, the live time efficiencies obtained from Figure 6.11 for the east and west forward detectors are 0.825 and 0.766, respectively. The average of these two numbers is used as an overall live time efficiency,

$$\varepsilon_{\mathrm{Live}} = 0.80 \pm 0.03 \ .$$

6.7.2 Single Vertex Cut Efficiency

The one-vertex cut efficiency is defined as the number of events with one primary vertex divided by the number of single-interaction events. In order to evaluate the number of single-interaction events, we first calculate the number of minimum bias interactions per bunch crossing, which is given by

$$\bar{n} = \frac{C_{\mathrm{acc}} \cdot \mathcal{L}_{\mathrm{inst}} \cdot \sigma_{BBC}}{f} \tag{6.4}$$

where $\mathcal{L}_{\mathrm{inst}}$ is the instantaneous luminosity in units of $10^{30}\mathrm{cm}^{-2}\mathrm{s}^{-1}$, $C_{\mathrm{acc}} = 1 - 0.002704 \cdot \mathcal{L}_{\mathrm{inst}}$ is the accidental correction factor for $\mathcal{L}_{\mathrm{inst}}$ [66] , $\sigma_{BBC} = 51.15$ mb is the minimum bias cross section, and $f = 286.28$ is the frequency of the bunch crossing. The probability of zero extra minimum bias interactions per bunch crossing, which represents the fraction of single-interaction events, is then given by $e^{-\bar{n}}$, using Poisson statistics.

Some Level 2 triggers had *dynamic* prescaling, which depended on the instantaneous luminosity. In order to avoid bias, only events that pass the unprescaled Level 2 triggers ($\sim 60\%$ of all events) were used in the evaluation of the one-vertex cut efficiency. To study the luminosity dependence of the efficiency, the sample of J/ψ candidates passing all selection requirements was divided into luminosity bins

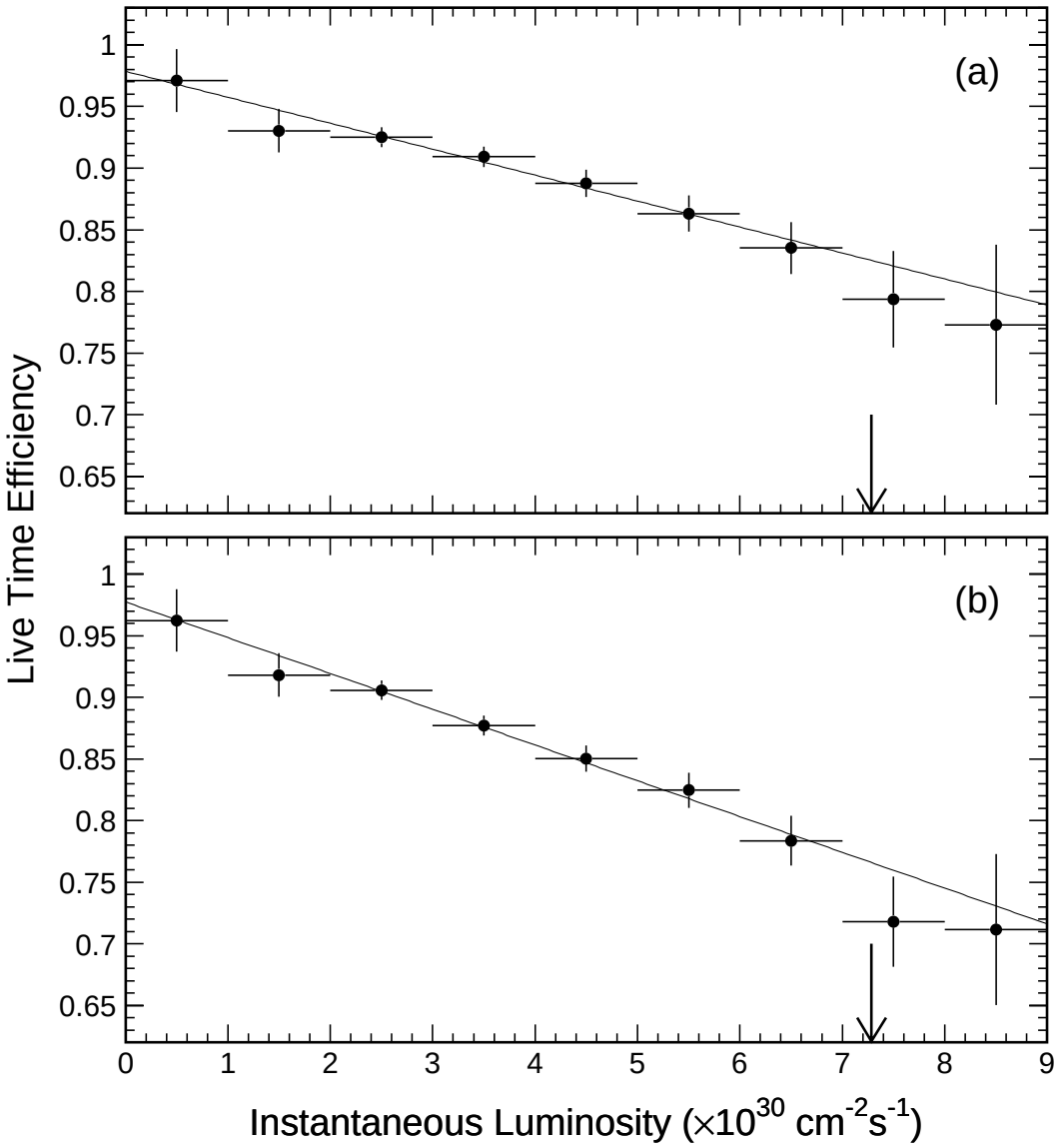

Figure 6.11: *Live time efficiency of forward "gap detectors" for east (a) and west (b) part of the CDF detector as a function of instantaneous luminosity for events with no reconstructed primary vertex from run 1A. The arrow indicates the mean value of instantaneous luminosity in the final J/ψ sample.*

of width $1 \times 10^{30}\text{cm}^{-2}\text{s}^{-1}$. The one-vertex cut efficiency obtained for different intervals of instantaneous luminosity is given in Table 6.3. From this analysis an overall efficiency of $(56.1 \pm 3.8)\%$ is derived, where the assigned uncertainty accounts for observed variations in efficiency as a function of instantaneous luminosity.

For diffractive events, the one-vertex cut efficiency was estimated by assuming that the probability of zero minimum bias interactions is 1, since particles produced from the extra minimum bias interaction would most likely spoil the rapidity gap. The one-vertex cut efficiency obtained for the single-diffractive J/ψ sample is 0.85 ± 0.03.

$\mathcal{L}_{\text{inst}}$, $10^{30}\text{cm}^{-2}\text{s}^{-1}$	N_{all}	$N_{1\text{vtx}}$	$R = N_{1\text{vtx}}/N_{\text{all}}$	$P_0 = e^{-\bar{n}}$	Efficiency, %
2-3	338	116	0.3432 ± 0.0260	0.6318	54.32 ± 4.12
3-4	1993	580	0.2910 ± 0.0102	0.5292	54.99 ± 1.93
4-5	6377	1549	0.2429 ± 0.0054	0.4471	54.33 ± 1.21
5-6	9985	2182	0.2185 ± 0.0041	0.3793	57.61 ± 1.08
6-7	10116	1823	0.1802 ± 0.0038	0.3197	56.37 ± 1.19
7-8	10103	1525	0.1509 ± 0.0036	0.2695	55.99 ± 1.34
8-9	9429	1251	0.1327 ± 0.0035	0.2275	58.33 ± 1.54
9-10	8407	964	0.1147 ± 0.0035	0.1921	59.71 ± 1.82
10-11	6910	583	0.0844 ± 0.0033	0.1620	52.10 ± 2.04
11-12	5462	409	0.0749 ± 0.0036	0.1372	54.59 ± 2.62
12-13	4028	262	0.0650 ± 0.0039	0.1161	55.99 ± 3.36
0-25	85252	11735	0.1377 ± 0.0012	0.2452	56.14 ± 0.49

Table 6.3: *Single-vertex cut efficiency. The first column indicates the luminosity interval. The second, third and fourth columns give the total number of events, the number of events with one reconstructed primary vertex, and the ratio of these two numbers, respectively. The fifth column provides the calculated probability of zero minimum bias interactions per bunch crossing, and the last column the one-vertex cut efficiency (ratio R/P_0).*

6.8 Ratio of Diffractive to Non-diffractive Events

Denoting by $R_{J/\psi}$ the fraction of J/ψ events produced by single-diffractive interactions, the measured diffractive fraction for events satisfying our rapidity gap definition is

$$R_{J/\psi} \times \mathcal{A}_{\rm gap} = \frac{N_{{\rm SD}\,J/\psi}}{N_{{\rm ND}\,J/\psi}} \times \frac{\varepsilon^{\rm ND}_{\rm 1vtx}}{\varepsilon^{\rm SD}_{\rm 1vtx}} \times \frac{1}{\varepsilon_{\rm Live}} \tag{6.5}$$

where $\mathcal{A}_{\rm gap}$ denotes the rapidity gap acceptance, i.e the fraction of diffractive J/ψ events satisfying our rapidity gap requirements (see Section 6.2).

Table 6.4 lists the estimated values of corrections factors in Eq. 6.5.

Correction Factor	Value	Uncertainty
$\varepsilon_{\rm Live}$	0.80	$\pm$0.03
$\varepsilon^{\rm ND}_{\rm 1vtx}$	0.561	$\pm$0.038
$\varepsilon^{\rm SD}_{\rm 1vtx}$	0.85	–

Table 6.4: *Correction factors.*

Thus, we find

$$\begin{aligned} R_{J/\psi} \times \mathcal{A}_{\rm gap} &= \frac{76.5 \pm 11.1}{17680 \pm 140} \times \frac{0.561 \pm 0.038}{0.85} \times \frac{1}{0.80 \pm 0.03} \\ &= [0.36 \pm 0.05({\rm stat}) \pm 0.03({\rm syst})]\%, \end{aligned} \tag{6.6}$$

where the statistical error combines in quadrature the uncertainties on the number of diffractive J/ψ events in the (0,0) bin and in the inclusive sample, and systematic error is due to uncertainties in $\varepsilon_{\rm 1vtx}$ and $\varepsilon_{\rm Live}$.

6.9 Study of B-hadron Decay Component in the J/ψ Event Sample

The fraction of the B-hadron decay background in our final J/ψ sample was estimated by using the precise measurement of the decay length provided by the SVX.

The invariant mass distribution of the final dimuon sample is shown in Figure 6.12. The light-shaded area indicates the J/ψ signal region $3.05 \leq M_{\mu^+\mu^-} < 3.15$ GeV/c^2. This region contains 18910 events. The dark-shaded area shows two sideband regions, one with mass from 2.8 to 3.0 GeV/c^2 and the other from 3.2 to 3.4 GeV/c^2. The sidebands, which contain 4457 events, were used to determine the shape of the lifetime distribution for background events in the J/ψ signal region. After background subtraction, the number of J/ψ's in the signal region is found to be 17680 ± 140 (see Table 6.2).

6.9.1 Definition of Proper Decay Length

For each J/ψ in the sample, a two dimensional decay distance L_{xy} was calculated, defined as the projection of the vector $\vec{X}$, pointing from the primary vertex to the secondary vertex, onto the transverse momentum of the J/ψ:

$$L_{xy} \equiv \frac{\vec{X} \cdot \vec{P_T}^{\psi}}{|\vec{P_T}^{\psi}|} \tag{6.7}$$

The position of the secondary vertex is obtained by constraining the two muon tracks to come from a common decay vertex. The primary vertex position is approximated by the mean beam position, determined run by run by averaging over many events. The uncertainty on L_{xy} is obtained using

$$\sigma(L_{xy}) = \frac{\sqrt{(\sigma_{xx}^2 + \sigma_p^2)P_x^2 + (\sigma_{yy}^2 + \sigma_p^2)P_y^2 + 2\sigma_{xy}^2 P_x P_y}}{P_T^B} \tag{6.8}$$

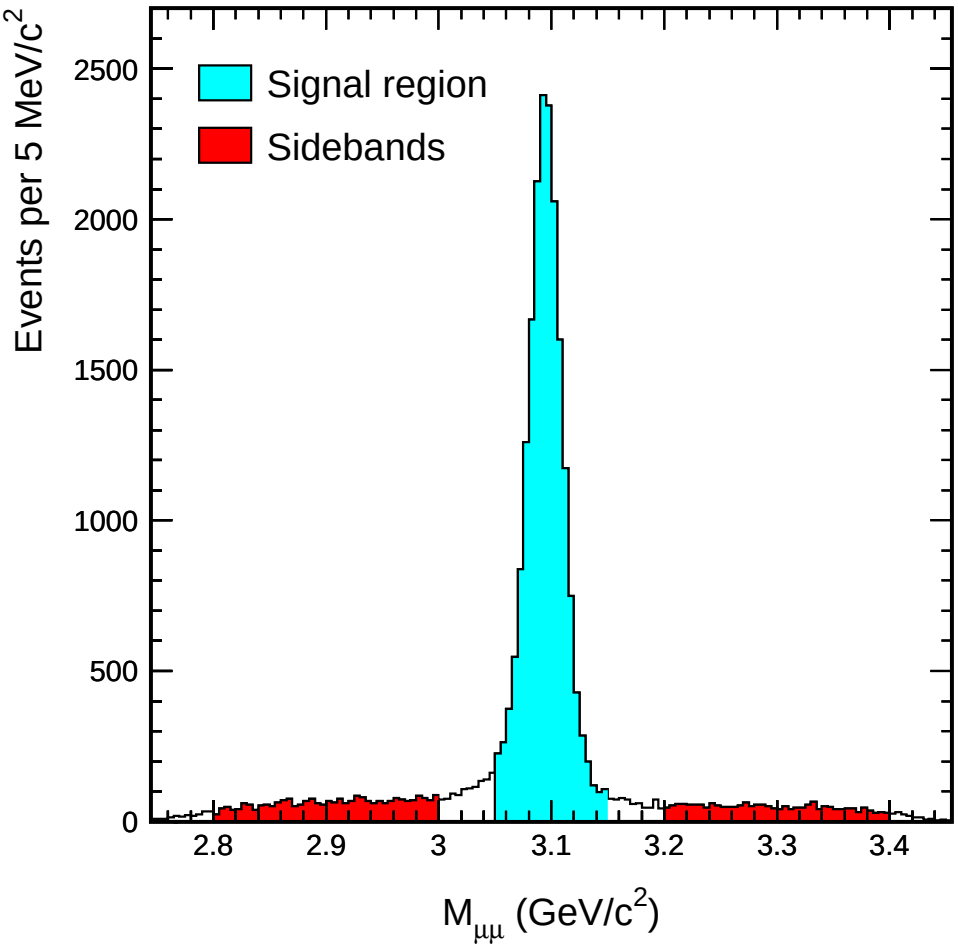

Figure 6.12: *Invariant mass distribution of oppositely charged dimuons after all selection cuts except for the mass cut. The shaded areas indicate the J/ψ signal (gray) and sideband (black) regions.*

where σ_{xx}, σ_{yy} and σ_{xy} are covariance matrix elements for the secondary vertex fit, σ_p is the uncertainty of the primary vertex (beam spot), and P_x and P_y are the x and y components of the B-hadron momentum, P_B.

To convert the transverse decay length into a proper lifetime, the relativistic quantity $(\beta\gamma)_B$ of the B hadron must be determined. Since the J/ψ selected by the dimuon trigger typically carries most of the momentum of the B hadron, the $(\beta\gamma)_\psi$ of the J/ψ is a good first approximation to $(\beta\gamma)_B$.

Using a Monte Carlo procedure, a $(\beta\gamma)$ correction factor $F_{\rm corr}$, which relates the boost factor $(\beta\gamma)_\psi$ of the J/ψ to the boost factor $(\beta\gamma)_B$ of the J/ψ parent B hadron, was calculated as a function of P_T^ψ. Details of this procedure can be found in the measurement of B-hadron lifetime [67]. The parameterization of $F_{\rm corr}(P_T^\psi)$ is given by

$$F_{\rm corr}(P_T^\psi) = 2.44 \cdot exp(-1.18 P_T^\psi) + 0.84 \tag{6.9}$$

The pseudo proper decay length, $c\tau$, is then calculated from L_{xy} using the equation

$$c\tau = L_{xy} \cdot \frac{M_{J/\psi}}{P_T^\psi \cdot F_{\rm corr}(P_T^\psi)} \tag{6.10}$$

6.9.2 Lifetime Distribution Fit

In order to obtain the B-hadron fraction from the $c\tau$ distribution, we fit to three sources of dimuon events in the J/ψ invariant mass region:

- J/ψ's from B decays.
- J/ψ's directly produced in $p\bar{p}$ collisions, or resulting from decay of intermediate states which are significantly short-lived so that their vertex is indistinguishable from the primary vertex (*e.g.* from χ_c's).

- Background coming from processes whose invariant mass falls accidentally in the J/ψ mass window: these events include dimuons from Drell-Yan production, double semileptonic b-quark decays, meson decays-in-flight and residual hadron punch-through. The shape of this contribution is obtained by fitting the corresponding J/ψ sideband distributions.

The first step in the fit is to determine the background $c\tau$ shape by fitting the $c\tau$ distribution for events from sidebands of the dimuon invariant mass distribution. The background fit is parameterized as a sum of a Gaussian function and three exponential tails, one symmetrical for both the negative and positive sides and two assymetrical, one for each side,

$$B_{bkg}(x) = (1 - f_+ - f_- - f_{sym})G(x, \sigma_{bkg}) + f_+ E(x, \lambda_+) + \frac{1}{2} f_{sym} E(x, \lambda_{sym}), \quad \text{if} x > 0$$

$$B_{bkg}(x) = (1 - f_+ - f_- - f_{sym})G(x, \sigma_{bkg}) + f_- E(-x, \lambda_-) + \frac{1}{2} f_{sym} E(-x, \lambda_{sym}), \text{if} x \leq 0$$

where the normalized Gaussian and exponential functions are:

$$G(x, \sigma) = \frac{1}{\sqrt{2\pi}\sigma} exp(-\frac{x^2}{2\sigma^2}) \tag{6.11}$$

$$E(x, \lambda) = \frac{1}{\lambda} exp(-\frac{|x|}{\lambda}) \tag{6.12}$$

The background fit parameters are:

f_-	fraction of the negative exponential
f_+	fraction of the positive exponential
f_{sym}	fraction of the symmetrical exponential
λ_-	slope of the negative exponential
λ_+	slope of the positive exponential
λ_{sym}	slope of the symmetrical exponential
σ_{bkg}	width of the gaussian

The pseudo-$c\tau$ distribution of the side bands is shown in Figure 6.13. Table 6.5 summarizes the values of the fitted parameters and the errors thereof. The distribution is clearly asymmetric, with a larger tail at positive lifetimes. An asymmetric background $c\tau$ distribution would be expected, since the dimuon sample contains events from sequential semileptonic b-quark decays ($b \to c\mu\nu \to s\mu\nu\mu\nu$).

Parameter		Value	Uncertainty
f_-	(%)	8.07	$\pm$0.93
f_+	(%)	16.4	$\pm$1.03
f_{sym}	(%)	31.7	$\pm$0.94
λ_-	(μm)	5080	$\pm$780
λ_+	(μm)	770	$\pm$60
λ_{sym}	(μm)	168	$\pm$12.7
σ_{bkg}	(μm)	43.1	$\pm$1.56

Table 6.5: *Parameters of the background fit.*

The pseudo-$c\tau$ distribution for the signal region consists of three components: prompt J/ψ's, B-decay contribution, and the non-J/ψ background described above.

The prompt J/ψ component is parameterized as

$$P(x) = (1 - f_{tail})G(x, \sigma_{J/\psi}) + \frac{1}{2} f_{tail} E(x, \lambda_{tail}) \tag{6.13}$$

where f_{tail} and λ_{tail} are the fraction and slope of the exponential tail, and $\sigma_{J/\psi}$ is the width of the gaussian for the prompt J/ψ component.

The B-decay contribution is determined by convoluting the prompt shape function $P(x)$ with an exponential according to the formula

$$B(x) = \int_0^\infty P(y - x) \cdot E(y, \lambda_B) dy \tag{6.14}$$

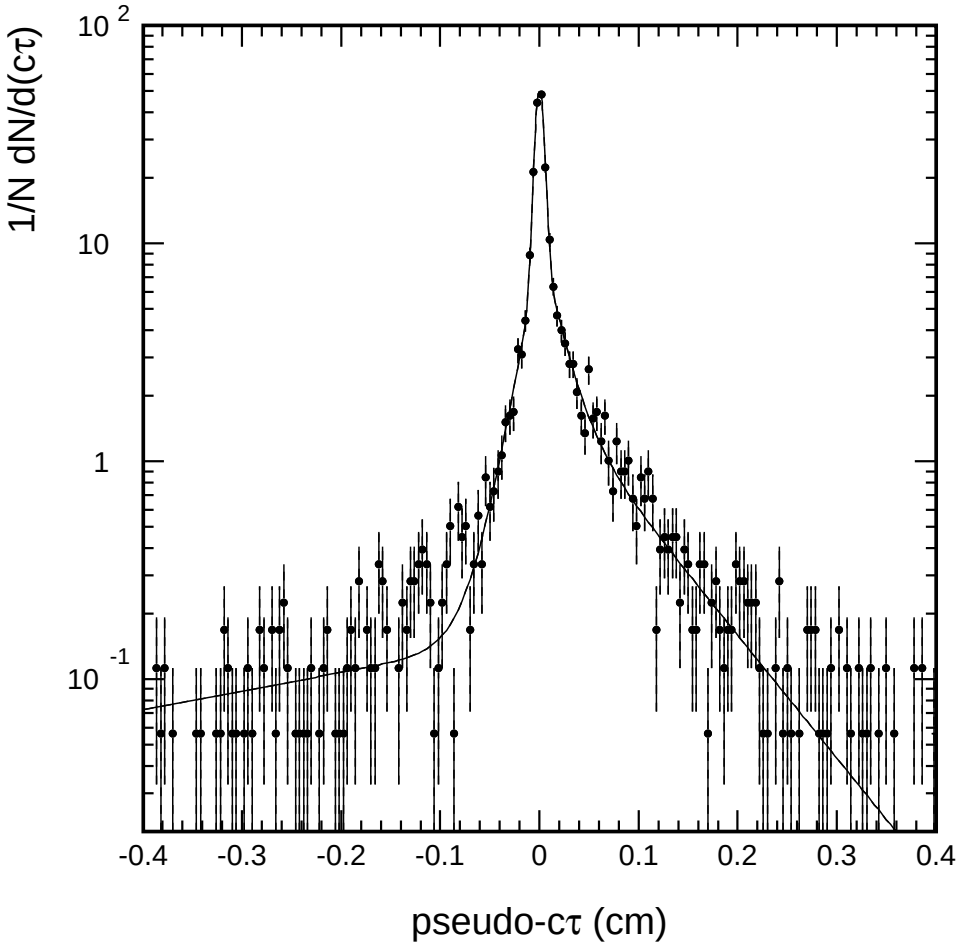

Figure 6.13: *Pseudo-$c\tau$ distribution for sideband region events with the fit to the* background *shape function superimposed.*

where λ_B is the average B lifetime. The analytical form of the integral 6.14 is provided in Appendix A. For our lifetime fit the λ_B is fixed at 460 μm, as found by the CDF inclusive B-hadron lifetime measurement [67].

The functional form for the J/ψ signal, $S(x)$, consisting of prompt and B components, is given by

$$S(x) = (1 - f_B)P(x) + f_B B(x) \tag{6.15}$$

where f_B is the fraction of the B-decay contribution, which we seek to estimate.

The total fitted function $T(x)$ in the signal region is then

$$T(x) = (1 - f_{bkg})S(x) + f_{bkg}B_{bkg}(x) \tag{6.16}$$

where f_{bkg} is the fraction of background events in the signal region, which was evaluated in the dimuon invariant mass fit and fixed at 0.065 for this fit.

The parameters of the signal region $c\tau$ distribution fit are:

f_B	fraction of J/ψ's from B decay
f_{bkg}	background fraction
f_{tail}	fraction of the exponential tail
λ_{tail}	slope of the exponential tail
$\sigma_{J/\psi}$	width of the prompt gaussian

Figure 6.14 shows the pseudo-$c\tau$ distribution for the signal region with a fit to the function $T(x)$ superimposed. The fit parameters and errors thereof are summarized in Table 6.6.

Figure 6.15 shows the three different contributions used in our fit of the signal region $c\tau$ distribution. The dark-shaded area shows the background contribution, the light-shaded region shows the contribution from B decays, and the unshaded region the contribution from prompt J/ψ's.

Figure 6.16 shows the fitted prompt J/ψ and B-hadron decay contributions.

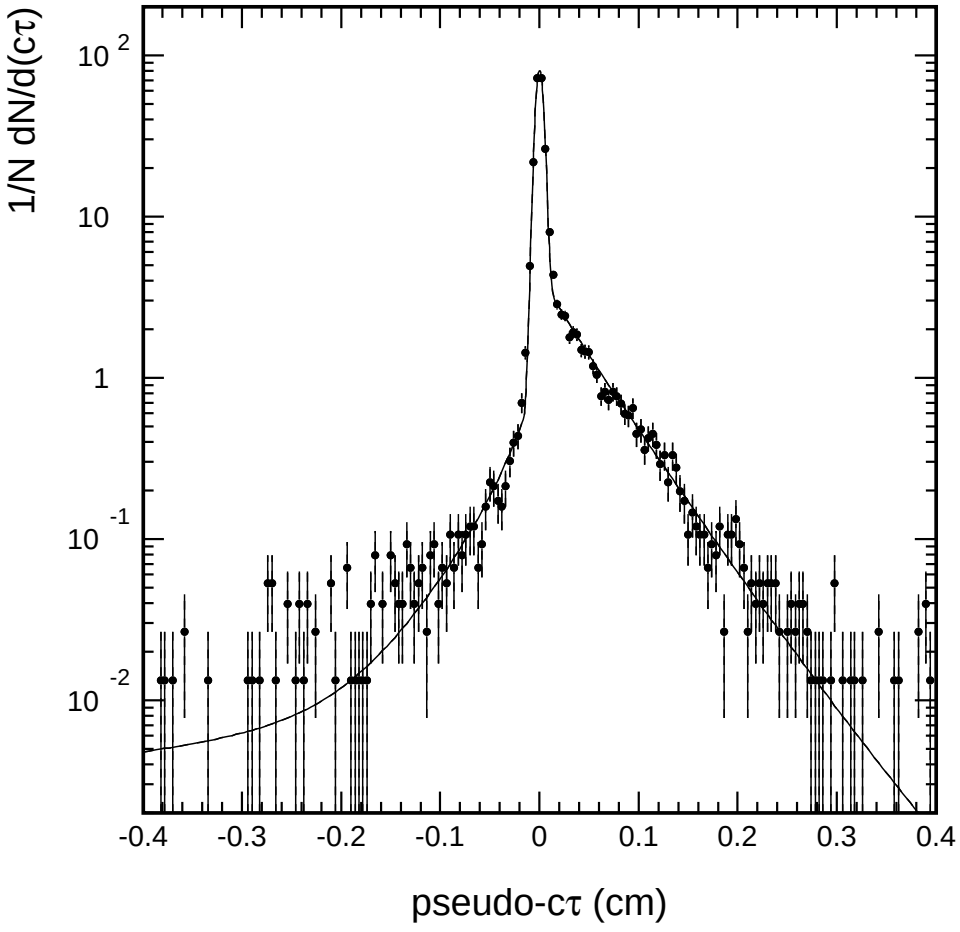

Figure 6.14: *Pseudo-$c\tau$ distribution for events in the signal region with the fit to the sum of three contributions from prompt J/ψ's, J/ψ's from B-hadron decays, and non-J/ψ background superimposed.*

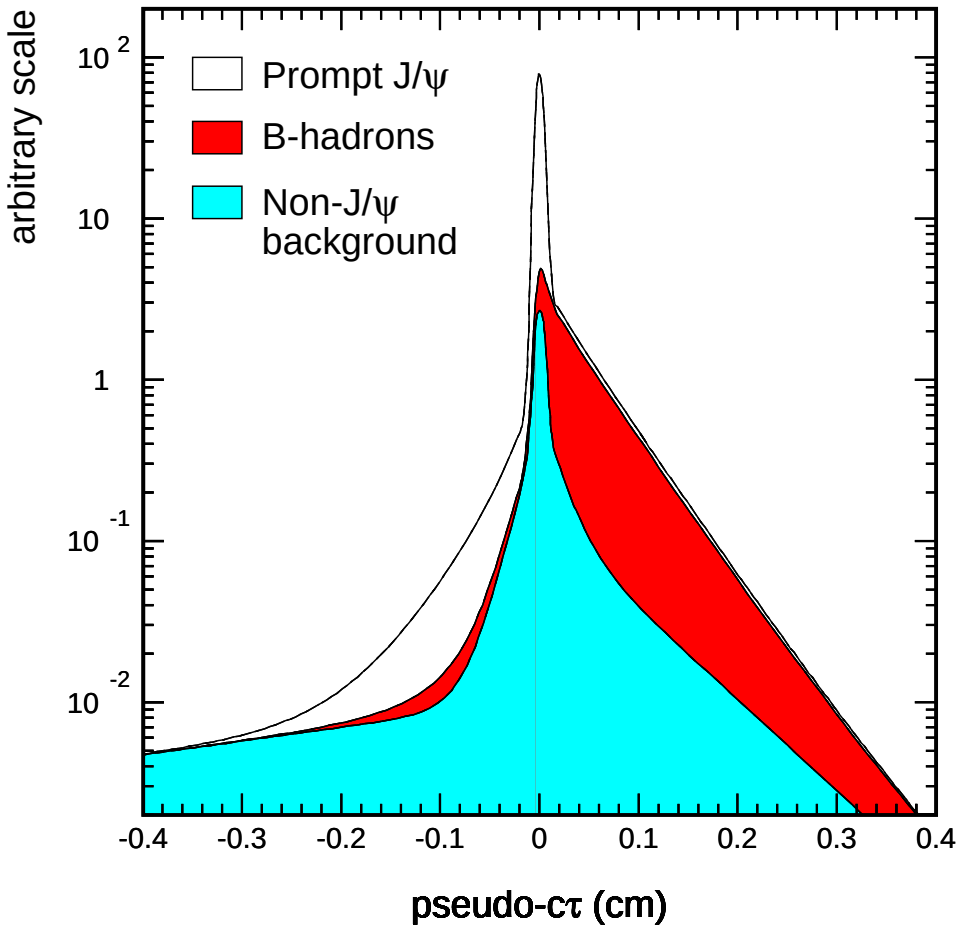

Figure 6.15: *Contributions from the three sources of dimuon events, (prompt J/ψ, B-hadron and non-J/ψ background) in the signal region of the $c\tau$ distribution.*

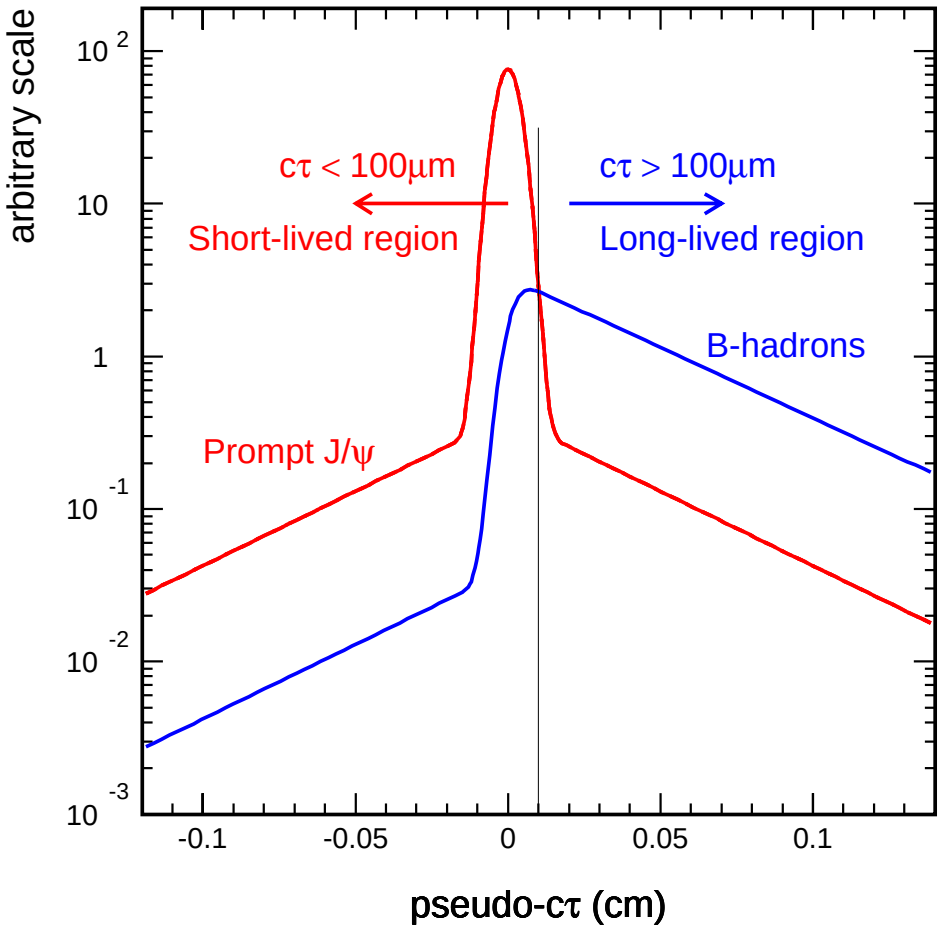

Figure 6.16: *The prompt J/ψ and B-decay components of the pseudo-$c\tau$ distribution.*

Parameter		Value	Uncertainty
f_B	(%)	16.78	$\pm$0.38
f_{tail}	(%)	4.60	$\pm$0.38
λ_{tail}	(μm)	445	$\pm$68
$\sigma_{J/\psi}$	(μm)	39.0	$\pm$0.34

Table 6.6: *Parameters of the pseudo-$c\tau$ distribution fit in the signal region.*

The vertical line at 100 μm separates two regions, a long-lived region dominated by B-decay contribution, and a short-lived region consisting mostly of prompt J/ψ's. By integrating numerically the fitted prompt and B-decay J/ψ components, we obtain estimates of the contamination of the J/ψ sample by B-hadron decay background in these two regions. The results are presented in Table 6.7.

		$c\tau \leq 100$ μm	$c\tau > 100$ μm
$F_{pJ/\psi}$	(%)	97.7	2.3
F_B	(%)	19.8	80.2

Table 6.7: *Fractions of prompt J/ψ and B-decay contributions in the short- and long-lived $c\tau$ regions, calculated by numerical integration of the $c\tau$ fit results.*

Multiplying the overall fraction $f_B = 16.78\%$ of the B-decay contribution in our final J/ψ sample (Table 6.6) by the fraction $F_B = 19.8\%$ of the B-hadron background contained within the $c\tau \leq 100$ μm cut (Table 6.7) yields 3.3% for the background in events that satisfy the $c\tau \leq 100$ μm cut. The number of events left in our J/ψ sample after applying the $c\tau \leq 100$ μm cut is 15824. In our further analysis we only use the sample of events after the $c\tau$ cut.

Multiplicity	$N_{\rm events}$	$N(\text{non}-J/\psi)$	$N(J/\psi)$
0	92	4.6 ± 1.2	87.4 ± 9.7
1	25	0.3 ± 0.3	24.7 ± 5.0
2	22	0.6 ± 0.3	21.4 ± 4.7
3	37	0.8 ± 0.5	36.2 ± 6.1
4	19	0.7 ± 0.5	18.3 ± 4.4
5	33	2.1 ± 0.8	30.9 ± 5.8
6	40	3.2 ± 1.0	36.8 ± 6.4
7	45	2.0 ± 1.0	43.0 ± 6.8
8	34	1.2 ± 0.6	32.8 ± 5.9
9	40	1.1 ± 0.6	38.9 ± 6.3
10	36	2.8 ± 1.0	33.2 ± 6.1
11	36	3.3 ± 1.1	32.7 ± 6.1
12	53	4.5 ± 1.2	48.5 ± 7.4
Full sample	15824	916 ± 23	13339 ± 128

Table 6.8: *Results of fits of the dimuon invariant mass distribution as a function of calorimeter tower and BBC multiplicity for prompt-J/ψ events for which the two multiplicities are equal.*

6.10 Fraction of Diffractive Prompt-J/ψ Events

The diffractive prompt-J/ψ content of the (0,0) bin is

$$N^{(0,0)}_{\text{SD}pJ/\psi} \;=\; (87.4 \pm 9.7) \;-\; (19.9 \pm 3.9) \;=\; 67.5 \pm 10.4 \tag{6.17}$$

where the non-diffractive background of 19.9 ± 3.9 events was obtained by extrapolating a linear fit to the values of bins 2-12 of column 4 of Table 6.8 to bin 0. Similar to expression of Eq. 6.5, the measured fraction of diffractive prompt J/ψ events satisfying our gap definition is given by

$$R_{pJ/\psi} \times \mathcal{A}_{\text{gap}} = \frac{N_{\text{SD}pJ/\psi}}{N_{\text{ND}pJ/\psi}} \times \frac{\varepsilon^{\text{ND}}_{\text{1vtx}}}{\varepsilon^{\text{SD}}_{\text{1vtx}}} \times \frac{1}{\varepsilon_{\text{Live}}} \tag{6.18}$$

where $\mathcal{A}_{\text{gap}}$ denotes the rapidity gap acceptance. The correction factors are presented in Table 8.3.

Correction Factor	Value	Uncertainty
$\varepsilon_{\rm Live}$	0.80	± 0.03
$\varepsilon^{\rm ND}_{\rm 1vtx}$	0.573	± 0.038
$\varepsilon^{\rm SD}_{\rm 1vtx}$	0.86	–

Table 6.9: *Correction factors.*

Applying all corrections, from Eq. 6.18 obtain

$$\begin{aligned} R_{pJ/\psi} \times \mathcal{A}_{\rm gap} &= \frac{67.5 \pm 10.4}{13339 \pm 128} \times \frac{0.573 \pm 0.038}{0.86} \times \frac{1}{0.80 \pm 0.03} \\ &= [0.42 \pm 0.06({\rm stat}) \pm 0.03({\rm syst})]\% \end{aligned} \tag{6.19}$$

The corresponding ratio for $\bar{b}b$ production [1] with the same rapidity gap definition is

$$R_{\bar{b}b} \times \mathcal{A}_{\rm gap} = [0.23 \pm 0.07({\rm stat}) \pm 0.05({\rm syst})]\%$$

Since both J/ψ and $\bar{b}b$ diffractive production are sensitive mostly to the *gluon* content of the pomeron, the difference between the two measured ratios must be due to the different kinematical regions probed in the two measurements, corresponding to different regions of $x_{\rm bj}$. This topic is discussed in detail in Section 8.4.

Chapter 7

Monte Carlo Studies

7.1 Monte Carlo Studies

This analysis is based on the rapidity gap (RG) method, which identifies diffractive J/ψ events by the presence of a large RG in a forward region. Not all diffractive events produced with ξ values within a given range satisfy our rapidity gap requirements. The fraction of events satisfying these requirements is defined as the *rapidity gap acceptance* for the given ξ range.

The RG acceptance is evaluated using a MC simulation. For a reliable acceptance calculation, the simulation must generate diffractive events with a correct underlying event as well as correct J/ψ kinematics.

We first generated a sample of non-diffractive J/ψ events using the PYTHIA 5.7 Monte Carlo program [69]. The standard PYTHIA uses the Color Singlet Model (CSM) as a mechanism of J/ψ hadroproduction. This model underestimates the magnitude of the J/ψ cross section measured at the Tevatron [30], and does not describe the shape of the p_T distribution. These discrepancies are overcome by incorporating

the Color Octet Model (COM) in PYTHIA.

The following α_s^3 partonic processes contribute to J/ψ hadroproduction:

$$g + g \rightarrow J/\psi + g$$
$$g + g \rightarrow J/\psi + q$$
$$q + \bar{q} \rightarrow J/\psi + g$$

The COM was implemented in PYTHIA [70] by modifying the routine PYSIGH (ISUB=86) for the partonic process $g + g \rightarrow J/\psi + g$ to include contributions from ${}^3S_1^{(8)}$, ${}^1S_0^{(8)}$ and ${}^3P_1^{(8)}(J = 0, 1, 2)$ colored states in ${}^3S_1$ charmonium hadroproduction [36]. Studies using the modified PYTHIA [70] show that gluon-gluon scattering is the dominant process in J/ψ hadroproduction, as expected, gluon-quark scattering contributes $\simeq 20\%$, and quark-antiquark scattering represents a tiny contribution, which is ignored in our simulation. The modified code of the ISUB=86 routine is presented in Appendix B.

The muons from the generated sample of $J/\psi \rightarrow \mu^+ + \mu^-$ events were restricted to the central pseudorapidity range of $|\eta| < 1.0$. The CTEQ2L set of parton distribution functions (PDFs) was used for the proton, and detector effects were simulated by QFL. The same set of selection criteria was applied to the generated J/ψ events as to the data. Figure 7.1 shows the transverse momentum distributions for Monte Carlo generated J/ψ events and for the data.

The shaded histogram shows the p_T distribution for Monte Carlo events generated by PYTHIA with only the CSM implemented. A comparison between distributions of muon transverse momentum, pseudorapidity and vertex z-position from the dimuon vertex constrained fit for MC generated non-diffractive J/ψ events and for data is presented in Figure 7.2. The Monte Carlo distributions are in good agreement with the data, suggesting that the corrected PYTHIA can be used reliably in diffractive gap acceptance calculations.

The distribution of calorimeter tower multiplicity versus BBC hit multiplicity for MC generated non-diffractive J/ψ events is shown in Fig. 7.3. The multiplicity distribution of calorimeter towers is in general agreement with the non-diffractive data (see Fig. 6.3b), while the saturation effect of the BBC observed in the data is poorly reproduced by detector simulation program. Despite of these facts leading to a higher non-diffractive contribution in low multiplicity bins, the expected non-diffractive background in the $(0,0)$ bin used to extract diffractive signal is very small, and changes slowly along the diagonal bins ($N = N_{\rm BBC} = N_{\rm CAL}$) of the multiplicity distribution.

Diffractive J/ψ production was simulated using the POMPYT 2.6 Monte Carlo program [71]. Three different parton distribution functions (PDF) for the Pomeron were used, characterized by their functional dependence on β, the momentum fraction of the pomeron carried by its parton participating in the J/ψ production:

- hard gluon $\beta f_g(\beta) = 6\beta(1-\beta)$
- flat gluon $\beta f_g(\beta) = 1$
- $1/\beta$ $\beta f_g(\beta) = 1/\beta$

The $1/\beta$ PDF is similar to the distribution reported in our diffractive dijet Roman

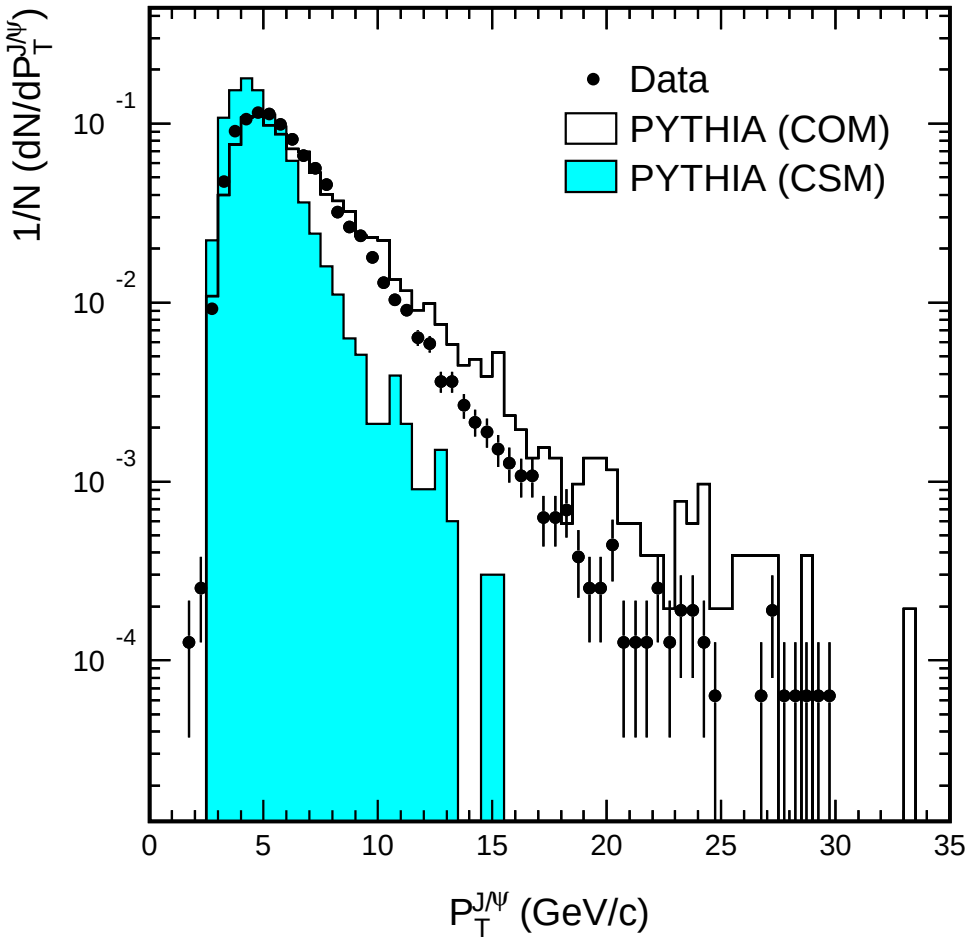

Figure 7.1: *J/ψ transverse momentum distribution compared with the prediction of the standard PYTHIA Monte Carlo (shaded histogram) and the modified PYTHIA incorporating the color-octet model (COM) for J/ψ production (solid histogram).*

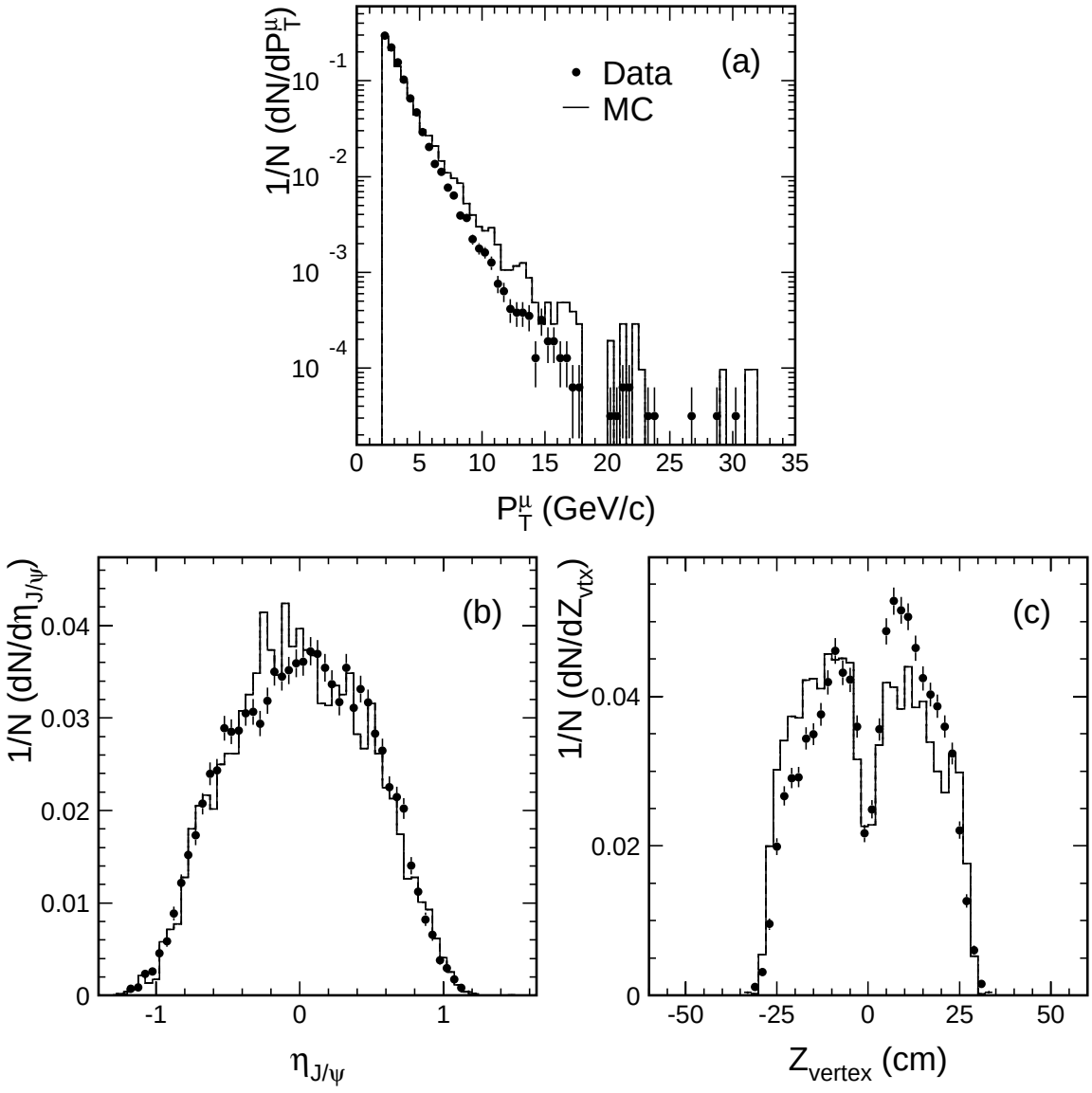

Figure 7.2: *(a) Muon transverse momentum, (b) pseudo-rapidity and (c) vertex z-position of J/ψ candidates (points) compared with the prediction of the modified PYTHIA Monte Carlo simulation (solid histogram).*

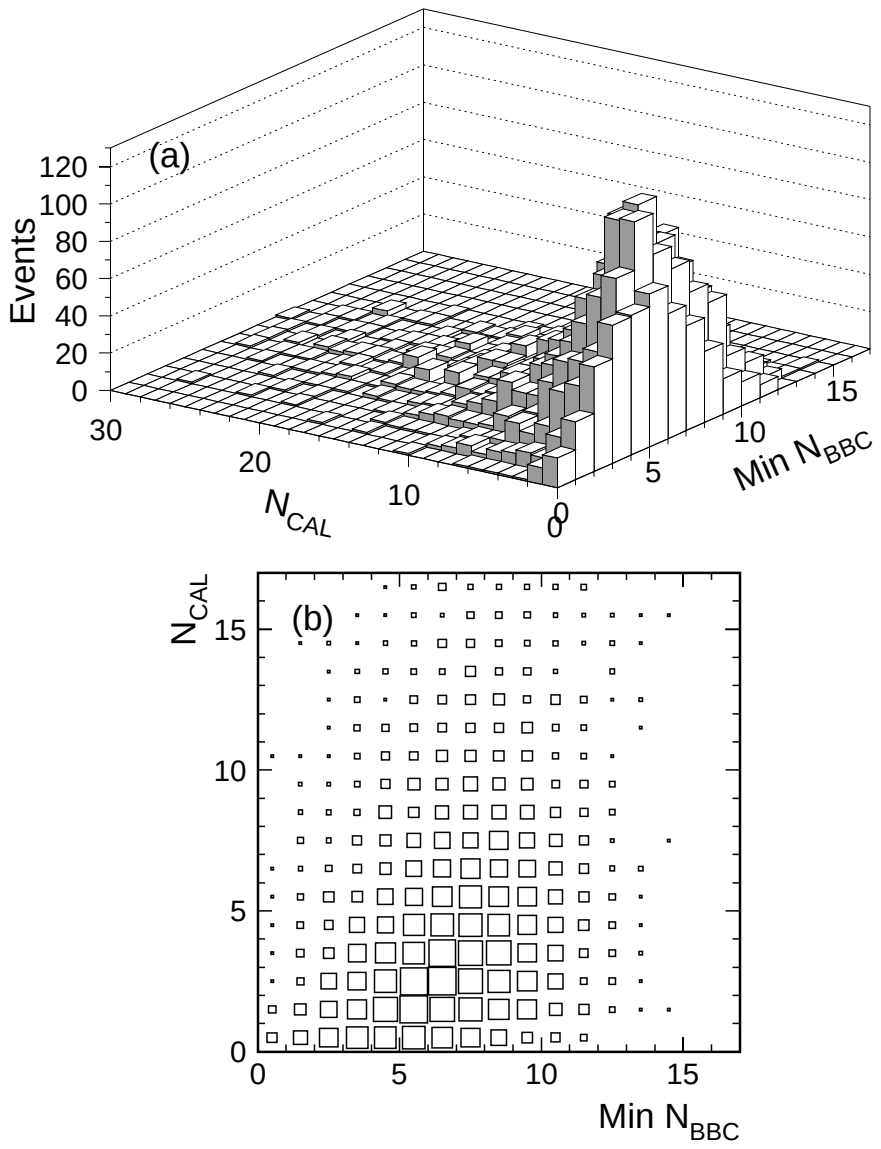

Figure 7.3: *Multiplicity of calorimeter towers versus BBC hits on the η-side of the detector with minimum BBC hit multiplicity for non-diffractive J/ψ events generated with the modified PYTHIA.*

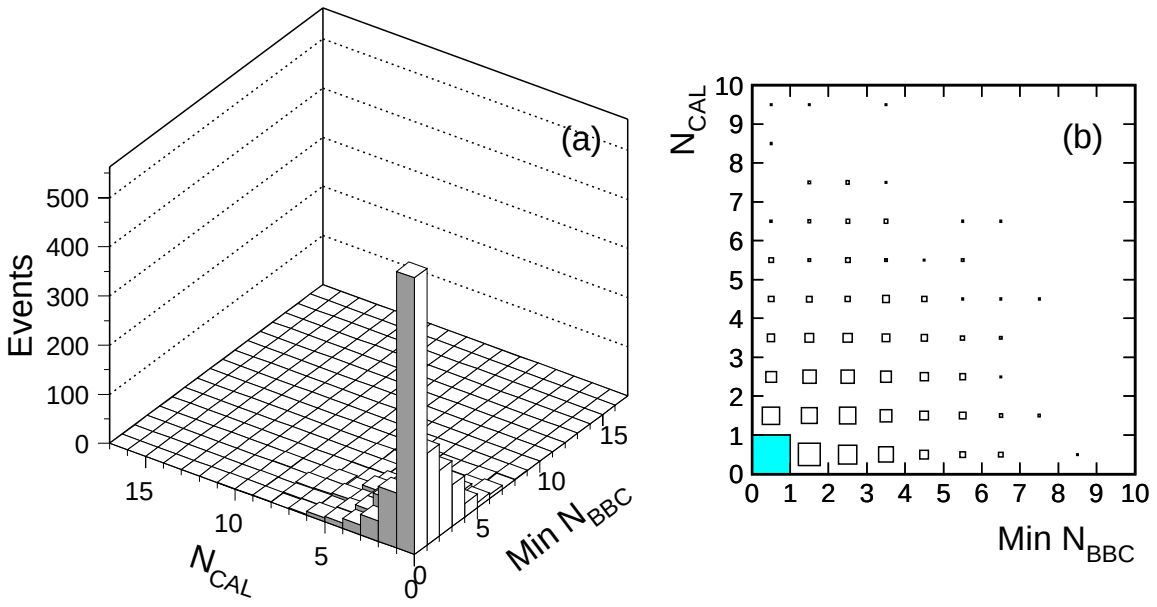

Figure 7.4: *Multiplicity of calorimeter towers versus minimum BBC hit multiplicity for diffractive J/ψ events generated with POMPYT incorporating the modified PYTHIA and using a $1/\beta$ pomeron structure function.*

Pot paper [22].

The distributions of calorimeter tower multiplicity versus minimum BBC hit multiplicity for diffractive J/ψ events generated using a $1/\beta$ PDF is shown in Figure 7.4. The obtained rapidity gap acceptances for events generated with $\xi < 0.1$ and corresponding pomeron PDF are presented in Table 7.1.

Pomeron PDF	Gap Acceptance
Hard Gluon	0.21
Flat Gluon	0.30
$1/\beta$	0.29

Table 7.1: *Rapidity gap acceptance for diffractive J/ψ events of $\xi < 0.1$ for different Pomeron PDFs.*

Figure 7.5 shows the transverse momentum, pseudorapidity, and vertex z-

position distributions of our diffractive J/ψ candidate events compared with the predictions of POMPYT based on the modified PYTHIA Monte Carlo using a $1/\beta$ pomeron structure function.

The ratio of diffractive to non-diffractive prompt-J/ψ production after correction for the gap acceptance, $\mathcal{A}_{\rm gap} = 0.29$, is

$$R_{pJ/\psi} = (1.45 \pm 0.25)\%. \tag{7.1}$$

The ξ and β distributions for the generated diffractive J/ψ events are presented in Figure 7.6. The shaded histograms are for the events with a rapidity gap ($N_{\rm BBC} = N_{\rm CAL} = 0$).

Figure 7.7 shows the multiplicity distribution of BBC hits versus calorimeter towers within the range $0.01 \leq \xi \leq 0.03$, which is the ξ-region of high acceptance in our diffractive data (see Section 8.3), for diffractive Monte Carlo generated events. The rapidity gap acceptance of the (0,0) bin for diffractive events with ξ in the region $0.01 \leq \xi \leq 0.03$ derived from this multiplicity distribution is

$$A^{\xi}_{\rm gap} = 0.79$$

This number is in agreement with the value of 0.87 ± 0.13 obtained in Section 8.3 from data considerations.

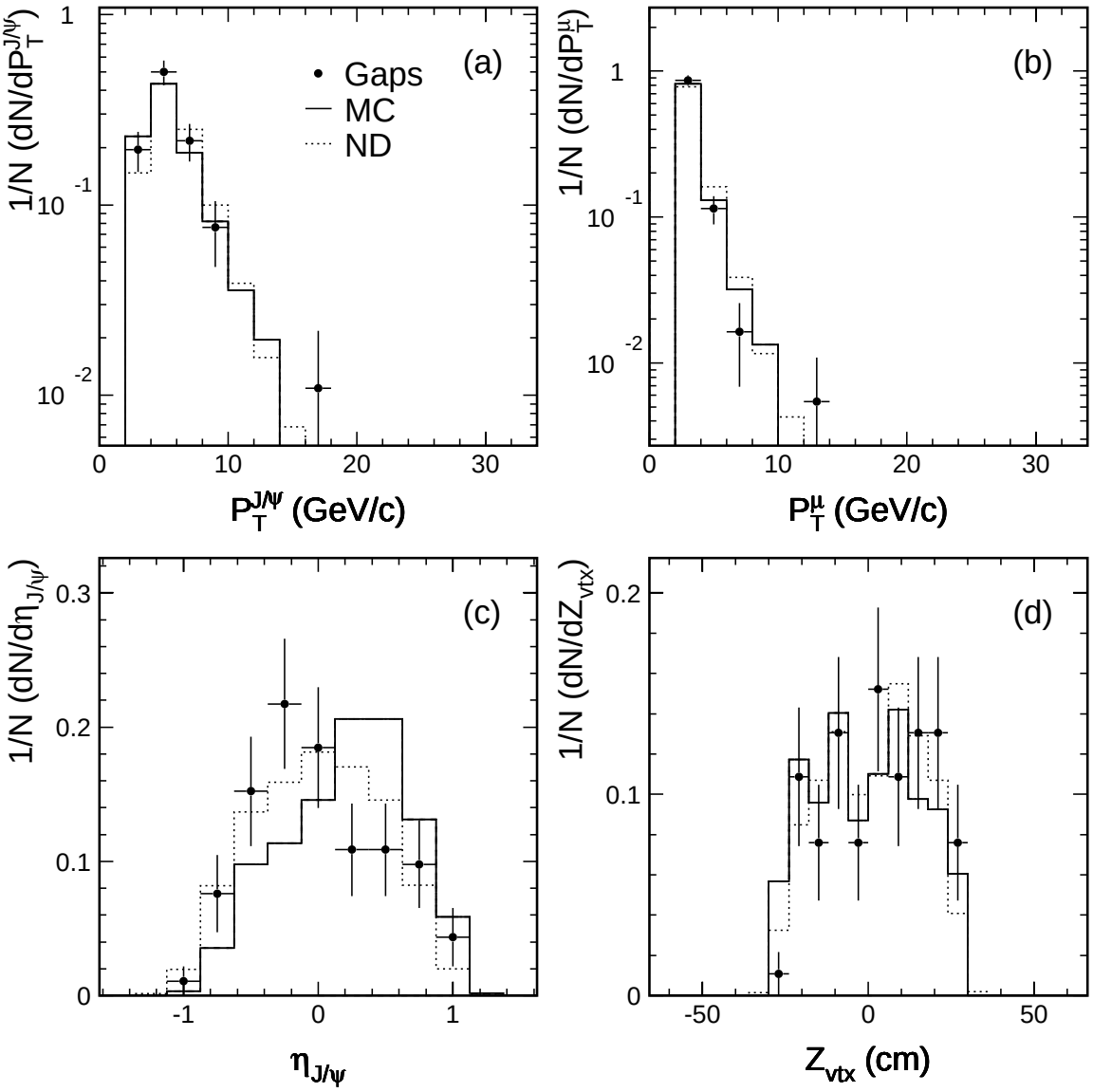

Figure 7.5: *(a) J/ψ and (b) muon transverse momentum, J/ψ (c) pseudo-rapidity and (d) vertex z-position of diffractive (points) and non-diffractive (dotted histogram) candidate events compared with the prediction of POMPYT based on the modified PYTHIA Monte Carlo (solid histogram) using a $1/\beta$ diffractive structure function.*

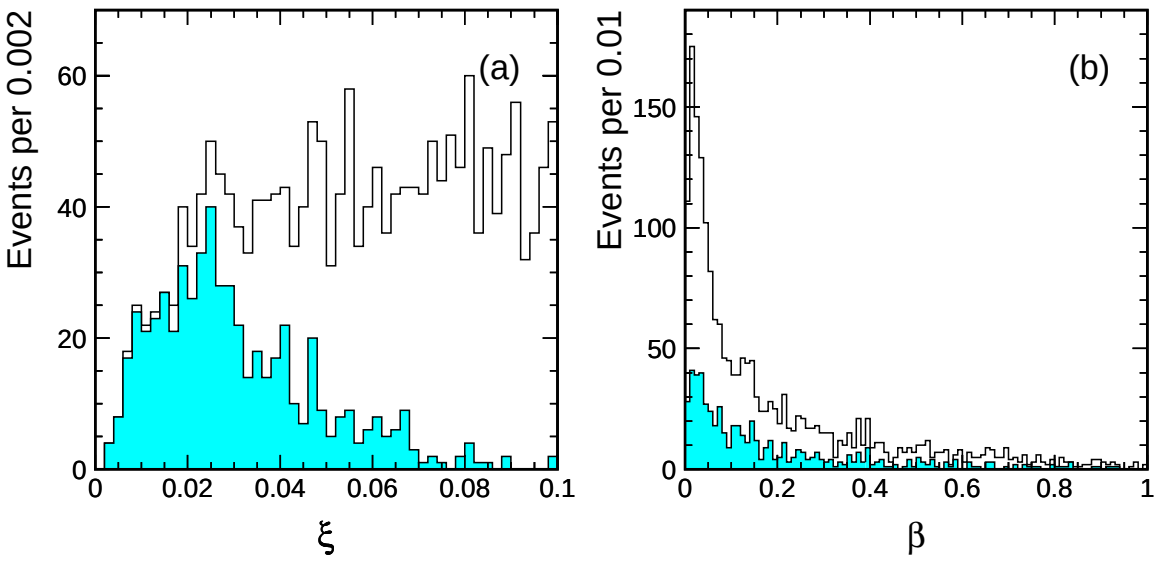

Figure 7.6: *(a) ξ and (b) β distributions for diffractive J/ψ events generated with POMPYT based on the modified PYTHIA using a $1/\beta$ pomeron structure function. The shaded histograms are for the events with a rapidity gap in the forward detectors ($N_{\rm BBC} = N_{\rm CAL} = 0$).*

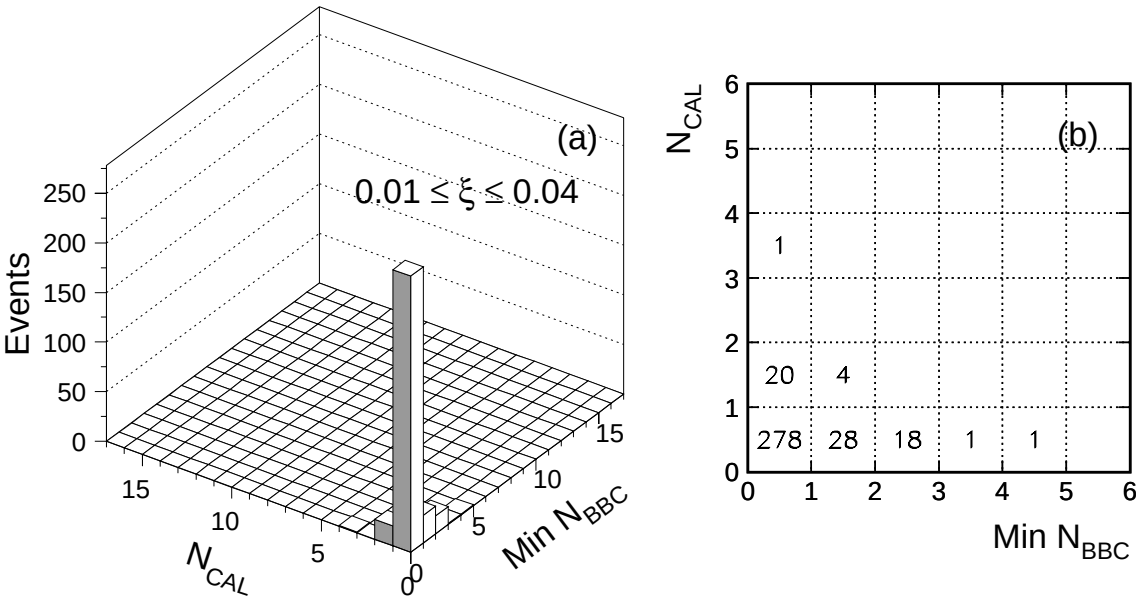

Figure 7.7: *Multiplicity of calorimeter towers versus minimum BBC hit multiplicity for diffractive Monte Carlo generated J/ψ events within the range $0.01 \leq \xi \leq 0.03$.*

Chapter 8

Gluon Fraction of Diffractive Structure

8.1 Analysis of $J/\psi + jet$ Events

Our analysis of diffractive J/ψ production was extended to study events in which one or more jets are reconstructed in addition to the J/ψ candidate.

8.1.1 Jet Clustering Algorithm

Experimentally, jets are detected as energy deposition in localized groups of calorimeter cells, energy *clusters*. CDF reconstructs jets using a fixed-cone clustering algorithm which consists of the following steps:

1. A list of seed calorimeter towers with $E_T > 1.0$ GeV is created.

2. Preclusters are formed from a continuous set of adjacent seed towers; if a tower is outside a window of 3×3 towers surrounding the seed, it is used to form a new precluster.

3. Clusters are built from preclusters by considering all the towers in a cone of radius $R = 0.7$ in $\eta - \phi$ space centered on the precluster. All towers with $E_T \geq 0.1$ GeV within the cone are included and the E_T-weighted centroid of the cluster is calculated.

4. The cluster is repositioned on the centroid. Around the centroid, towers within the new cone of 0.7 are included in reclustering and a new centroid is calculated. This procedure is repeated until the set of towers contributing to the jet remains unchanged.

5. Overlapping jets are merged if they share $\geq 75\%$ of the smaller jet's energy. If they share less, the towers in the overlap region are divided between the two clusters according to their proximity to the cluster centroid. After this division, the centroids are recalculated and the towers in the original overlap region are redivided based on their distance from the new centroids. This procedure iterates until a stable configuration is reached.

8.1.2 Jets in the J/ψ Sample

Since the mean value of the J/ψ transverse momentum is ~ 6 GeV/c, the reconstructed leading jet, which balances the J/ψ, is expected to have E_T in the range 4-8 GeV.

The low P_T muons from J/ψ decay are close to each other in η-ϕ space and deposit a significant portion of their energy in the calorimeter, so that in a J/ψ event the calorimeter cluster from muon hits may be misidentified as a jet. Figure 8.1 shows the distribution of energy deposited in the central calorimeter by muons from candidate J/ψ decays. The average energy deposition in the electromagnetic calorimeter

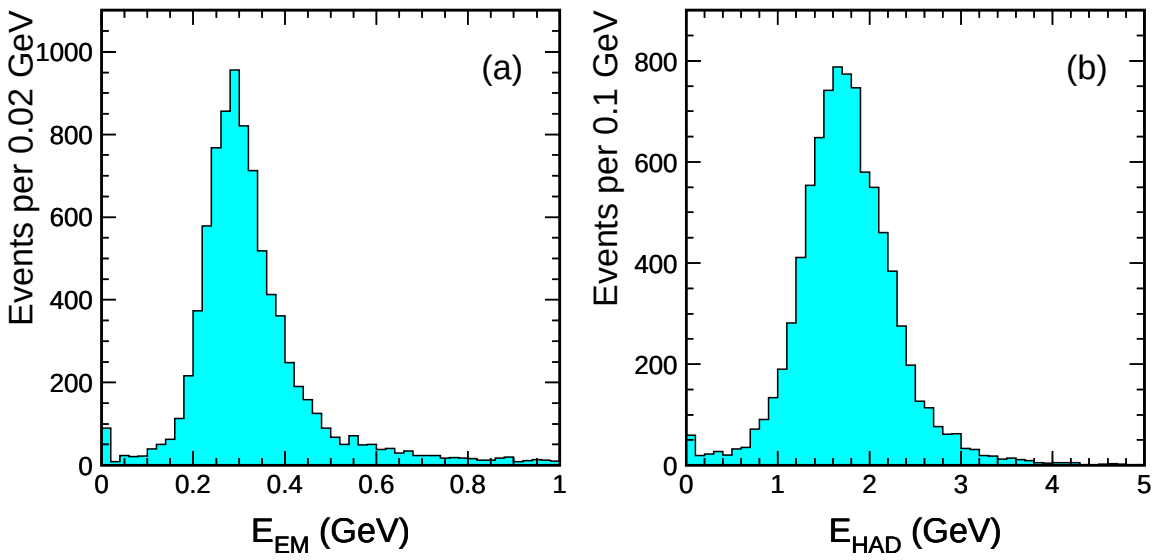

Figure 8.1: *Energy deposited in central electromagnetic (a) and hadronic (b) calorimeter by muons from J/ψ dimuon candidates.*

is 0.35 GeV and in the hadronic calorimeter 2.0 GeV.

Figure 8.2 shows the distribution of the distance in η-ϕ space, ΔR, between the muon calorimeter tower and the leading calorimeter cluster for different leading cluster energy thresholds. The peak at low ΔR is associated with the muon calorimeter cluster. The second peak on the plot for $E_T^{\rm 1clst} > 4$ GeV is associated with the second muon calorimeter cluster, as can be deduced from Fig. 8.3a which shows the distance between muon calorimeter towers. To exclude from consideration the calorimeter cluster due to the second muon, an isolation requirement of $\Delta R > 0.4$ around the second muon was applied. The ΔR distribution after the isolation cut, presented in Fig. 8.3c, shows no longer a leading jet peak at the vicinity of $\Delta R \approx 1$, where the second muon would be expected.

To avoid confusing a jet with a muon calorimeter cluster the distance in η-ϕ between the leading calorimeter cluster and each muon is required to be greater than

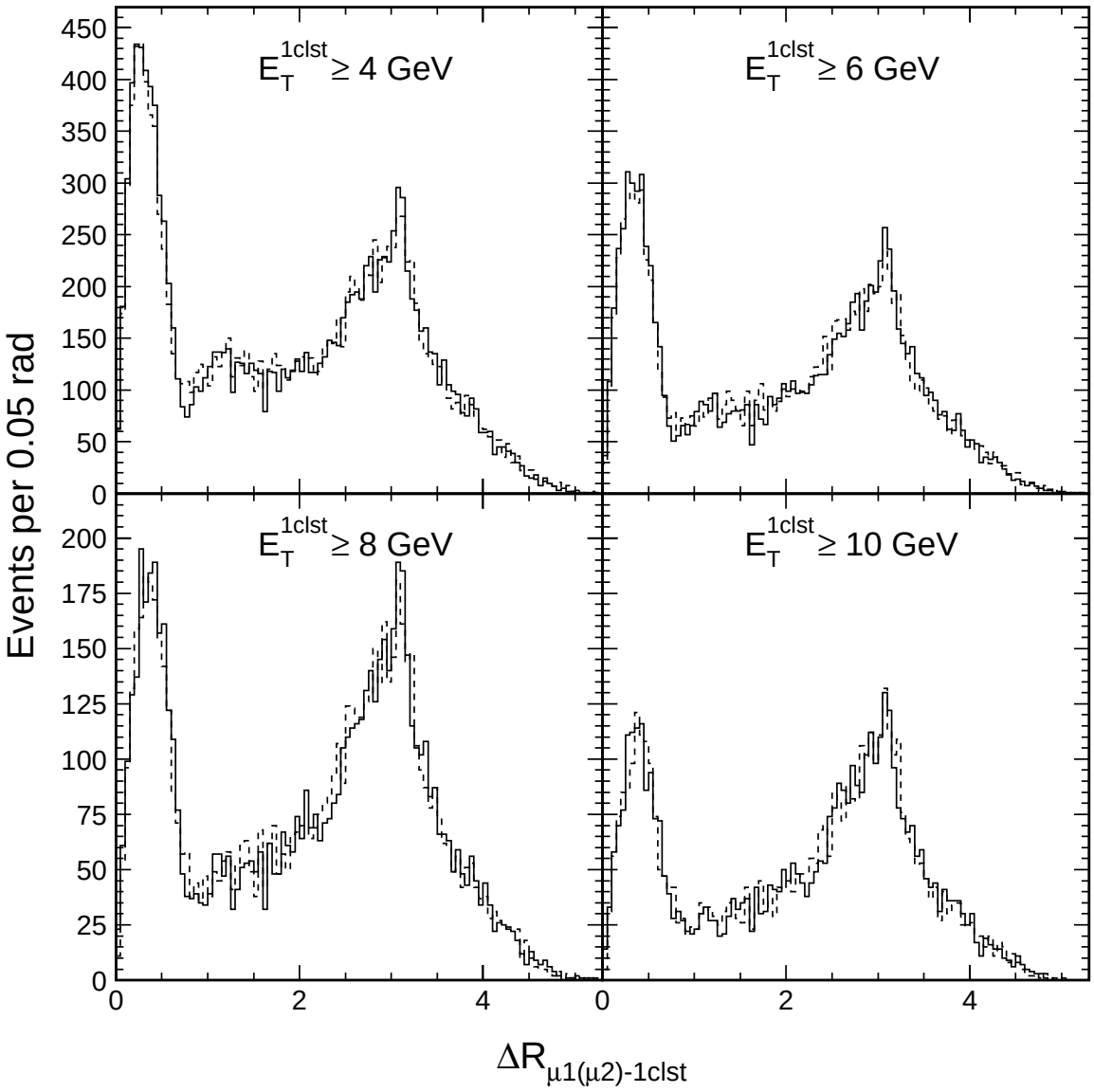

Figure 8.2: *Distance ΔR between muon calorimeter tower and highest energy calorimeter cluster in $\eta - \phi$ space for different cluster energy thresholds.*

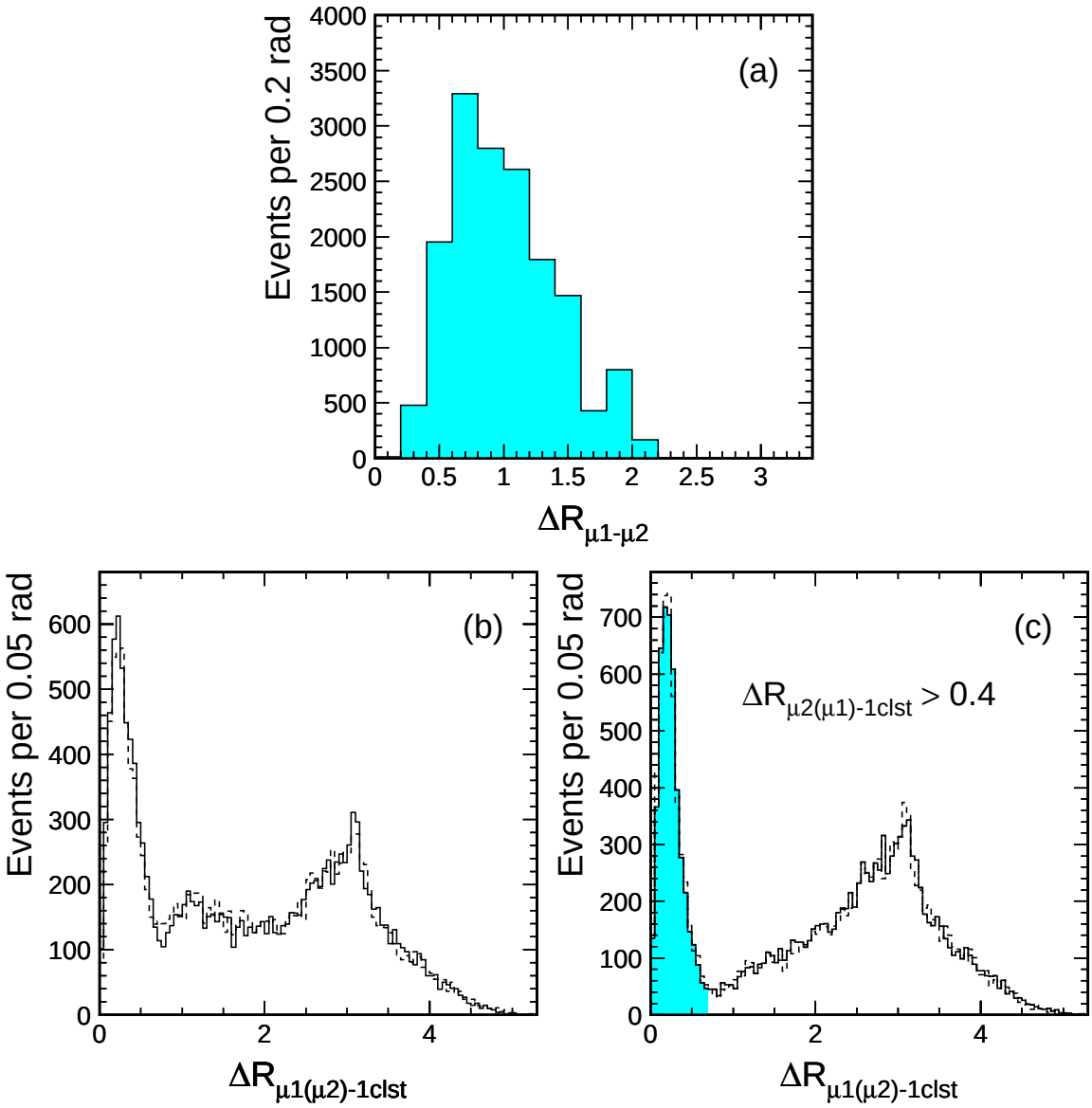

Figure 8.3: *Distance in $\eta-\phi$ space between (a) muon calorimeter towers, (b) muon calorimeter tower and highest energy cluster and (c) the same distribution as (b) after excluding the calorimeter cluster within $\Delta R = 0.4$ around the second muon (shaded histogram indicates events removed by the cut $\Delta R_{\mu-1\mathrm{clst}} > 0.7$).*

0.7. Since our diffractive J/ψ events have a rapidity gap in the region $2.4 \leq |\eta| \leq 5.9$, the core of the reconstructed jet for non-diffractive events is restricted to the region $|\eta| < 1.7$. The number of J/ψ events passing the above jet requirements is 8732.

8.2 Fraction of Diffractive $J/\psi + jet$ Events

The ratio of diffractive to non-diffractive $J/\psi + jet$ events is measured using the method for extracting the diffractive event signal described in sections 6.3 - 6.8. Figure 8.4 shows the forward calorimeter tower multiplicity versus BBC hits for the η-side of the detector with minimum BBC hit multiplicity(top plots) and for the η-side with maximum BBC multiplicity(bottom plots).

Multiplicity	N_{events}	$N(\text{non}-J/\psi)$	$N(J/\psi)$
0	44	2.2 ± 0.8	41.8 ± 6.7
1	10	0.2 ± 0.2	9.8 ± 3.2
2	11	0.6 ± 0.4	10.4 ± 3.3
3	15	0.6 ± 0.4	14.4 ± 3.9
4	12	0.6 ± 0.4	11.4 ± 3.5
5	19	1.3 ± 0.7	17.7 ± 4.4
6	23	1.8 ± 0.7	21.2 ± 4.9
7	23	0.7 ± 0.5	22.3 ± 4.8
8	17	0.3 ± 0.3	16.7 ± 4.1
9	28	0.7 ± 0.5	27.3 ± 5.3
10	19	1.2 ± 0.6	17.8 ± 4.4
11	23	1.8 ± 0.8	21.2 ± 4.9
12	33	3.9 ± 1.1	29.1 ± 5.8
Full sample	8732	591 ± 31	8141 ± 98

Table 8.1: *Results of fits of the dimuon invariant mass distribution as a function of calorimeter tower and BBC multiplicity for $J/\psi + jet$ candidate events for which the two multiplicities are equal.*

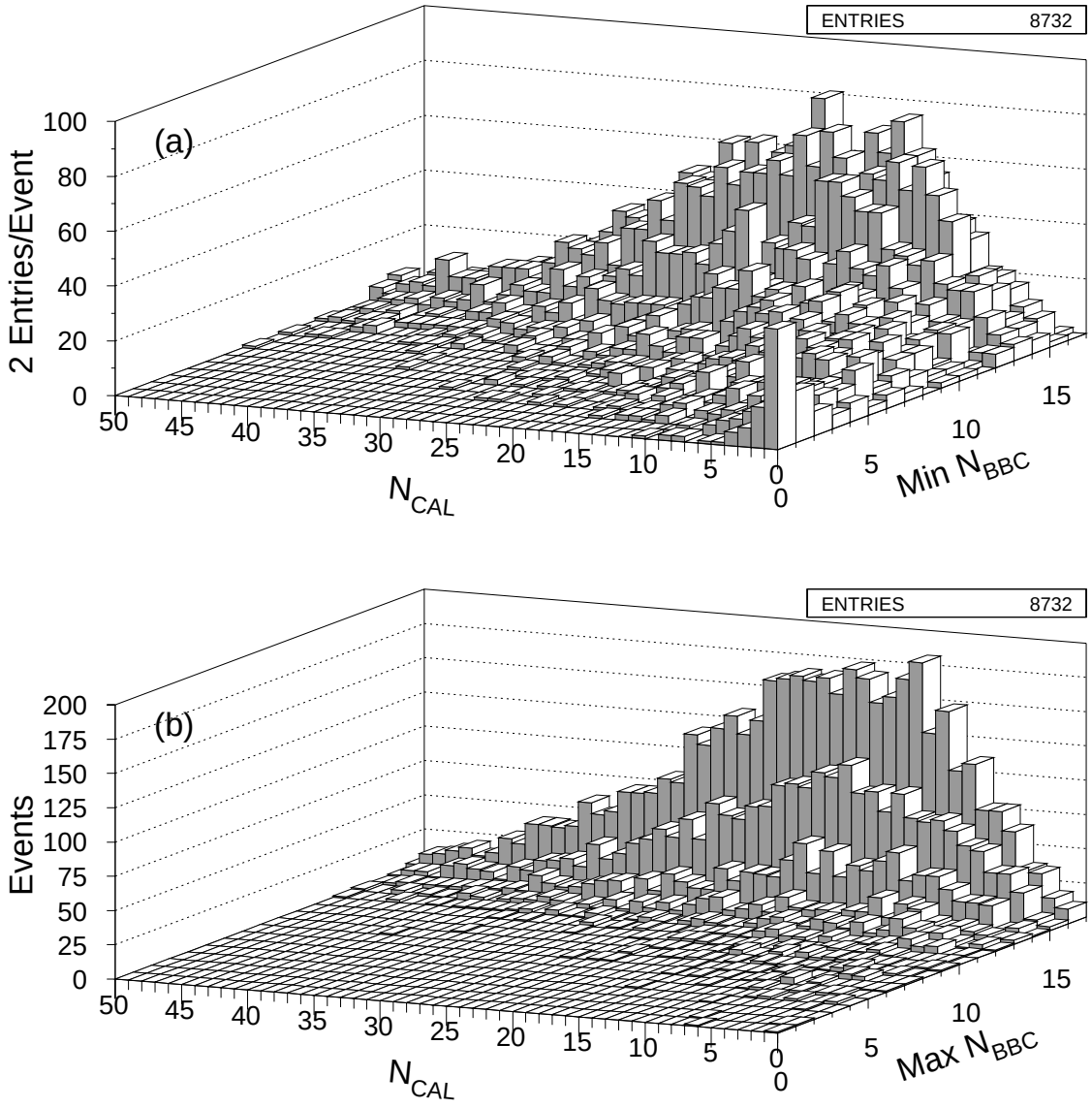

Figure 8.4: *(a) Multiplicity in calorimeter towers with* $2.4 < |\eta| < 4.2$ *versus BBC hit multiplicity on the* η*-side of the detector with minimum BBC multiplicity for the* $J/\psi + jet$ *sample; (b) BBC hits versus calorimeter tower multiplicity only for the side of the detector with maximum BBC hit multiplicity.*

As previously, the non-J/ψ background in the diagonal bins of the 2-dimensional multiplicity distribution is obtained by fitting the dimuon invariant mass distribution to a sum of a gaussian and a constant function. Table 8.1 summarizes the results of the fits for events with the same BBC hit multiplicity and forward calorimeter tower multiplicity (diagonal bins). The dimuon mass distribution of the total $J/\psi + jet$ sample is fitted to the sum of two gaussian and a linear function (last line in Tab. 8.1).

Figure 8.5 shows the multiplicity distribution of the diagonal bins ($N = N_{\rm BBC} = N_{\rm CAL}$) after non-$J/\psi$ background subtraction. The diffractive signal is estimated by linearly extrapolating the fit from bins $2-12$ to bin 0. The number of diffractive $J/\psi + jet$ events in the (0,0) bin ($N_{\rm BBC} = N_{\rm CAL} = 0$) is found to be

$$N^{(0,0)}_{{\rm SD}\psi+jet} = (41.8 \pm 6.7) - (8.7 \pm 2.8) = 33.1 \pm 7.3$$

Correction Factor	Value	Uncertainty
$\varepsilon^{\rm ND}_{\rm 1vtx}$	0.552	± 0.038
$\varepsilon^{\rm SD}_{\rm 1vtx}$	0.85	± 0.05
$\varepsilon_{\rm Live}$	0.80	± 0.03

Table 8.2: *Correction factors for the ratio of diffractive to non-diffractive $J/\psi + jet$ events.*

All necessary correction factors for calculating the ratio of diffractive to non-diffractive $J/\psi + jet$ events are given in Table 8.2. The measured ratio of diffractive to non-diffractive $J/\psi + jet$ events after corrections is given by

$$\begin{aligned} R_{J/\psi+jet} \times \mathcal{A}_{\rm gap} &= \frac{33.1 \pm 7.3}{8139 \pm 98} \times \frac{0.552 \pm 0.038}{0.85 \pm 0.05} \times \frac{1}{0.80 \pm 0.03} \\ &= [0.33 \pm 0.07({\rm stat}) \pm 0.03({\rm syst})]\%. \end{aligned} \tag{8.1}$$

Figures 8.6, 8.7 and 8.8 show distributions of the J/ψ p_T, the p_T of the four highest energy jets in a J/ψ event, and the azimuthal angle difference between

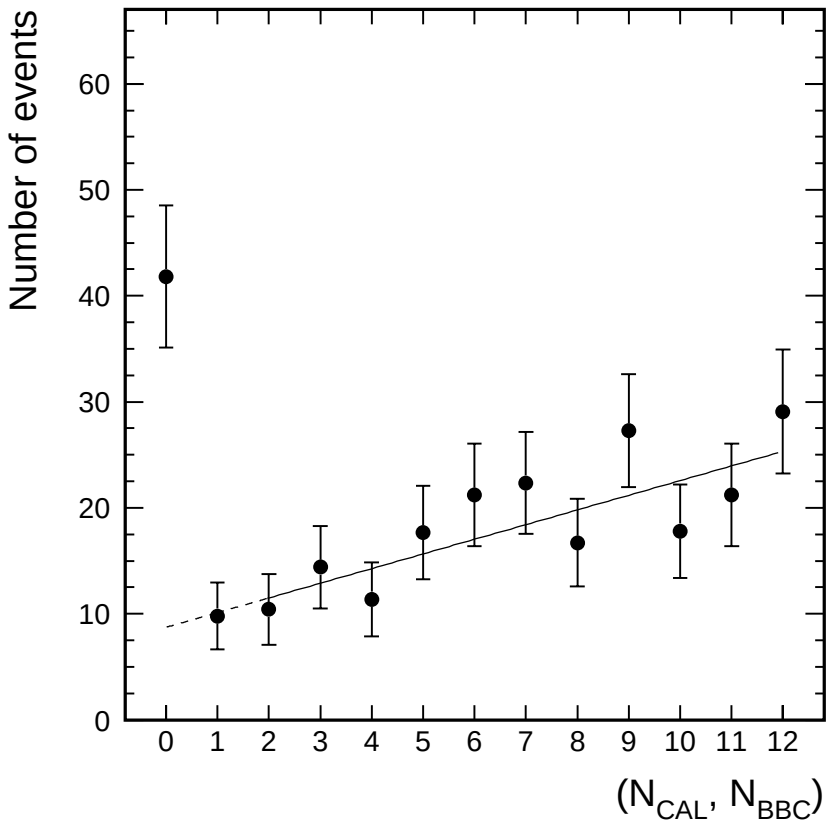

Figure 8.5: *J/ψ event counts in bins of equal BBC and calorimeter multiplicity (for $2.4 < |\eta| < 4.2$) as a function of multiplicity $N = N_{\mathrm{CAL}} = N_{\mathrm{BBC}}$.*

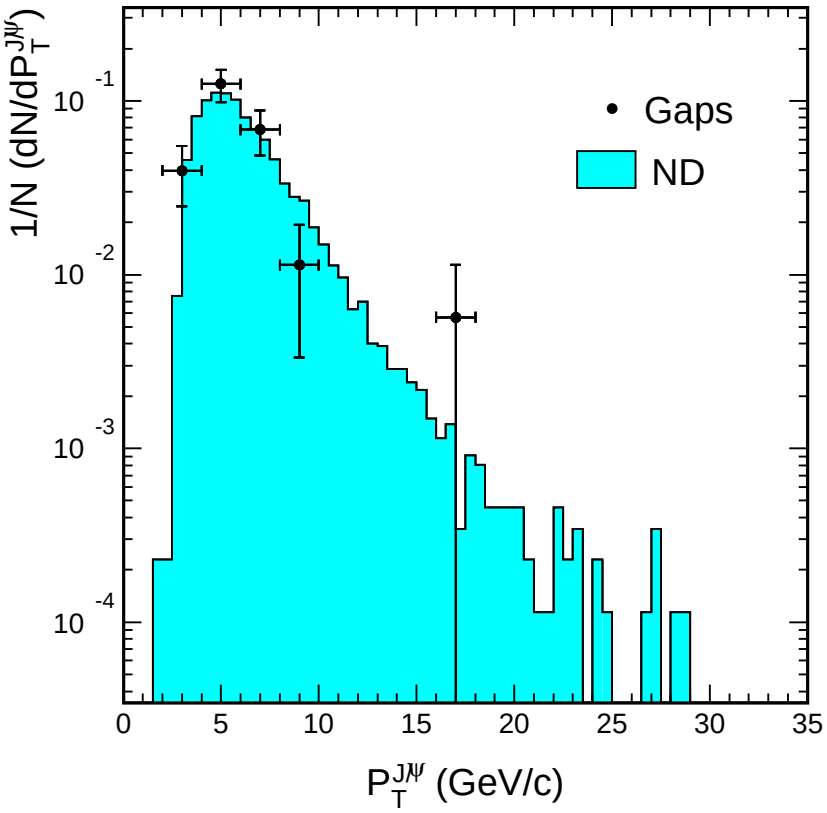

Figure 8.6: *J/ψ transverse momentum for J/ψ + jet sample.*

the J/ψ and the leading jet, respectively, for single diffractive (SD) candidates and non-diffractive (ND) sample.

8.3 Measurement of ξ

The variable ξ is related to the mass M_X of the diffractive state X by

$$\xi = \frac{M_X^2}{s} \tag{8.2}$$

The mass squared of the diffractive state X is given by

$$M_X^2 = (\sum_i E_i)^2 - (\sum_i \vec{P}_i)^2 = (\sum E_T e^{+\eta}) \cdot (\sum E_T e^{-\eta}) \tag{8.3}$$

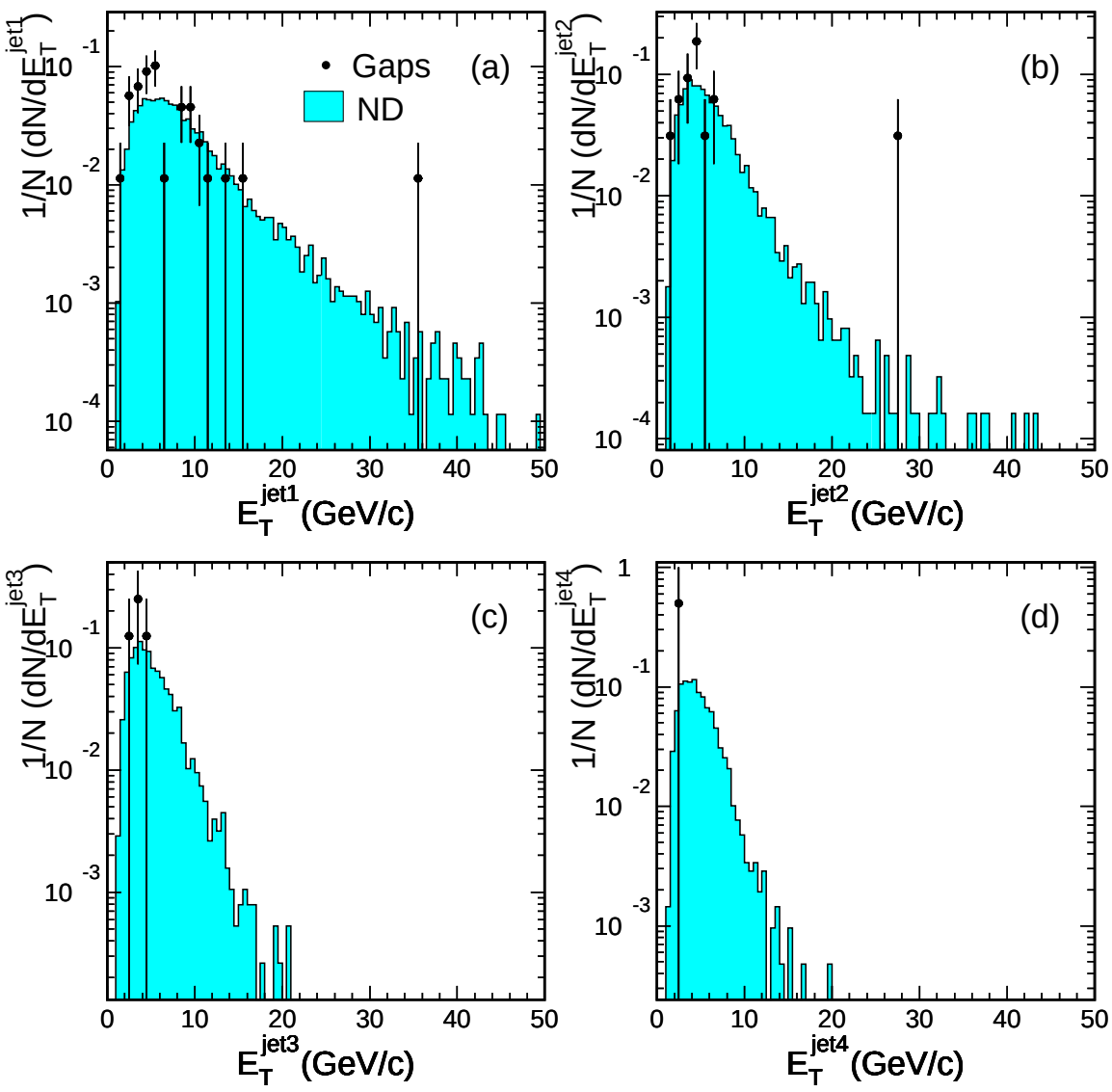

Figure 8.7: *Transverse momentum of the four highest energy jets in a J/ψ event.*

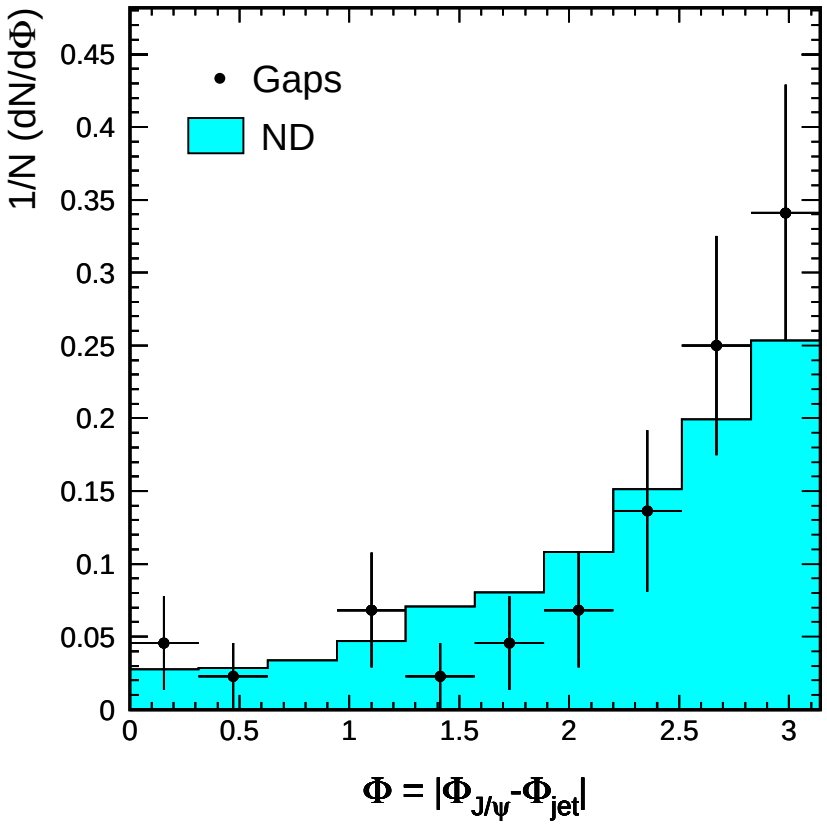

Figure 8.8: *Azimuthal angle difference between J/ψ and leading jet.*

where the sum is taken over all particles in the final state X excluding the leading (anti)proton. Including the $\bar{p}$, each sum in the product is equal to $\sqrt{s}$. For single diffractive events with a rapidity gap on the negative η side, the leading antiproton escapes the detector system along the negative z direction. Since the rapidity of the leading antiproton has a large negative value, the first factor of the product in Eq. 8.3 can still be approximated by $\sqrt{s}$, even when the $\bar{p}$ is excluded. Hence, the value of ξ for single diffractive events with a rapidity gap at negative η is

$$\xi = \frac{\sqrt{s} \cdot \sum E_T e^{-\eta}}{s} = \frac{\sum E_T e^{-\eta}}{\sqrt{s}} \tag{8.4}$$

A similar formula can be written for single diffractive events with a rapidity gap at positive η,

$$\xi = \frac{\sum E_T e^{+\eta}}{\sqrt{s}} \tag{8.5}$$

The value of ξ in Eq. 8.4 is dominated by particles which are close to the edge of the rapidity gap and are in the region of the CDF detector coverage; the contribution of particles which escape down the beam pipe at large positive η is very small and can be neglected. The value of ξ measured from the particles within the range of CDF detectors should therefore be a good approximation to the true value of ξ [68].

In evaluation of ξ, all towers with energy above the threshold specified in Table 6.1 are considered, the tower E_T is multiplied by the correction factor of 1.6, and the sum $E_T^i e^{-\eta_i}$ is calculated. In this sum, the terms $E_T^{jet} e^{-\eta_{jet}}$ for the 4 leading jets in the event are included instead of the terms for calorimeter towers inside the cones of these jets. To account for particles in the BBC coverage region, it is assumed that a BBC hit is due to a particle of $E_T = 0.5$ GeV and η the central value of the BBC being hit, and a term $E_T^i e^{-\eta_i}$ for each BBC hit is added to the sum. To take into account the neutral particles hitting BBC, the obtained BBC part of the sum is

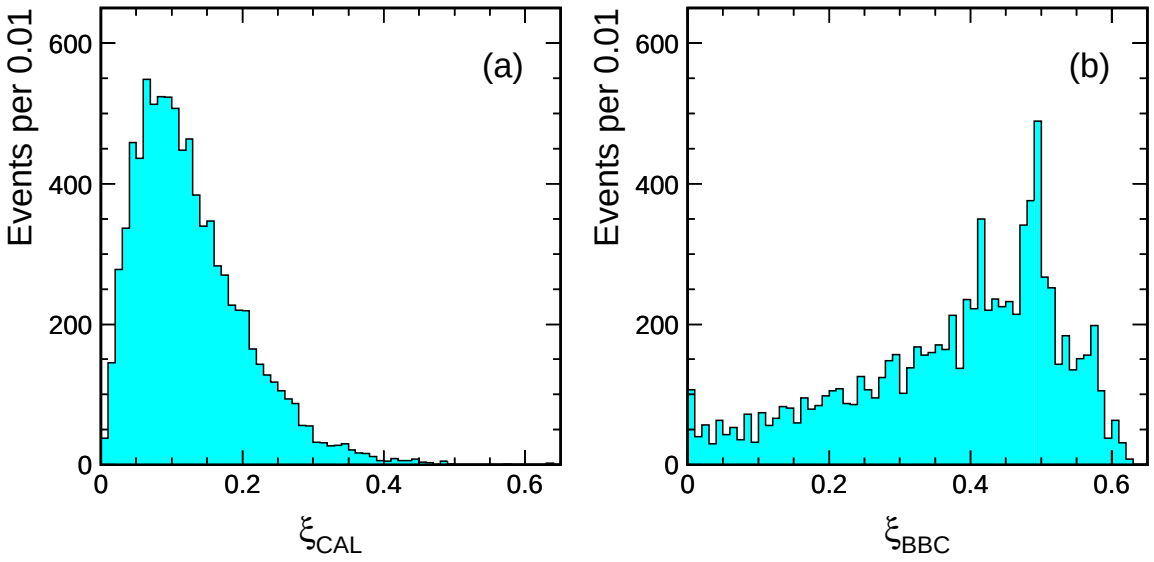

Figure 8.9: *(a) The calorimeter contribution, $\xi_{\rm CAL}$, and (b) the BBC contribution, $\xi_{\rm BBC}$, to the reconstructed ξ (uncorrected) for all J/ψ + jet candidates.*

multiplied by a factor of 1.5. Since the beam-beam counters overlap in 1/3 of the BBC coverage region, a correction factor of 3/4 is applied. The forward calorimeter and BBCs overlap by about one unit of pseudorapidity. To account for this, the number of forward calorimeter towers above noise level in the overlap region is divided by two, since one BBC hit on average corresponds to two forward calorimeter towers, and subtracted from the number of BBC hits in the outer BBC layers

Figure 8.9 shows the calorimeter contribution to the reconstructed ξ (uncorrected) for all J/ψ candidates, and the BBC contribution, $\xi_{\rm BBC}$. Figure 8.10 shows the distribution of the reconstructed ξ multiplied by 1.7, the correction factor for rapidity gap events found in the analysis presented in [26]. The bottom plot in Fig. 8.10 shows an expanded view of the low $\xi_{\rm corr}$ range, where the shaded histogram is for the diffractive J/ψ events with $N_{\rm BBC} = N_{\rm CAL} = 0$.

In our further analysis only diffractive candidate events from the region $0.01 \leq \xi_{\rm corr} \leq 0.03$ are used. The excess of events of the ξ distribution of the inclusive

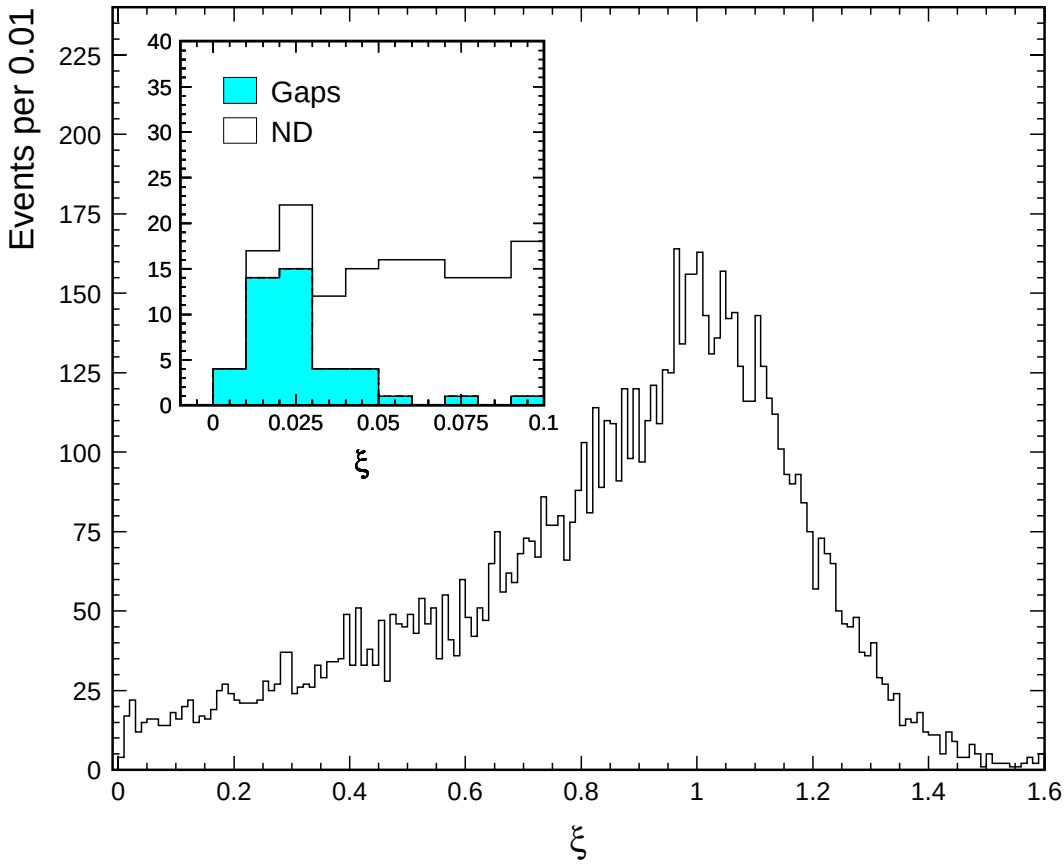

Figure 8.10: *Reconstructed ξ multiplied by 1.7 (correction factor for rapidity gap events) for all $J/\psi + jet$ candidates. Insertion shows expanded view of low ξ region (shaded histogram for diffractive $J/\psi + jet$ events with $N_{\mathrm{BBC}} = N_{\mathrm{CAL}} = 0$).*

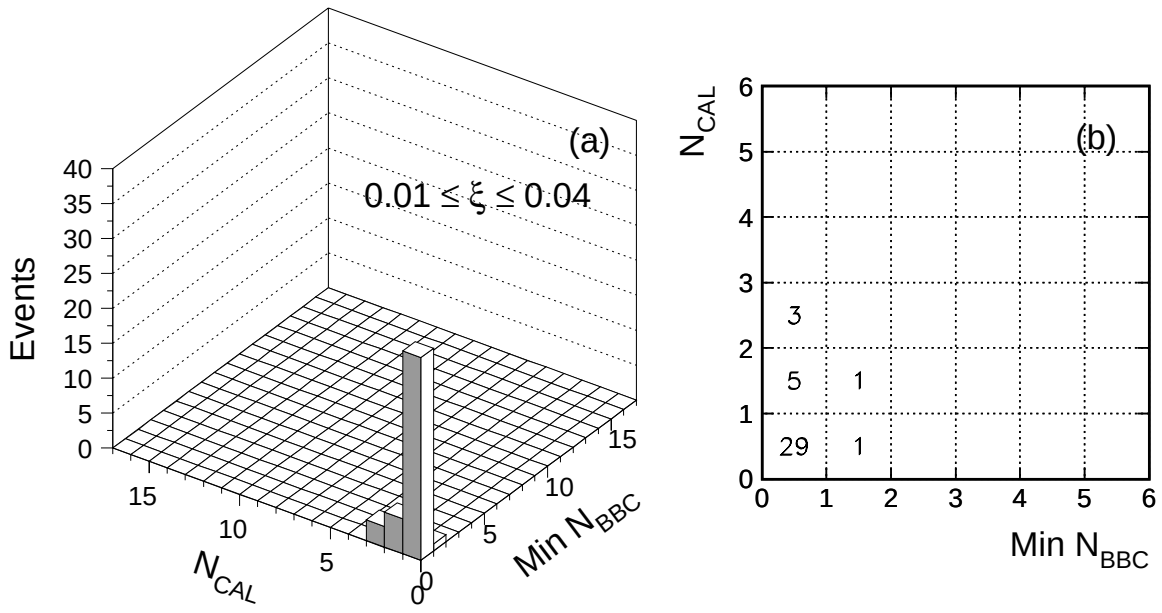

Figure 8.11: *Multiplicity of calorimeter towers versus minimum BBC hit multiplicity for diffractive J/ψ + jet candidates within the range* $0.01 \leq \xi \leq 0.03$.

event sample in this region is partly due to leakage of some diffractive signal from the (0,0) bin to higher multiplicity bins, and partly due to non-diffractive events with ξ values in this ξ range. Assuming that one half of the excess is due to leakage of diffractive events and assigning to it an uncertainty of $\pm 100\%$, we find the gap acceptance of the (0,0) bin for diffractive events with ξ in the region $0.01 \leq \xi_{\rm corr} \leq 0.03$

$$A^{\xi}_{\rm gap} = 0.87 \pm 0.13$$

Figure 8.11 shows the BBC versus calorimeter tower multiplicity for the events of the inclusive sample within $0.01 \leq \xi_{\rm corr} \leq 0.03$. As discussed in Section 7.1, the Monte Carlo simulation showed that the multiplicity bins with $N_{\rm BBC} + N_{\rm CAL} \geq 2$ are dominated by non-diffractive events. In the present case, the number of events in these bins is 4, which is consistent with one half of the excess of 10 events.

The sample of events in the (0,0) bin contains 21% of non-diffractive back-

ground (see Section 8.2). Therefore, to obtain the number of diffractive events in the region $0.01 \leq \xi_{\rm corr} \leq 0.03$ the total number of gap events in this region has to be multiplied by the fraction of diffractive events, $f_{\rm SD} = 0.79 \pm 0.06$, and divided by the gap acceptance, $A^{\xi}_{\rm gap}$.

8.4 Study of Bjorken-x Distribution

For $\bar{p}p \to J/\psi + jet + X$, the x-Bjorken of the struck parton in the (anti)proton is given by

$$x_{\rm bj} = p_{g,q}/p_{p(\bar{p})} \simeq \frac{P_T^{J/\psi} \cdot e^{\pm\eta_{J/\psi}} + E_T^{jet} \cdot e^{\pm\eta_{jet}}}{2 \cdot p_0^{p(\bar{p})}} \tag{8.6}$$

where the $+(-)$ sign in the exponent is for the $x_{\bar{p}}$ (x_p). Here we will be concerned with the $x_{\rm bj}$ of the parton in the diffracted nucleon "attached" to the rapidity gap. The leading jet E_T distribution in our sample is dominated by low E_T jets in the region 3-7 GeV. The jet E_T correction (JTC96X) for such low E_T jets is not reliable. Since the E_T^{jet} of the leading jet is expected to be balanced by the $E_T^{J/\psi}$ of the J/ψ, the $P_T^{J/\psi}$ is used instead of E_T^{jet} in the calculation of the $x_{\rm bj}$:

$$x_{\rm bj} \simeq \frac{P_T^{J/\psi} \cdot \left(e^{\pm\eta_{J/\psi}} + e^{\pm\eta_{jet}}\right)}{\sqrt{s}} \tag{8.7}$$

Figure 8.12 shows the $x_{\rm bj}$ distribution for rapidity gap events (Fig. 8.12a) in the region $0.01 \leq \xi_{\rm corr} \leq 0.03$ and for non-diffractive events (Fig. 8.12b). The solid histograms were obtained with $x_{\rm bj}$ calculated using $E_T^{J/\psi}$ for the leading jet E_T, and the dashed histograms using the corrected E_T^{jet}. The two distributions are in reasonable agreement.

From the $x_{\rm bj}$ distributions for diffractive and non-diffractive events, we ob-

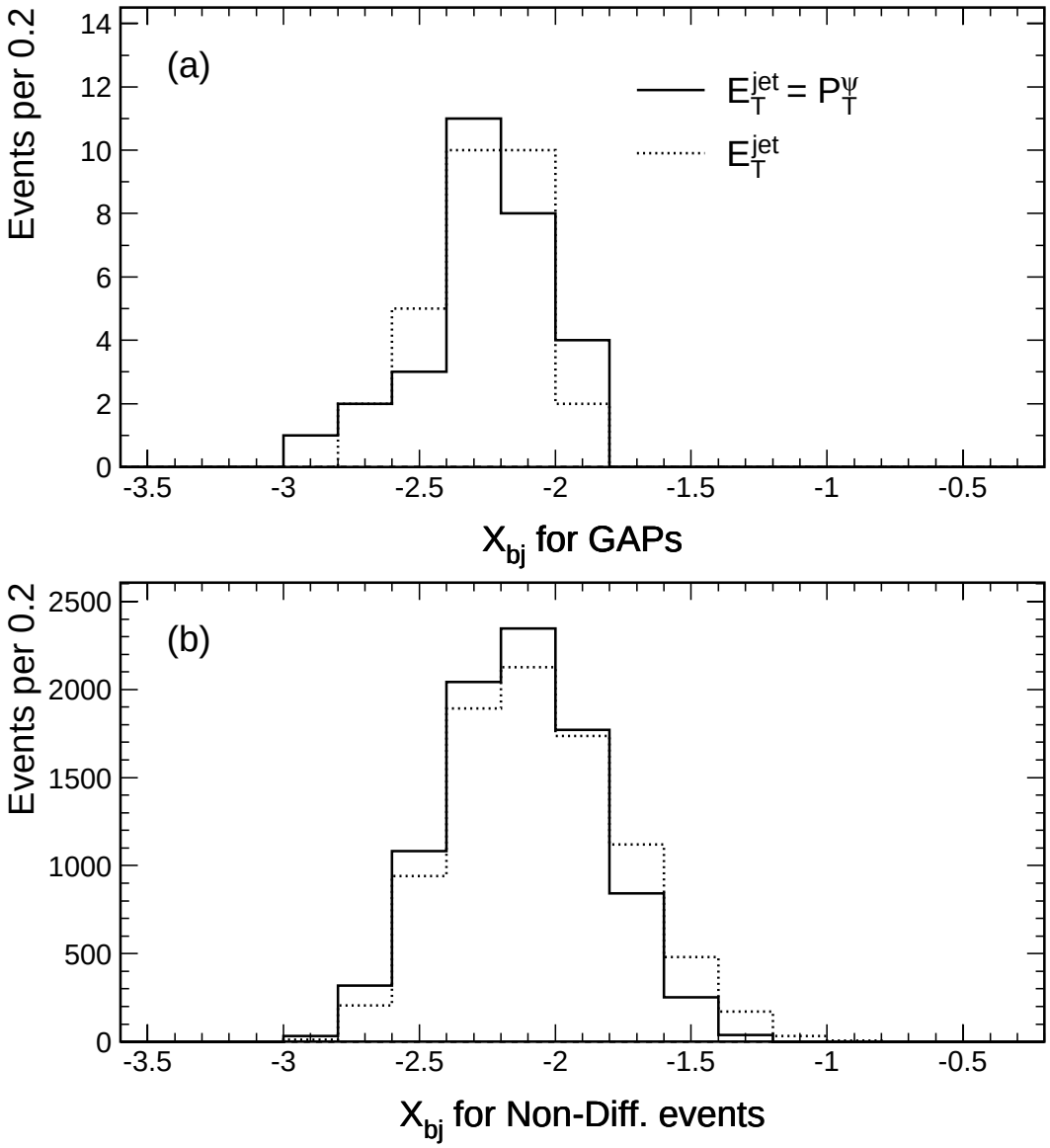

Figure 8.12: $x_{\rm bj}$ *distribution for diffractive* J/ψ *candidates in the region* $0.01 \leq \xi_{\rm corr} \leq 0.03$ *(a) and non-diffractive events (b).*

tain the $x_{\rm bj}$ distribution for the diffractive to non-diffractive event ratio,

$$R_{J/\psi}(x_{\rm bj}) = \frac{N^{\rm SD}_{J/\psi}(x_{\rm bj})}{N^{\rm ND}_{J/\psi}(x_{\rm bj})}$$

This ratio may be expressed in terms of cross sections per unit ξ by applying the correction

$$A_{\rm corr} = \frac{1}{\Delta\xi_{\rm corr}} \times \frac{f_{\rm SD}}{A^{\xi}_{\rm gap}} \times \frac{\varepsilon^{\rm ND}_{\rm 1vtx}}{\varepsilon^{\rm SD}_{\rm 1vtx}} \times \frac{1}{\varepsilon_{\rm Live}} \tag{8.8}$$

where $\Delta\xi_{\rm corr}$ is the width of the ξ range, $0.01 \leq \xi_{\rm corr} \leq 0.03$, $A^{\xi}_{\rm gap}$ the gap acceptance, and $f_{\rm SD}$ the diffractive fraction in the (0,0) bin. The values of the correction factors are listed in Table 8.3.

Correction Factor	Value	Uncertainty
$A^{\xi}_{\rm gap}$	0.79	–
$f_{\rm SD}$	0.79	$\pm$0.06
$\varepsilon^{\rm ND}_{\rm 1vtx}$	0.552	$\pm$0.038
$\varepsilon^{\rm SD}_{\rm 1vtx}$	0.85	–
$\varepsilon_{\rm Live}$	0.80	$\pm$0.03
$\Delta\xi_{\rm corr}$	0.02	–

Table 8.3: *Correction factors used in the calculation of* $R_{J/\psi}(x_{\rm bj})$.

The corrected ratio $R_{J/\psi}$ must be divided by 2 before comparing it with the ratio R_{jj} obtained from the analysis of dijets with a leading antiproton, since in the J/ψ case gaps both in the positive and negative pseudorapidity regions are considered. The two ratios are compared in Fig. 8.13. The vertical dashed lines denote the boundaries of the *kinematically safe* region for the $J/\psi + jet$ events, $0.004 \leq x_{\rm bj} \leq 0.01$. The upper bound corresponds to $\xi_{\rm min}$ of the diffractive sample and ensures that all ξ values from the region $0.01 \leq \xi_{\rm corr} \leq 0.03$ contribute to the $x_{\rm bj}$ distribution, while the lower bound, $x_{\rm min}$, is imposed to guard against detector edge effects. The two distributions exhibit similar behavior.

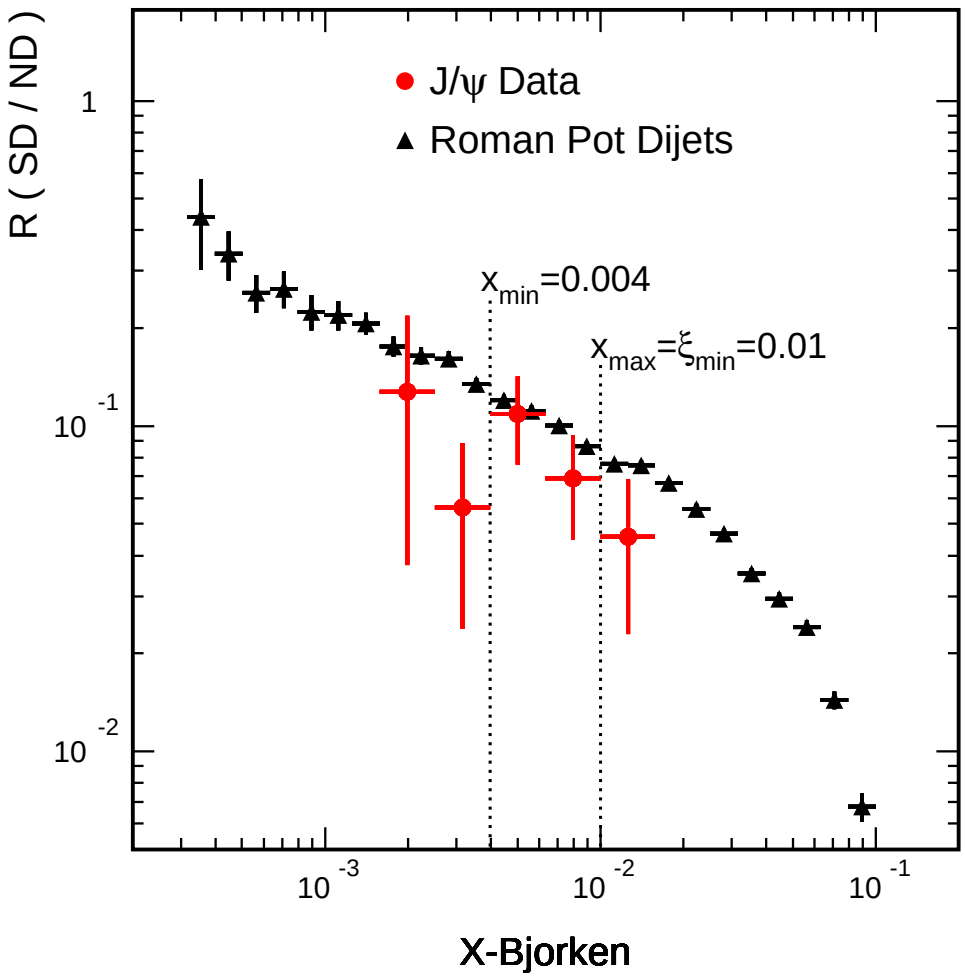

Figure 8.13: *Ratios of diffractive to non-diffractive J/ψ (circles) and dijet (triangles) rates per unit $\xi_p(\xi_{\bar{p}})$ as a function of x-Bjorken of the struck parton of the $p(\bar{p})$ adjacent to the rapidity gap.*

8.5 Gluon Fraction of Diffractive Structure Function

In LO QCD, the ratio of diffractive to non-diffractive dijet production as a function of Bjorken x is equal to the ratio of the diffractive to non-diffractive structure functions of the proton:

$$R_{jj}(x) = \frac{F_{jj}^D(x)}{F_{jj}(x)} \tag{8.9}$$

Since $F_{jj}(x) \sim g(x) + \frac{4}{9}q(x)$, where $g(x)$ and $q(x)$ are the gluon and quark fractions in the proton, respectively, Eq. 8.9 can be written as

$$R_{jj}(x) = \frac{g^D(x) + \frac{4}{9}q^D(x)}{g(x) + \frac{4}{9}q(x)} = \frac{g^D(x)}{g(x)} \times \frac{1 + \frac{4}{9}\frac{q^D(x)}{g^D(x)}}{1 + \frac{4}{9}\frac{q(x)}{g(x)}} \tag{8.10}$$

where $g^D(x)$ and $q^D(x)$ denote the gluon and quark fraction of the diffracted proton structure function, $F_{jj}^D(x)$.

For J/ψ production, which is dominated by gg interactions, the ratio of diffractive to non-diffractive production can be written in terms of $g^D(x)$ and $g(x)$ as

$$R_{J/\psi}(x) \simeq \frac{g^D(x)}{g(x)} \tag{8.11}$$

From Eq. 8.10 then obtain

$$\frac{R_{jj}(x)}{R_{J/\psi}(x)} = \frac{1 + \frac{4}{9}\frac{q^D(x)}{g^D(x)}}{1 + \frac{4}{9}\frac{q(x)}{g(x)}} \tag{8.12}$$

Evaluating this ratio of ratios by integrating the $x_{\rm bj}$ distributions for R_{jj} and $R_{J/\psi}$ in the region $0.004 \leq x_{\rm bj} \leq 0.01$ yields

$$\left.\frac{R_{jj}(x)}{R_{J/\psi}(x)}\right|_{\rm exp} = 1.17 \pm 0.27({\rm stat})$$

Using this value in Eq. 8.12 and the ratio of $q(x)/g(x) = 0.274$ at $x = 0.0063$ and $Q = 6$ GeV calculated from the GRV98 LO PDF-set, the gluon fraction of the diffractive

structure function is found to be

$$f_g^D = 0.59 \pm 0.14(\text{stat}) \pm 0.06(\text{syst}) = 0.59 \pm 0.15$$

where the statistical uncertainty is based on the 19 rapidity gap events in the kinematical region $0.01 \leq \xi_{\text{corr}} \leq 0.03$, $0.004 \leq x_{\text{bj}} \leq 0.01$, and the systematic uncertainty includes in quadrature the uncertainties of the correction factors in Eq. 8.8. This gluon fraction is consistent with the value $0.54^{+0.16}_{-0.14}$ obtained by combining the results of diffractive W, dijet, and b-quark production [1].

Chapter 9

Results

The first observation of diffractive $J/\psi(\rightarrow \mu^+\mu^-)$ production in $\bar{p}p$ collisions at $\sqrt{s}$=1.8 TeV was presented using data collected from the Collider Detector at Fermilab (CDF). Diffractive events were identified by their rapidity gap signature.

In a sample of events with two muons of transverse momentum $P_T^{\mu} > 2$ GeV/c within the pseudorapidity region $|\eta|$ <1.0, the ratio of diffractive to total J/ψ production rates was found to be

$$R_{J/\psi} = (1.45 \pm 0.25)\%.$$

The ratio $R_{J/\psi}$ is larger than the corresponding ratio for diffractive b-quark production, $R_{b\bar{b}} = (0.62 \pm 0.25)\%$ [1], by a factor of 2.34 ± 0.35. Since both J/ψ and b-quark production are mainly sensitive to the gluon content of pomeron exchange, the difference in the two ratios must be attributed to the different average $x_{\rm bj}$ values of the two measurements, coupled with the $x_{\rm bj}^{-0.45}$ dependence of the diffractive structure function [22]. Thus, the double ratio $R_{b\bar{b}}^{J/\psi} \equiv R_{J/\psi}/R_{b\bar{b}}$ is expected to be equal to $(x_{\rm bj}^{J/\psi}/x_{\rm bj}^{b\bar{b}})^{-0.45}$. Since in these measurements we consider only central J/ψ or b-quark production, the ratio $x_{\rm bj}^{J/\psi}/x_{\rm bj}^{b\bar{b}}$ is approximately proportional to the ratio of the

corresponding average P_T values for each process, which is ≈ 6 GeV/c for the J/ψ and ≈ 36 GeV/c for the b-quark (three times the average P_T of the b-decay electron). The expected value for $R_{b\bar{b}}^{J/\psi}$ is then $R_{b\bar{b}}^{J/\psi} \approx (6/36)^{-0.45} = 2.2$, in agreement with the measured value of 2.34 ± 0.35.

For a more direct study of the diffractive structure function, the analysis was extended to events in which at least one jet was reconstructed. The ratio $R_{J/\psi}$ was studied as a function of $x_{\rm bj}$. By combining this result with a similar measurement of diffractive dijet production with a leading antiproton, the gluon fraction of the (anti)proton diffractive structure was found to be

$$f_g = 0.59 \pm 0.15$$

This result is in agreement with the gluon fraction of $0.54^{+0.16}_{-0.14}$ derived previously by comparing diffractive W, dijet and b-quark production [1].

CDF COLLABORATION

T. Affolder,[21] H. Akimoto,[43] A. Akopian,[36] M. G. Albrow,[10] P. Amaral,[7] S. R. Amendolia,[32] D. Amidei,[24] K. Anikeev,[22] J. Antos,[1] G. Apollinari,[36] T. Arisawa,[43] T. Asakawa,[41] W. Ashmanskas,[7] M. Atac,[10] F. Azfar,[29] P. Azzi-Bacchetta,[30] N. Bacchetta,[30] M. W. Bailey,[26] S. Bailey,[14] P. de Barbaro,[35] A. Barbaro-Galtieri,[21] V. E. Barnes,[34] B. A. Barnett,[17] M. Barone,[12] G. Bauer,[22] F. Bedeschi,[32] S. Belforte,[40] G. Bellettini,[32] J. Bellinger,[44] D. Benjamin,[9] J. Bensinger,[4] A. Beretvas,[10] J. P. Berge,[10] J. Berryhill,[7] B. Bevensee,[31] A. Bhatti,[36] M. Binkley,[10] D. Bisello,[30] R. E. Blair,[2] C. Blocker,[4] K. Bloom,[24] B. Blumenfeld,[17] S. R. Blusk,[35] A. Bocci,[32] A. Bodek,[35] W. Bokhari,[31] G. Bolla,[34] Y. Bonushkin,[5] D. Bortoletto,[34] J. Boudreau,[33] A. Brandl,[26] S. van den Brink,[17] C. Bromberg,[25] M. Brozovic,[9] N. Bruner,[26] E. Buckley-Geer,[10] J. Budagov,[8] H. S. Budd,[35] K. Burkett,[14] G. Busetto,[30] A. Byon-Wagner,[10] K. L. Byrum,[2] M. Campbell,[24] W. Carithers,[21] J. Carlson,[24] D. Carlsmith,[44] J. Cassada,[35] A. Castro,[30] D. Cauz,[40] A. Cerri,[32] A. W. Chan,[1] P. S. Chang,[1] P. T. Chang,[1] J. Chapman,[24] C. Chen,[31] Y. C. Chen,[1] M. -T. Cheng,[1] M. Chertok,[38] G. Chiarelli,[32] I. Chirikov-Zorin,[8] G. Chlachidze,[8] F. Chlebana,[10] L. Christofek,[16] M. L. Chu,[1] S. Cihangir,[10] C. I. Ciobanu,[27] A. G. Clark,[13] A. Connolly,[21] J. Conway,[37] J. Cooper,[10] M. Cordelli,[12] J. Cranshaw,[39] D. Cronin-Hennessy,[9] R. Cropp,[23] R. Culbertson,[7] D. Dagenhart,[42] F. DeJongh,[10] S. Dell'Agnello,[12] M. Dell'Orso,[32] R. Demina,[10] L. Demortier,[36] M. Deninno,[3] P. F. Derwent,[10] T. Devlin,[37] J. R. Dittmann,[10] S. Donati,[32] J. Done,[38] T. Dorigo,[14] N. Eddy,[16] K. Einsweiler,[21] J. E. Elias,[10] E. Engels, Jr.,[33] W. Erdmann,[10] D. Errede,[16] S. Errede,[16] Q. Fan,[35] R. G. Feild,[45] C. Ferretti,[32] R. D. Field,[11] I. Fiori,[3] B. Flaugher,[10] G. W. Foster,[10] M. Franklin,[14] J. Freeman,[10] J. Friedman,[22] Y. Fukui,[20]

S. Galeotti,[32] M. Gallinaro,[36] T. Gao,[31] M. Garcia-Sciveres,[21] A. F. Garfinkel,[34] P. Gatti,[30] C. Gay,[45] S. Geer,[10] D. W. Gerdes,[24] P. Giannetti,[32] P. Giromini,[12] V. Glagolev,[8] M. Gold,[26] J. Goldstein,[10] A. Gordon,[14] A. T. Goshaw,[9] Y. Gotra,[33] K. Goulianos,[36] C. Green,[34] L. Groer,[37] C. Grosso-Pilcher,[7] M. Guenther,[34] G. Guillian,[24] J. Guimaraes da Costa,[24] R. S. Guo,[1] C. Haber,[21] E. Hafen,[22] S. R. Hahn,[10] C. Hall,[14] T. Handa,[15] R. Handler,[44] W. Hao,[39] F. Happacher,[12] K. Hara,[41] A. D. Hardman,[34] R. M. Harris,[10] F. Hartmann,[18] K. Hatakeyama,[36] J. Hauser,[5] J. Heinrich,[31] A. Heiss,[18] M. Herndon,[17] B. Hinrichsen,[23] K. D. Hoffman,[34] C. Holck,[31] R. Hollebeek,[31] L. Holloway,[16] R. Hughes,[27] J. Huston,[25] J. Huth,[14] H. Ikeda,[41] J. Incandela,[10] G. Introzzi,[32] J. Iwai,[43] Y. Iwata,[15] E. James,[24] H. Jensen,[10] M. Jones,[31] U. Joshi,[10] H. Kambara,[13] T. Kamon,[38] T. Kaneko,[41] K. Karr,[42] H. Kasha,[45] Y. Kato,[28] T. A. Keaffaber,[34] K. Kelley,[22] M. Kelly,[24] R. D. Kennedy,[10] R. Kephart,[10] D. Khazins,[9] T. Kikuchi,[41] M. Kirk,[4] B. J. Kim,[19] H. S. Kim,[16] M. J. Kim,[19] S. H. Kim,[41] Y. K. Kim,[21] L. Kirsch,[4] S. Klimenko,[11] P. Koehn,[27] A. Köngeter,[18] K. Kondo,[43] J. Konigsberg,[11] K. Kordas,[23] A. Korn,[22] A. Korytov,[11] E. Kovacs,[2] J. Kroll,[31] M. Kruse,[35] S. E. Kuhlmann,[2] K. Kurino,[15] T. Kuwabara,[41] A. T. Laasanen,[34] N. Lai,[7] S. Lami,[36] S. Lammel,[10] J. I. Lamoureux,[4] M. Lancaster,[21] G. Latino,[32] T. LeCompte,[2] A. M. Lee IV,[9] S. Leone,[32] J. D. Lewis,[10] M. Lindgren,[5] T. M. Liss,[16] J. B. Liu,[35] Y. C. Liu,[1] N. Lockyer,[31] J. Loken,[29] M. Loreti,[30] D. Lucchesi,[30] P. Lukens,[10] S. Lusin,[44] L. Lyons,[29] J. Lys,[21] R. Madrak,[14] K. Maeshima,[10] P. Maksimovic,[14] L. Malferrari,[3] M. Mangano,[32] M. Mariotti,[30] G. Martignon,[30] A. Martin,[45] J. A. J. Matthews,[26] J. Mayer,[23] P. Mazzanti,[3] K. S. McFarland,[35] P. McIntyre,[38] E. McKigney,[31] M. Menguzzato,[30] A. Menzione,[32] C. Mesropian,[36] T. Miao,[10] R. Miller,[25] J. S. Miller,[24] H. Minato,[41] S. Miscetti,[12] M. Mishina,[20] G. Mitselmakher,[11] N. Moggi,[3] C. Moore,[10] E. Moore,[26] R. Moore,[24]

Y. Morita,[20] A. Mukherjee,[10] T. Muller,[18] A. Munar,[32] P. Murat,[10] S. Murgia,[25] M. Musy,[40] J. Nachtman,[5] S. Nahn,[45] H. Nakada,[41] T. Nakaya,[7] I. Nakano,[15] C. Nelson,[10] D. Neuberger,[18] C. Newman-Holmes,[10] C.-Y. P. Ngan,[22] P. Nicolaidi,[40] H. Niu,[4] L. Nodulman,[2] A. Nomerotski,[11] S. H. Oh,[9] T. Ohmoto,[15] T. Ohsugi,[15] R. Oishi,[41] T. Okusawa,[28] J. Olsen,[44] C. Pagliarone,[32] F. Palmonari,[32] R. Paoletti,[32] V. Papadimitriou,[39] S. P. Pappas,[45] D. Partos,[4] J. Patrick,[10] G. Pauletta,[40] M. Paulini,[21] C. Paus,[22] L. Pescara,[30] T. J. Phillips,[9] G. Piacentino,[32] K. T. Pitts,[16] R. Plunkett,[10] A. Pompos,[34] L. Pondrom,[44] G. Pope,[33] M. Popovic,[23] F. Prokoshin,[8] J. Proudfoot,[2] F. Ptohos,[12] G. Punzi,[32] K. Ragan,[23] A. Rakitine,[22] D. Reher,[21] A. Reichold,[29] W. Riegler,[14] A. Ribon,[30] F. Rimondi,[3] L. Ristori,[32] W. J. Robertson,[9] A. Robinson,[23] T. Rodrigo,[6] S. Rolli,[42] L. Rosenson,[22] R. Roser,[10] R. Rossin,[30] W. K. Sakumoto,[35] D. Saltzberg,[5] A. Sansoni,[12] L. Santi,[40] H. Sato,[41] P. Savard,[23] P. Schlabach,[10] E. E. Schmidt,[10] M. P. Schmidt,[45] M. Schmitt,[14] L. Scodellaro,[30] A. Scott,[5] A. Scribano,[32] S. Segler,[10] S. Seidel,[26] Y. Seiya,[41] A. Semenov,[8] F. Semeria,[3] T. Shah,[22] M. D. Shapiro,[21] P. F. Shepard,[33] T. Shibayama,[41] M. Shimojima,[41] M. Shochet,[7] J. Siegrist,[21] G. Signorelli,[32] A. Sill,[39] P. Sinervo,[23] P. Singh,[16] A. J. Slaughter,[45] K. Sliwa,[42] C. Smith,[17] F. D. Snider,[10] A. Solodsky,[36] J. Spalding,[10] T. Speer,[13] P. Sphicas,[22] F. Spinella,[32] M. Spiropulu,[14] L. Spiegel,[10] J. Steele,[44] A. Stefanini,[32] J. Strologas,[16] F. Strumia, [13] D. Stuart,[10] K. Sumorok,[22] T. Suzuki,[41] T. Takano,[28] R. Takashima,[15] K. Takikawa,[41] P. Tamburello,[9] M. Tanaka,[41] B. Tannenbaum,[5] W. Taylor,[23] M. Tecchio,[24] P. K. Teng,[1] K. Terashi,[41] S. Tether,[22] D. Theriot,[10] R. Thurman-Keup,[2] P. Tipton,[35] S. Tkaczyk,[10] K. Tollefson,[35] A. Tollestrup,[10] H. Toyoda,[28] W. Trischuk,[23] J. F. de Troconiz,[14] J. Tseng,[22] N. Turini,[32] F. Ukegawa,[41] T. Vaiciulis,[35] J. Valls,[37] S. Vejcik III,[10] G. Velev,[10] R. Vidal,[10] R. Vilar,[6] I. Volobouev,[21] D. Vucinic,[22] R. G. Wagner,[2] R. L. Wagner,[10]

J. Wahl,[7] N. B. Wallace,[37] A. M. Walsh,[37] C. Wang,[9] C. H. Wang,[1] M. J. Wang,[1] T. Watanabe,[41] D. Waters,[29] T. Watts,[37] R. Webb,[38] H. Wenzel,[18] W. C. Wester III,[10] A. B. Wicklund,[2] E. Wicklund,[10] H. H. Williams,[31] P. Wilson,[10] B. L. Winer,[27] D. Winn,[24] S. Wolbers,[10] D. Wolinski,[24] J. Wolinski,[25] S. Wolinski,[24] S. Worm,[26] X. Wu,[13] J. Wyss,[32] A. Yagil,[10] W. Yao,[21] G. P. Yeh,[10] P. Yeh,[1] J. Yoh,[10] C. Yosef,[25] T. Yoshida,[28] I. Yu,[19] S. Yu,[31] A. Zanetti,[40] F. Zetti,[21] and S. Zucchelli[3]

(CDF Collaboration)

[1] *Institute of Physics, Academia Sinica, Taipei, Taiwan 11529, Republic of China*

[2] *Argonne National Laboratory, Argonne, Illinois 60439*

[3] *Istituto Nazionale di Fisica Nucleare, University of Bologna, I-40127 Bologna, Italy*

[4] *Brandeis University, Waltham, Massachusetts 02254*

[5] *University of California at Los Angeles, Los Angeles, California 90024*

[6] *Instituto de Fisica de Cantabria, University of Cantabria, 39005 Santander, Spain*

[7] *Enrico Fermi Institute, University of Chicago, Chicago, Illinois 60637*

[8] *Joint Institute for Nuclear Research, RU-141980 Dubna, Russia*

[9] *Duke University, Durham, North Carolina 27708*

[10] *Fermi National Accelerator Laboratory, Batavia, Illinois 60510*

[11] *University of Florida, Gainesville, Florida 32611*

[12] *Laboratori Nazionali di Frascati, Istituto Nazionale di Fisica Nucleare, I-00044 Frascati, Italy*

[13] *University of Geneva, CH-1211 Geneva 4, Switzerland*

[14] *Harvard University, Cambridge, Massachusetts 02138*

[15] *Hiroshima University, Higashi-Hiroshima 724, Japan*

[16] *University of Illinois, Urbana, Illinois 61801*

[17] *The Johns Hopkins University, Baltimore, Maryland 21218*

[18] *Institut für Experimentelle Kernphysik, Universität Karlsruhe, 76128 Karlsruhe, Germany*

[19] *Korean Hadron Collider Laboratory: Kyungpook National University, Taegu 702-701; Seoul National University, Seoul 151-742; and SungKyunKwan University, Suwon 440-746; Korea*

[20] *High Energy Accelerator Research Organization (KEK), Tsukuba, Ibaraki 305, Japan*

[21] *Ernest Orlando Lawrence Berkeley National Laboratory, Berkeley, California 94720*

[22] *Massachusetts Institute of Technology, Cambridge, Massachusetts 02139*

[23] *Institute of Particle Physics: McGill University, Montreal H3A 2T8; and University of Toronto, Toronto M5S 1A7; Canada*

[24] *University of Michigan, Ann Arbor, Michigan 48109*

[25] *Michigan State University, East Lansing, Michigan 48824*

[26] *University of New Mexico, Albuquerque, New Mexico 87131*

[27] *The Ohio State University, Columbus, Ohio 43210*

[28] *Osaka City University, Osaka 588, Japan*

[29] *University of Oxford, Oxford OX1 3RH, United Kingdom*

[30] *Universita di Padova, Istituto Nazionale di Fisica Nucleare, Sezione di Padova, I-35131 Padova, Italy*

[31] *University of Pennsylvania, Philadelphia, Pennsylvania 19104*

[32] *Istituto Nazionale di Fisica Nucleare, University and Scuola Normale Superiore of Pisa, I-56100 Pisa, Italy*

[33] *University of Pittsburgh, Pittsburgh, Pennsylvania 15260*

[34] *Purdue University, West Lafayette, Indiana 47907*

[35] *University of Rochester, Rochester, New York 14627*

[36] *Rockefeller University, New York, New York 10021*

[37] *Rutgers University, Piscataway, New Jersey 08855*

[38] *Texas A&M University, College Station, Texas 77843*

[39] *Texas Tech University, Lubbock, Texas 79409*

[40] *Istituto Nazionale di Fisica Nucleare, University of Trieste/ Udine, Italy*

[41] *University of Tsukuba, Tsukuba, Ibaraki 305, Japan*

[42] *Tufts University, Medford, Massachusetts 02155*

[43] *Waseda University, Tokyo 169, Japan*

[44] *University of Wisconsin, Madison, Wisconsin 53706*

[45] *Yale University, New Haven, Connecticut 06520*

Appendix A

Analytical Form of B-hadron Lifetime Parameterization

$$B(x) = \int_0^\infty P(y-x) \cdot E(y, \lambda_B) dy \tag{A.1}$$

$$\begin{aligned} B(x) =& \frac{1 - f_{tail}}{\lambda_B} \cdot \text{freq}\left(\frac{x}{\sigma_{J/\psi}} - \frac{\sigma_{J/\psi}}{\lambda_B}\right) \cdot \exp\left(\frac{\sigma^2_{J/\psi}}{2\lambda_B^2} - \frac{x}{\lambda_B}\right) \\ &+ \begin{cases} \dfrac{f_{tail}}{2\lambda_B \lambda_{tail}} \cdot \dfrac{e^{x/\lambda_{tail}}}{c_a} & \text{if } x \leq 0 \\ \dfrac{f_{tail} e^{-x/\lambda_B}}{2\lambda_B \lambda_{tail}} \cdot \left[\dfrac{1}{c_s} \cdot (1 - e^{-c_s x}) + \dfrac{1}{c_a}\right] & \text{if } x > 0 \end{cases} \end{aligned} \tag{A.2}$$

where $\quad c_a = \dfrac{1}{\lambda_{tail}} + \dfrac{1}{\lambda_B}, \quad c_s = \dfrac{1}{\lambda_{tail}} - \dfrac{1}{\lambda_B},$

and freq(z) is the normal frequency function

$$\text{freq}(z) = \frac{1}{\sqrt{2\pi}} \int_{-\infty}^{z} \exp(-t^2/2) dt \tag{A.3}$$

Appendix B

Code for implementing the Color Octet Model in PYTHIA

```
    ELSEIF(ISUB.EQ.86) THEN
C...g + g -> J/Psi + g.
C
C... Color-Octet Matrix Elements for J/psi
C               (CTEQ 2L)
C
        SQM3=(2.*1.48)**2
        XO83S1=0.0033
        XO81S3P=0.0048
C
C   COLOR SINGLET
C
       FACQQG1=COMFAC*AS**3*(5./9.)*PARP(38)*SQRT(SQM3)*
     &  ((SH*(SH-SQM3))**2+(TH*(TH-SQM3))**2+(UH*(UH-SQM3))**2)/
     &  ((SH-SQM3)*(TH-SQM3)*(UH-SQM3))**2
C
C   COLOR OCTET (3-S-1)
C
        FACQQG2=-COMFAC*AS**3*(1./18.)*3.1416/SQRT(SQM3)*
     &   (27.*(SH*TH+TH*UH+UH*SH)-19.*SQM3**2)*((TH**2+TH*UH+UH**2)**2-
     &   SQM3*(TH+UH)*(2.*TH**2+TH*UH+2.*UH**2)+SQM3**2*
     &   (TH**2+TH*UH+UH**2))*XO83S1/
     &   ((TH-SQM3)*(UH-SQM3))**2/(SH-SQM3)**2
C
C   COLOR OCTET (1-S-0)/3 + (3-P-0) !!!
```

```
C
        FACQQG3=1000.*COMFAC*(5.*3.1416*AS**3/(4.*SQRT(SQM3)))/SH*
     &   (SH**2*(SH-SQM3)**2+SH*TH*UH*(SQM3-2.*SH)+(TH*UH)**2)/(TH*UH)*
     &   ((SH**2-SQM3*SH+SQM3**2)**2-
     &   TH*UH*(2.*TH**2+3.*TH*UH+2.*UH**2))*XO81S3P/
     &   ((TH-SQM3)*(UH-SQM3))**2/(SH-SQM3)**2
         FACQQG3=FACQQG3/1000.
C
C ... Scaling factor for g + q -> J/psi + q
C
         SCALGQ=1.25
C
        IF(KFAC(1,21)*KFAC(2,21).NE.0) THEN
          NCHN=NCHN+1
          ISIG(NCHN,1)=21
          ISIG(NCHN,2)=21
          ISIG(NCHN,3)=1
          SIGH(NCHN)=FACQQG1
          NCHN=NCHN+1
          ISIG(NCHN,1)=21
          ISIG(NCHN,2)=21
          ISIG(NCHN,3)=1
          SIGH(NCHN)=FACQQG2*SCALGQ
          NCHN=NCHN+1
          ISIG(NCHN,1)=21
          ISIG(NCHN,2)=21
          ISIG(NCHN,3)=1
          SIGH(NCHN)=3.*FACQQG3*SCALGQ
        ENDIF
```

Bibliography

[1] T. Affolder *et al.*, Phys. Rev. Lett. **84**, 232 (1999).

[2] J.D. Bjorken, Phys. Rev. D **47** 101 (1993); SLAC-PUB-6463, SLAC-PUB-6477 (1994).

[3] P.D.B. Collins, *An Introduction to Regge Theory and High Energy Physics*, Cambridge Univ. Press, UK 1977.

[4] K. Goulianos, Phys. Lett. B **358**, 379 (1995).

[5] S. Abatzis *et al.*, Phys. Lett. B **324**, 509 (1994); F. Antinori *et al.*, Phys. Lett. B **353**, 589 (1995).

[6] F.E. Low, Phys. Rev. D **12**, 163 (1975).

[7] S. Nussinov, Phys. Rev. Lett. **34**, 1286 (1975); Phys. Rev. D **14**, 246 (1976).

[8] Yu.A. Simonov, Phys. Lett. B **249**, 514 (1990); Nucl. Phys. B (Proc. Suppl.) 23, 283 (1991).

[9] G. Ingelman and P.E. Schlein, Phys. Lett. B **152**, 256 (1985).

[10] R. Bonino *et al.*, Phys. Lett. B **211**, 239 (1988).

[11] A. Brandt *et al.*, Phys. Lett. B **297**, 417 (1992).

[12] A. Brandt *et al.*, Phys. Lett. B **421**, 395 (1998).

[13] K. Wacker, UA1 Collaboration, *Diffractive heavy flavor production in UA1*, in Proceedings of the 7th Topical Workshop on Proton Antiproton Collider Physics, Fermilab, 1988.

[14] K. Eggert, UA1 Collaboration, *Search for diffractive heavy flavor production at the CERN proton-antiproton collider*, in Proceedings of the 2nd International Conference on Elastic and Diffractive Scattering, Rockefeller University, New York, 1987.

[15] P. Bruni, G. Ingelman, *Diffractive hard scattering at ep and $p\bar{p}$ colliders*, in Proceedings of the Europhysics Conference on high Energy Physics, Marseille, France, 1993.

[16] E.L. Berger, J.C. Collins, D.E. Soper, G. Sterman, Nucl. Phys. **B286**, 704 (1987).

[17] A. Donnachie and P.V. Landshoff, Phys. Lett. B **191**, 309 (1987); Nucl. Phys. **B303**, 634 (1988).

[18] M. Derrick *et al.*, Phys. Lett. B **315**, 481 (1993); Z. Phys. C **68**, 569 (1995).

[19] T. Ahmed *et al.*, Nucl. Phys. **B429**, 477 (1994); Phys. Lett. B **348**, 681 (1995).

[20] C. Adloff *et al.*, Z. Phys. C **76**, 613 (1997).

[21] F. Abe *et al.*, Phys. Rev. Lett. **79**, 2636 (1997).

[22] T. Affolder *et al.*, Phys. Rev. Lett. **84**, 5043 (2000).

[23] F. Abe *et al.*, Phys. Rev. Lett. **78**, 2698 (1997).

[24] F. Abe *et al.*, Phys. Rev. Lett. **80**, 1156 (1998); Phys. Rev. Lett. **81**, 5278 (1998).

[25] B. Abbott *et al.*, Phys. Lett. B **440**, 189 (1998).

[26] T. Affolder *et al.*, Phys. Rev. Lett. **85**, 4215 (2000).

[27] S. Erhan, P.E. Schlein, Phys. Lett. B **427**, 389 (1998).

[28] J.C. Collins, L. Frankfurt, M. Strikman, Phys. Lett. B **307**, 161 (1993).

[29] R. Van Royen and V.F. Weisskopff, Nuovo Cim. **50**, 617 (1967); erratum Nuovo Cim. **51**, 583 (1967).

[30] F. Abe *et al.*, Phys. Rev. Lett. **69**, 3704 (1992); Phys. Rev. Lett. **79**, 572 (1997).

[31] E. Braaten and T. Yuan, Phys. Rev. Lett. **71**, 1673 (1993); Phys. Rev. D **52**, 6627 (1995).

[32] G. Bodwin, E. Braaten and G. Lapage, Phys. Rev. D **46**, 1914 (1992); Phys. Rev. D **51**, 1125 (1995).

[33] M. Neubert, Phys. Rept. **245**, 259 (1994).

[34] E. Shuryak, Phys. Lett. B **93**, 134 (1980); Nucl. Phys. **B198**, 83 (1982).

[35] N. Isgur and M. Wise, Phys. Lett. B **232**, 113 (1989); Phys. Lett. B **237**, 527 (1990); Phys. Lett. **66**, 1130 (1991).

[36] P. Cho and A.K. Leibovich, Phys. Rev. D **53**, 150 (1996); Phys. Rev. D **53**, 6203 (1996).

[37] R. Balest *et al.*, Phys. Rev. D **52**, 2661 (1995).

[38] F. Abe *et al.*, Phys. Rev. Lett. **79**, 578 (1997).

[39] D. Mohl, G. Petrucci, L. Thorndahl, S. Van Der Meer, Phys. Rep. **58**, 73 (1980).

[40] F. Abe *et al.*, Nucl. Instrum. Methods A **271**, 387 (1988).

[41] D. Amidei *et al.*, Nucl. Instrum. Methods A **350**, 73 (1994); P. Azzi *et al.*, Nucl. Instrum. Methods A **360**, 137 (1995).

[42] F. Bedeschi *et al.*, Nucl. Instrum. Methods A **268**, 50 (1988).

[43] S. Bhadra *et al.*, Nucl. Instrum. Methods A **268**, 92 (1988).

[44] L. Balka *et al.*, Nucl. Instrum. Methods A **267**, 272 (1988).

[45] S. Bertolucci *et al.*, Nucl. Instrum. Methods A **267**, 301 (1988).

[46] K. Yasuoka *et al.*, Nucl. Instrum. Methods A **267**, 315 (1988).

[47] R.G. Wagner *et al.*, Nucl. Instrum. Methods A **267**, 330 (1988).

[48] S.R. Hahn *et al.*, Nucl. Instrum. Methods A **267**, 351 (1988).

[49] Y. Fukui *et al.*, Nucl. Instrum. Methods A **267**, 280 (1988).

[50] W.C. Carithers *et al.*, *Resistive Plastic Cathode Pad Readout Proportional Mode Chamber for CDF*; W.C. Carithers *et al.*, *Performance and Calibration Studies of the CDF Endplug Calorimeter*, in Proceedings of the Gas Sampling Calorimetry Workshop II, Fermilab, 1985.

[51] G. Brandenburg *et al.*, Nucl. Instrum. Methods A **267**, 257 (1988).

[52] S. Cihangir *et al.*, Nucl. Instrum. Methods A **267**, 249 (1988).

[53] G. Ascoli *et al.*, Nucl. Instrum. Methods A **268**, 33 (1988).

[54] A. Gauthier *et al.*, *Design and Performance of Drift Chambers for the Central Muon Upgrade*, CDF/PUB/CDF/CDFR/1500.

[55] P. Giromini *et al.*, *The Central Muon Extension Scintillators (CSX)*, CDF/DOC/MUON/PUBLIC/3898.

[56] K. Byrum *et al.*, Nucl. Instrum. Methods A **268**, 46 (1988).

[57] D. Amidei *et al.*, Nucl. Instrum. Methods A **269**, 51 (1988).

[58] F. Abe *et al.*, Phys. Rev. Lett. **76**, 3070 (1996).

[59] G. Drake *et al.*, Nucl. Instrum. Methods A **269**, 68 (1988).

[60] G.W. Foster *et al.*, Nucl. Instrum. Methods A **269**, 93 (1988).

[61] B. Denby and M. Contreras, *A New Look at Punchthrough at CDF*, CDF/MEMO/MUON/CDFR/1324.

[62] A. Bodek, *Punchthrough in Hadronic Shower Cascades, Muon Identification and Scaling Laws for Different Absorbers*, University of Rochester preprint, UR 911 (1985).

[63] F. Yuan and K.T. Chao, Phys. Rev. D **57**, 5658 (1998).

[64] S. Bagdasarov, *Observation of Diffractive W-boson Production at the Tevatron*, CDF/THESIS/ELECTROWEAK/PUBLIC/4603.

[65] H. Ikeda, *Observation of Diffractive Bottom Quark Production in 1.8-TeV Proton-Antiproton Collisions*, CDF/THESIS/JET/PUBLIC/4872.

[66] D. P. Cronin-Hennessy, A. Beretvas, S. Segler, *Getting Your Luminosity*, CDF/DOC/CDF/CDFR/4317.

[67] F. Abe *et al.*, Phys. Rev. D **57**, 5382 (1998).

[68] M.G. Albrow, K. Borras, K. Goulianos and K. Terashi, *Further Studies of Dijets in Double Pomeron Exchange*, CDF/ANAL/JET/CDFR/5023.

[69] T. Sjöstrand, Comp. Phys. Comm. **82**, 74 (1994).

[70] B. Cano-Coloma and A. Sanchis-Lozano, Nucl. Phys. **B508**, 753 (1997).

[71] P. Bruni, A. Edin, and G. Ingelman, *POMPYT version 2.6 - A Monte Carlo to Simulate Diffractive Hard Scattering Processes*, Report No. DESY-95, DRAFT, ISSN 0418-9833; http://www3.tsl.uu.se/thep/pompyt/